

THESIS / THÈSE

DOCTOR OF SCIENCES

Cosmological Spherical Collapse with Relativistic Hydrodynamics and Threshold for Primordial Black Hole Formation

STAELENS, Francois

Award date:
2020

Awarding institution:
University of Namur

[Link to publication](#)

General rights

Copyright and moral rights for the publications made accessible in the public portal are retained by the authors and/or other copyright owners and it is a condition of accessing publications that users recognise and abide by the legal requirements associated with these rights.

- Users may download and print one copy of any publication from the public portal for the purpose of private study or research.
- You may not further distribute the material or use it for any profit-making activity or commercial gain
- You may freely distribute the URL identifying the publication in the public portal ?

Take down policy

If you believe that this document breaches copyright please contact us providing details, and we will remove access to the work immediately and investigate your claim.



UNIVERSITÉ DE NAMUR

FACULTÉ DES SCIENCES

DÉPARTEMENT DE MATHÉMATIQUE

Cosmological Spherical Collapse with Relativistic Hydrodynamics and Threshold for Primordial Black Hole Formation

Thèse présentée par
François Staelens
pour l'obtention du grade
de Docteur en Sciences

Composition du Jury :

Sébastien CLESSE
André FÜZFA (Promoteur)
Éric GOURGOULHON
Alexandre MAUROY (Président du Jury)
Christophe RINGEVAL

Novembre 2020

Effondrement gravitationnel sphérique avec hydrodynamique relativiste et seuil de formation des trous noirs primordiaux

par François Staelens

Résumé :

Ce travail est consacré à l'étude, avec les outils de la relativité numérique, de l'effondrement gravitationnel sphérique de matière avec pression dans un univers en expansion. La thèse est divisée en deux parties.

Dans la première, nous étudions l'universalité de l'effondrement critique par rapport au type de matière en considérant une équation d'état ω constante comme paramètre de contrôle. Il est montré numériquement, dans les cas où l'arrière-plan est Minkowski ou de Sitter, que la masse du trou noir formé, pour les solutions sous-critiques, décroît en loi de puissance de $|\omega - \omega^*|$, où ω^* est le ω critique, avec un exposant indépendant du type de matière. Pour le cas de l'univers Friedmann-Lemaître-Robertson-Walker rempli de matière, de sérieuses indications en faveur de l'universalité sont exposées mais le bruit numérique provenant des conditions Einstein-de Sitter au bord extérieur nous empêche de le prouver complètement.

La seconde partie étudie l'hypothèse selon laquelle la matière noire serait constituée de trous noirs primordiaux (TNP) en calculant le delta critique à plusieurs moments de l'histoire thermique post-inflationniste de l'univers, où l'équation d'état connaît plusieurs creux qui favorisent leur formation. Nous montrons que les pics de la fonction de masse des TNP de [Carr et al. 2019b] sont atténués et translatés vers des masses plus petites. Ces résultats semblent réfuter l'hypothèse initiale mais l'importance du choix de la gauge est soulignée.

Cosmological Spherical Collapse with Relativistic Hydrodynamics and Threshold for Primordial Black Hole Formation

by François Staelens

Abstract:

This work is devoted to the study of the gravitational spherical collapse of pressured matter in a cosmological background using the tools of numerical relativity. The thesis is divided into two parts.

In the first one, we investigate the universality of the critical collapse with respect to the matter type by considering the constant equation of state ω as a control parameter. It is shown numerically, in the cases the background is Minkowski or de Sitter, that the mass of the formed black hole, for sub-critical solutions, rescales in a power-law of $|\omega - \omega^*|$, where ω^* is the critical ω , with an exponent independent of the matter type. For the full matter Friedmann-Lemaître-Robertson-Walker background, serious indications in favour of universality are exposed but some numerical noise from the Einstein-de Sitter outer boundary conditions prevents us to prove it completely.

The second part investigates the hypothesis that Dark Matter is made of Primordial Black Holes (PBH) by computing the critical delta at several moments of the post-inflationary thermal history of universe, when the equation of state knows some dips that favour their formation. The peaks in the PBH mass function of [Carr et al. 2019b] are shown to be attenuated and shifted towards lower masses. These results seem to reject the initial hypothesis but the importance of the gauge choice is pointed out.

Thèse de doctorat en Sciences Mathématiques (Ph.D. thesis in Mathematics)

Date: 20/11/2020

Département de Mathématique

Promoteur (Advisor): André FÜZFA

Remerciements

L'aventure se termine après plus de quatre ans passés sur ce travail. L'heure des remerciements est enfin arrivée.

Je remercie mon promoteur André Füzfa pour m'avoir suivi et encadré tout au long de ce doctorat.

Merci aux membres du jury d'avoir accepté d'en faire partie et pour leurs avis éclairants concernant mes résultats.

I warmly thank Isabel Cordero-Carrion for the very helpful and instructive discussions during the three conferences I attended in Spain. If the code finally works, it is thanks to her and her important advice.

Merci à Watson pour son aide précieuse tout au long de la thèse. Sans lui je n'y serais probablement pas arrivé.

Merci à tous mes collègues du département et aux amis que j'y ai rencontrés. En particulier à Nicolas pour ses calembourgs qui nous ont bien accompagnés lors de nos conférences en Espagne. À Martin pour les jeux (belote, bulot, tarot, Diplomacy,... et bien sûr Nainwak!), son humour raffiné, son aide et son soutien dans les moments importants de cette thèse. À Jérémy pour les débats de l'Arsenal, son soutien et sa confiance. Et, dans le désordre, merci à Julien, Morgane, Candy, Alexis, Delphine, Pauline, Eve-Aline, Mara, Arnaud, Anthony, François, Jon, Riccardo,... La vie au département n'aurait pas été si joyeuse sans vous.

Merci à Joanna pour sa chouette compagnie au bureau et sans qui les journées de travail auraient été moins souriantes.

Je remercie bien sûr Manon pour m'avoir accueilli chaleureusement dans ce bureau, pour son soutien indéfectible, les discussions sans fin que nous interrompons de temps en temps pour travailler (si si), et surtout pour son amitié.

Merci à Thibault et Fanny qui m'ont toujours soutenu dans les épreuves quelles

qu'elles soient.

Merci à Gaby et Jean-Marie pour l'intérêt qu'ils ont toujours porté à ce que je faisais et la confiance qu'ils ont en moi.

Merci à mes parents et mes grands-parents pour leur soutien tout au long de ces années de recherche.

Merci à mes frères d'avoir tout de même parfois, au milieu des plougeries, fait semblant de reconnaître que j'avais un vrai boulot.

Et enfin, merci à Elodie qui a toujours cru en moi et qui m'a soutenu du début à la fin, même lorsque j'ai été sur le point d'abandonner. Durant cette longue aventure, je sais que je n'ai pas été toujours facile ni très organisé mais cela n'a jamais semblé trop te gêner. Reste comme tu es, je sais que pour une fois je ne me suis pas trompé.

*À Jacques, toi qui me surnommes si souvent « Herr Doktor »,
pour la place que tu occupes dans mon cœur.*

À notre princesse, pour que tu sois fière de moi.

Contents

Introduction	1
1 A Formalism for General Relativity	7
1.1 General Relativity and the Cauchy Problem	8
1.2 The 3 + 1-formalism of General Relativity	9
1.3 The BSSN equations	12
1.4 The BSSN formalism in spherical symmetry	13
1.5 The Hydrodynamics for a perfect fluid and the Valencia formulation .	15
1.6 Equation of state	18
1.7 A homogeneous background : the Friedmann-Lemaître equations in BSSN variables	19
1.8 The linearized equations	20
2 Building of a Numerical Code	23
2.1 Choice of the formalism	24
2.2 The implementation	24
2.2.1 The PIRK algorithm	24
2.2.2 A HRSC method for the hydrodynamics	26
2.2.3 Recovering the primitive variables	28
2.3 Boundary and gauge conditions	30
2.3.1 Boundary conditions	30
2.3.2 Slicing conditions	31
2.4 The question of the initial data	32
2.4.1 A conformally flat metric as initial data	32
2.4.2 The long-wavelength approximation as initial data	34
2.4.3 The initial background	40
2.5 Scales	40
2.6 Validation of the code	41

3	The Search for Universality	45
3.1	Introduction	46
3.2	Quantities and observables	47
3.3	Phenomenology by varying the equation of state	52
3.4	Towards universality	62
3.4.1	Tests with conformally flat initial conditions	63
3.4.2	Tests with initial conditions from the long-wavelength approx- imation	71
3.4.3	The static Minkowski case	72
3.4.4	The de Sitter case	73
3.5	Conclusion	74
4	PBH Formation	75
4.1	Problem setting	76
4.2	A time dependent equation of state	77
4.3	Results and consequences	78
	Conclusion	83
	Bibliography	89

Introduction

In the beginning of the twentieth century, Albert Einstein and Georges Lemaitre published several articles that would change the world ([Einstein 1916], [Einstein 1917], [Lemaitre 1927], [Lemaitre 1933]). The first one developed the theory of General Relativity (GR) that is a relativistic theory of gravitation. In particular, Einstein found partial differential equations that linked the space-time curvature (its shape) to its contents (the matter in it), known as "Einstein equations". The second studied the universe as a whole and developed first models of expanding universes, by solving Einstein equations in homogeneous particular cases, which lead in particular to the big bang theory. Those works gave birth to complementary new physics : the general relativity and the cosmology.

General relativity was, at that time, a really new physics that could give a solution to unexplained problems of the classical newtonian theory of gravitation, such as the advance of Mercury's perihelion. GR obtained great successes with gravitational lensing events or the correct prediction of the rate of growth of galaxy clusters. This theory also revealed interesting new features from the equations such as the possibility of black holes, that Schwarzschild first derived from Einstein equations. At the present time, no observation call into question general relativity (see [Will 2001]), on the contrary : recent detection of gravitational waves by [Abbott et al 2016] gave an additional support to this theory.

Concerning cosmology, many improvement have been done, turning this field to a precision science. The standard model of cosmology is ruled by the Friedmann-Lemaitre-Robertson-Walker metric and gives a efficient description of a homogeneous dynamical universe. The observations by the Hubble and ground-based telescopes in the 1990's showed moreover that the universe was not simply expanding but accelerating. This led to the reconsideration of the well known cosmological constant that Einstein had abandoned.

Rapidly, the question of the formation of structures, both astronomical and cosmological, occurs. The first case to address is the spherical gravitational collapse. Newtonian mechanics gives interesting results but the first relativistic used model is the so called "top-hat" model (see [Bonnor 1956 (Reprinted as Gen. Rel. Grav in 1998)], that

simply divides the problem into an inner and an outer Friedmann homogeneous universe. The linear theory of perturbations, N-body simulations in semi-Newtonian approximation and post-Newtonian developments are also widely used methods, either in astrophysical or cosmological circumstances. However, some situations require a completely relativistic and non linear treatment, especially in scenarii implying strong gravitational fields such as black hole formation. It was thus important to develop new tools to solve Einstein equations even when no analytical solution exists. The first step to achieve that was to find a way to write the field equations as a Cauchy problem. The solution that appeared is the $3 + 1$ formalism of GR that formally splits space-time into time *and* space (see [Gourgoulhon 2012]).

The development of this $3 + 1$ formalism of General Relativity and the associated algorithmics during the XXth century combined with the "computer revolution" of the last decades permits the study of gravitation from a new point of view. The important works of Darmois ([Darmois 1927]), Lichnerowicz ([Lichnerowicz 1939], [Lichnerowicz 1944], [Lichnerowicz 1952]), Choquet-Bruhat ([Fourès-Bruhat 1956]), Dirac ([Dirac 1958], [Dirac 1959]) and Arnowitt et al. ([Arnowitt et al. 1962]), managed to write Einstein equations as a constrained Cauchy problem, a suitable form for numerical integration, in the view of developing a quantum theory of gravitation. These laid the foundations of the Hamiltonian formulation of GR and introduced the well known Arnowitt-Deser-Misner (ADM) formalism. With the emergence of more and more powerful computers, numerical integration of such new formalisms became possible and the capability to simulate GR whatever the ingredients considered was a dream that scientists could then try to render realistic. This opened the era of Numerical Relativity, a new field of research whose aim is to build and use numerical methods to solve Einstein equations of GR on a computer. Remarkable works to mention are [Nakamura et al. 1987], [Nakamura 1994], [Shibata and Nakamura 1995], [Baumgarte and Shapiro 1998], which developed the famous Baumgarte-Shibata-Shapiro-Nakamura (BSSN) formalism in the 1990's, the one used in this thesis.

Numerical Relativity obtained several successes and is now widely used in modern physics. It has been used, among others, to simulate spherical black holes formation ([Shibata and Sasaki 1999]), stable solutions of neutron stars ([Shibata and Uryu 2002]) or binary black holes ([Pretorius 2005]),... The first detection of gravitational waves, the signal GW150914 from a binary black holes merger in 2016 by [Abbott et al 2016] is an important evidence in favour of GR. This was made possible thanks to numerical relativity which permitted to verify post-Newtonian analytical developments and to go beyond it by simulating the black holes merger. This event has even enforced Numerical Relativity as an active, powerful and essential branch of physics.

Another major result was the discovery of critical phenomena in gravitation and their universality. Universality is an important notion of dynamical systems originally found in phase transitions of statistical mechanics. A transition phase is a severe change in the properties of a system like transitions between states of matter or superconductivity for example. It happens when a certain parameter β , called a "control" parameter (typically the temperature), reaches a critical value β_* that makes another parameter α (the heat capacity, for example), the "order" parameter, rescaled in a

power-law of $|\beta - \beta_*|$. This is the famous universal scaling law. Such a property is important because it reveals that a particular critical phenomenon is very general and occurs in the same way whatever the near critical value of some parameters. It is also independent of the "microphysics" (the details of the model such as the fluid or field considered) and is a generic property of emergent (collective) phenomena. Similar universal behaviours have been looked for and found in various situations such as transition phases, epidemic models, network dynamics and thus gravitational collapse.

In this latter case, it was first discovered by Choptuik in 1992 ([Choptuik 1993]) by using numerical relativity for the spherical collapse of a massless scalar field. Near critical solutions appeared to follow a particular scaling law that does not depend on the initial curvature profile. Several works ([Evans and Coleman 1994], [Maison 1996], [Nielsen and Choptuik 2000], [Niemeyer and Jedamzik 1999], [Hawke and Stewart 2002], [Musco and Miller 2013],...) were dedicated to the search for universality in the case of a fluid of matter with constant equation of state, both in asymptotically Minkowski and homogeneous Friedmann universes. Results produced in these works showed that the critical collapse is universal in all the cases in question.

Universality in gravitation collapse is thus a widely studied concept since the development of numerical relativity. Similar universal scaling laws have been searched in many other situations such as charged black hole mass, angular momentum, coupled scalar field, higher dimensions,... (see [Gundlach and Martín-García 2007] for a review).

On our side, our thesis was initially designed to pursue the works of J. Requier ([Requier et al. 2015], [Requier 2015],[Requier et al. 2016]) who built a numerical code that performed the evolution of a fluctuation of dust matter, possibly in the presence of a scalar field, in a homogeneous Friedmann universe. The idea was to incorporate a hydrodynamics module in the code to allow it to deal with pressured fields of matter, such as radiation for example. Once done, we used the code by evolving fluctuations of a barotropic fluid with constant equation of state $p = \omega e$, where e is the energy-density of the fluid and p is the pressure, the most used matter model in cosmology. We then noticed that, whatever the initial density profile, there was a threshold value ω^* in the equation of state for which values under ω^* gave birth to a black hole and values above ω^* dilute the fluctuation into the surrounding medium. This led us naturally to the question of the universality of this critical phenomenon with respect to the equation of state parameter (i.e. the matter type). This is a different approach from the works [Nielsen and Choptuik 2000], [Musco and Miller 2013] (and the other mentioned above) since we tried to show universal scaling laws that do not depend on the equation of state, that is to say the matter type, while previous studies fixed the matter type and showed scaling laws independent on the curvature and matter distribution profile. Our work constitutes a generalization of the concept of universality to another parameter of the Cauchy problem, concerning the internal properties of matter, which makes it complementary to those mentioned above. Our results will hopefully be published in the near future since a scientific communication has already been submitted to a scientific journal and is in the reviewing process.

This work is interesting from GR and mathematical point of view, but it has also important cosmological motivations. Indeed, the large scale structure formation mech-

anism is still not completely understood and our work could be a starting point for the study of spherically symmetric fluctuations evolution at several cosmological epochs. It could extend from primordial black holes formation in the radiation era to long term evolutions going through the equivalence radiation-dust epoch by considering two-fluids simulations.

Precisely, talking about Primordial Black Holes (PBH), we invested in a second research project in the second part of the thesis. We worked jointly with S. Clesse on this topic with our code. Primordial black holes are black holes that could have gravitationally formed during the radiation era. They were first considered by the precursor works of [Zel'dovich and Novikov 1967], [Hawking 1971],[Hawking 1975], [Carr and Hawking 1974],[Carr 1975] and already the idea that they could constitute a non negligible part of the missing matter, the famous Dark Matter (DM), was present in it. Several observations from the Macho and the Eros experiments rejected this hypothesis but the first detection of gravitational waves in 2016 and corrections in the calculations re-enhanced the interest in it.

In this context, we pursue the works of [Carr et al. 2019b] who computed the PBH mass function, assuming DM is entirely made of PBHs, on the basis of the fluctuation in the equation of state during the post-inflationary thermal history of universe. At that time, some dips occur in the equation of state and enhance the probability for PBHs to form. These dips produce important peaks in the PBH mass function at some particular values. This calculation had the advantages to verify all the astronomical and cosmological constraints and to explain additionally other unsolved issues. By using numerical relativity, we performed this computation by using a really time-dependant equation of state, on the contrary to what was done before by considering, for each value of ω in the history, a universe with this value fixed to a constant. This would give us a more realistic approximation of the PBH mass function and possibly confirm or infirm the hypothesis that PBHs could account for a significant part of DM. A scientific communication is currently in preparation to publish our results.

To perform all this, we are following the works made in [Rekier et al. 2015] and [Rekier et al. 2016], within the framework of numerical relativity. We use the BSSN formalism of GR, in spherical symmetry, conjointly with the Valencia formulation for the hydrodynamics [Banyuls et al. 1997]. Many numerical simulations in spherical symmetry use formalisms specially adapted to this kind of symmetry, such as the Misner-Sharp formalism (see [Baumgarte and Shapiro 2010] or [Shibata 2016] for a presentation of this formalism). A drawback of these formalisms is that they are written in comoving gauges. Because we intent to study in the future the spherical collapse of several fluids with relative velocities, comoving gauges were not suitable at the moment. The polar-areal gauge is often used too, such as in [Noble and Choptuik 2016], but is difficult to use in a cosmological context since it does not converge to the FLRW metric as $r \rightarrow \infty$. This is why we chose the BSSN formalism. When spherical coordinates are employed, it induces terms of the form $1/r^m$ which become problematic near the the origin of coordinates (i. e. when $r \rightarrow 0$). To overcome this difficulty, the authors of [Cordero-Carrion and Cerda-Duran 2016] developed a partially implicit Runge-Kutta (PIRK) method for hyperbolic wave-like equations which solves the problems of instabilities without other regularization. This scheme

has already been applied with success in the case of asymptotic flatness in [Montero and Cordero-Carrion 2012]. For the case of an expanding background universe, it has also been done but only in the case of dust in [Rekier et al. 2015] and in the case of a scalar field in [Rekier et al. 2016]. We apply here to the case of pressured matter.

We encountered several difficulties that forced us to reconsider the formulation of the initial problem and of the observables. In particular, we had to use the mass and compactness notions used in [Shibata and Sasaki 1999] and [Musco 2019] and we had to derive in our specific gauge the analytic solution of the equations in the long-wavelength approximation, as was done in [Harada et al. 2015] in other gauges. The resulting code is not perfect, because of the difficulty in implementing the outer boundary conditions when the cosmological horizon is greater than the outer boundary of the numerical grid and the need of additional precision in the case of cosmologies with matter. But it is robust enough for our purpose and gives interesting original results that prove universality with respect to matter types.

The thesis is organised as follows. First chapter is dedicated to the quick presentation of Einstein equations, the $3 + 1$ formalism of GR and the particular Baumgarte-Shibata-Shapiro-Nakamura formalism that is used in all this work. We do not intend to compete existing well realised textbooks on the topic (see [Shibata 2016], [Gourgoulhon 2012], [Alcubierre 2008], [Rezzolla and Zanotti 2013] or [Baumgarte and Shapiro 2010] for example). We however hope it will permit people with a master degree level in mathematical or theoretical physics to follow and appreciate our contribution. Chapter 2 is devoted to the process of the building of a numerical code that must solve Einstein equations of GR. Important questions such as the formalism, the gauge or the initial conditions are addressed, and the code is validated at the end of this chapter. The third chapter, which is the central part of this manuscript, contains all the results concerning the works on the universality of the critical collapse with respect to the matter type. The fourth and last chapter contains the work on PBH formation during the thermal history of the universe. Chapter 3 and 4 can be read independently from each other. We end with a conclusion that summarizes the work realised in the thesis and discuss about the underlying perspectives for possibly future studies.

Chapter 1

A Formalism for General Relativity

Summary

In this chapter we present the $3 + 1$ -formalism of general relativity. This is an unavoidable step in view of a numerical treatment since we need to write the equations in the form of a Cauchy problem. We also present one of the most widely used formulation of this formalism, due to its stability : the Baumgarte-Shibata-Shapiro-Nakamura (BSSN) equations. We explicit the spherical symmetry case since we will exclusively stay in that context. We will use it in the next chapters in a cosmological context, as [Rekier 2015] and [Shibata and Sasaki 1999] did before us. This is why we also give the Friedmann equations in these variables. Since we are working with general pressured fields of matter, we present the Valencia formulation for the hydrodynamics that must be used to ensure stability.

1.1 General Relativity and the Cauchy Problem

General Relativity (GR) is a geometric theory of gravitation, discovered by Einstein in the beginning of the XXth century, based on the "Equivalence principle" which states that there is no way to distinguish, in a local experiment, the effect of gravity from the acceleration of the whole laboratory. In other words, it is equivalent to say that there exists, at any point of space-time, a local inertial reference frame (i.e. in free fall). This also includes the Galileo's principle according to whom all masses fall in the same way. In GR, it is useful to use geometric units in which the gravitation Newton constant G and the speed of light c are both unity, $G = c = 1$, and this is what we do all along this thesis. The space-time is modelled by a four-dimensional differential manifold equipped with a Lorentzian metric (a metric with signature $(-, +, +, +)$ ⁽¹⁾). The metric $g_{\mu\nu}$ is often, in the coordinates $\{x^\mu\}$, written thanks to the line-element

$$ds^2 = g_{\mu\nu} dx^\mu dx^\nu. \quad (1.1.1)$$

In this theory, gravitation is present directly in this metric through the space-time curvature. It is linked to the energy and momentum contained in it by the Einstein equations

$$R_{\mu\nu} - \frac{1}{2}g_{\mu\nu}R = 8\pi T_{\mu\nu}, \quad (1.1.2)$$

where $R_{\mu\nu}$ is the Ricci tensor (the trace of the Riemann tensor), R its trace (the Riemannian curvature also called Ricci Scalar) and $T_{\mu\nu}$ the stress-energy tensor (also called energy-momentum tensor). This set of 10 equations (the metric is symmetrical), of which only 6 are independent, are second order partial differential equations in the metric terms that are non linear and does not possess generally an analytical solution. This can be derived by using the least-action principle on the Einstein-Hilbert action

$$S = \frac{1}{16\pi} \int d^4x \sqrt{-g} R + S_{\text{matter}}, \quad (1.1.3)$$

where the action for the matter content is given by the lagrangian :

$$S_{\text{matter}} := \int d^4x \sqrt{-g} \mathcal{L}_{\text{matter}}. \quad (1.1.4)$$

The corresponding stress-energy tensor is thus given by

$$T_{\mu\nu} := \frac{-2}{\sqrt{-g}} \frac{\partial(\sqrt{-g} \mathcal{L}_{\text{matter}})}{\partial g^{\mu\nu}}. \quad (1.1.5)$$

The general equations of General Relativity are written in a covariant form. This means that there is, a priori, no distinction between space and time in the coordinates. However, it can be convenient to make the theory look like a classical dynamical system with time-dependant quantities such as fields on a three-dimensional space. Such a step is even essential since it is particularly appropriate for numerical computations.

⁽¹⁾The signature $(+, -, -, -)$ is equivalently widely used in the literature.

However, we must keep in mind that some solutions do not enter that category such as the Gödel universe (see [Gödel 1949]) that possesses closed timelike curves. To avoid such solutions, we must work exclusively with globally hyperbolic space-times which are space-times admitting a Cauchy surface Σ , a hypersurface that intersects exactly once each causal curve without endpoint (see [Hawking and Ellis 1973], [Gourgoulhon 2012]). A globally hyperbolic space-time has the topology $\mathbb{R} \times \Sigma$ and thus excludes temporal loops. This property allows to formally separate time from space and thus to write the equations in the form of an initial value problem. The existence and uniqueness of solutions of this Cauchy problem was a challenging question during the last century and was finally proven for a quite general case in [Choquet-Bruhat and Geroch 1969] with the global existence and uniqueness theorem of Choquet-Bruhat and Geroch (see [Choquet-Bruhat 2009] for more informations). The writing of GR as a dynamical system is performed through the 3 + 1 formalism that we present now in the next section.

1.2 The 3 + 1-formalism of General Relativity

We present briefly the 3 + 1 formalism, following what is done in [Rekier 2015]. But since well written reference books on the topic already exist (see for example [Alcubierre 2008] and [Gourgoulhon 2012]), we do not intend to give a fully detailed description of this formalism. We prefer to present here the minimum of developments required to understand the theory.

Let $t(x^\mu)$ be a scalar field on a globally hyperbolic 4-dimensional space-time M with coordinates $\{x^\mu\}$. This scalar field must be such that the equation $\Phi \equiv t(x^\mu) = t_0$ defines a collection of non intersecting hypersurfaces labelled by the real parameter t_0 . We denote the hypersurface corresponding to the value t_0 by Σ_{t_0} . The unit normal vector to all hypersurfaces is given by $n_\mu = -\alpha \frac{\partial t}{\partial x^\mu}$ and is such that $n^\mu n_\mu = -1$.

On each hypersurface Σ_t , we define a set of coordinates $\{y^i\}$ such that $\{t, y^i\}$ is a new set of coordinates of the space-time. The coordinate t will represent a time coordinate and $\{y^i\}$ spatial coordinates. Consider now the collection of curves made by points with constant $\{y^i\}$. All these curves represent the time evolution of fixed spatial coordinates. We denote their tangent vector by $t^\mu := \frac{dx^\mu}{dt}$. Moreover, we define the following 3-vectors, tangent to all hypersurfaces, $e_i^\mu := \frac{\partial x^\mu}{\partial y^i}$. Therefore we can decompose t^μ as

$$t^\mu = \alpha n^\mu + \beta^i e_i^\mu, \quad (1.2.1)$$

where α is called the *lapse* and the β^i are the *shifts*. The lapse defines the foliation of space-time while the shifts determines the relative velocity between the Eulerian observer (the one moving along a worldline perpendicular to all hypersurfaces) and the events of constant spatial coordinates. The Figure 1.1 represents that situation. The next step is to write de metric in the coordinates $\{t, y^i\}$. By change of coordinates, we have

$$dx^\mu = t^\mu dt + e_i^\mu dy^i.$$

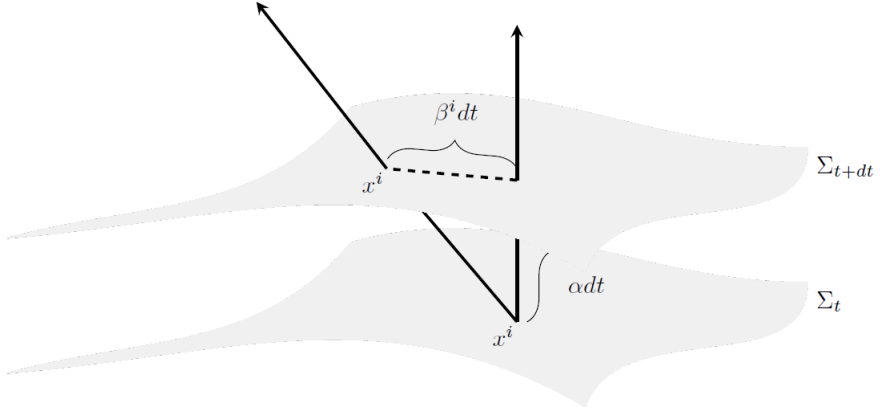


Figure 1.1 – Foliation of space-time. The quantity αdt is the lapse of proper time measured by a Eulerian observer and the β^i are the shift between that observer and the one with constant spatial coordinates. Figure taken from [Rekier 2015].

If the metric, in the frame $\{x^\mu\}$, is given by $ds^2 = g_{\mu\nu}dx^\mu dx^\nu$, we have

$$ds^2 = -\alpha^2 dt^2 + \gamma_{ij}(dy^i + \beta^i dt)(dy^j + \beta^j dt), \quad (1.2.2)$$

where $\gamma_{ij} := g_{\mu\nu}e_i^\mu e_j^\nu$ is the induced 3-metric on the hypersurface. If we denote the metric elements in the frame $\{t, y^i\}$ by $\tilde{g}_{\alpha\beta}$, then we have

$$\tilde{g}_{\alpha\beta} = \begin{pmatrix} -\alpha^2 + \beta^i \beta_i & \beta_i \\ \beta_j & \gamma_{ij} \end{pmatrix} \quad \tilde{g}^{\alpha\beta} = \frac{1}{\alpha^2} \begin{pmatrix} -1 & \beta^j \\ \beta^i & \gamma^{ij} \alpha^2 - \beta^i \beta_j \end{pmatrix}. \quad (1.2.3)$$

We thus can derive the equation

$$g^{\mu\nu} = \gamma^{ij} e_i^\mu e_j^\nu - n^\mu n^\nu.$$

We use the following notation :

$$\gamma^{\mu\nu} := \gamma^{ij} e_i^\mu e_j^\nu.$$

This is an important quantity because it is used to project tensors onto the hypersurface.

An important parameter of the 3 + 1 formalism is the extrinsic curvature. That curvature measures how the hypersurface is curved within the surrounding spacetime. Contrary to the intrinsic curvature, the extrinsic curvature thus depends on the way the hypersurfaces are embedded in M . We can obtain that information by looking at the parallel transport of the normal vector n along the curves in the hypersurface. It is thus defined as the following projection:

$$K_{\mu\nu} := -\gamma_\mu^\sigma \nabla_\sigma n_\nu. \quad (1.2.4)$$

The dynamics of spacetime is given by two sets of equations. First, we have the dynamical equations for $\gamma_{\mu\nu}$ that only depends on the geometry of the hypersurfaces :

$$\partial_t \gamma_{\mu\nu} = -2\alpha K_{\mu\nu} + D_\mu \beta_\nu + D_\nu \beta_\mu, \quad (1.2.5)$$

where D_μ is the Levi-Civita connection on the hypersurface.

As we told, those equations are only geometrical consequences of the definitions of the variables it implies. The second set of equations is built thanks to the Einstein equations. But to write them, we need the projections of the stress-energy tensor :

$$\begin{aligned} E &:= n_\alpha n_\beta T^{\alpha\beta}; \\ j_\mu &:= -\gamma_{\mu\alpha} n_\beta T^{\alpha\beta}; \\ S_{\mu\nu} &:= \gamma_{\alpha\mu} \gamma_{\beta\nu} T^{\alpha\beta}, \end{aligned}$$

where E and j_μ can be seen as the *energy density* and the *momentum density*.

By projecting the Einstein equations onto the hypersurface, we obtain

$$\partial_t K_{\mu\nu} - \mathcal{L}_\beta K_{\mu\nu} = -D_\mu D_\nu \alpha + \alpha \left[{}^{(3)}R_{\mu\nu} + K K_{\mu\nu} - 2K_{\mu\lambda} K_\nu^\lambda \right] + 4\pi\alpha \left[\gamma_{\mu\nu}(S - E) - 2S_{\mu\nu} \right], \quad (1.2.6)$$

where ${}^{(3)}R_{\mu\nu\lambda\sigma}$ is the curvature tensor of the hypersurface and \mathcal{L} is the Lie derivative. With the two sets of equations 1.2.5 and 1.2.6, we can fully describe the dynamics of spacetime. The remaining projections of the Einstein equations give additional constraints on this evolution :

$${}^{(3)}R + K^2 - K_{\mu\nu} K^{\mu\nu} = 16\pi E; \quad (1.2.7)$$

$$D_\nu K_\mu^\nu - D_\mu K = 8\pi j_\mu. \quad (1.2.8)$$

Those four sets of equations are referred to as the ADM equations, for Arnowitt, Deser and Misner (see [Arnowitt et al. 1962]). This formalism can be seen as a Hamiltonian formulation of Einstein theory of gravitation since it can be shown that the extrinsic curvature $K_{\mu\nu}$ is closely related to the conjugated quantities of the 3-metric $\gamma_{\mu\nu}$, as well as momentum are linked to positions in classical Hamiltonian mechanics.

From the conservation of the stress-energy tensor $\nabla_\mu T^{\mu\nu} = 0$, we can derive two other equations of conservation :

$$\mathcal{L}_n E + D_\mu j^\mu + \frac{2}{\alpha} j_\mu (D^\mu \alpha) - KE - K_{\mu\nu} S^{\mu\nu} = 0; \quad (1.2.9)$$

$$\mathcal{L}_n j_\sigma + D_\mu S_\sigma^\mu + S_\sigma^\mu \frac{D_\mu \alpha}{\alpha} - K j_\sigma + E \frac{D_\sigma \alpha}{\alpha} = 0. \quad (1.2.10)$$

This first one is the equation for the conservation of energy and the second one is for the conservation of momentum. Generally, those two additional equations are used to derive the hydrodynamics of the problem (equations for the source terms).

The ADM equations are generally not used in their original form when performing numerical integration. Indeed, if we wish to use a free evolution scheme, that is to say choosing initial conditions verifying the constraints (1.2.8) and then evolving them

with equations 1.2.5 and 1.2.6, we must be sure that the constraints equations will still be verified at every time of integration, or at least will not increase. In other words, we must use a scheme that is numerically stable. We thus need a strongly hyperbolic system while ADM equations are only weakly hyperbolic (see [Baumgarte and Shapiro 2010]). In the present thesis, we are working with the BSSN formulation because it is strongly hyperbolic and one of the most used in numerical relativity.

1.3 The BSSN equations

The BSSN scheme, named in honour of Shibata and Nakamura who first derived it [Shibata and Nakamura 1995] and of Baumgarte and Shapiro who revised it [Baumgarte and Shapiro 1998], is a free evolution scheme using a conformal decomposition of the metric. It is based on the introduction of a conformal factor in the metric and on the splitting of the extrinsic curvature between its trace and traceless parts. Let us define the conformal metric by

$$\tilde{\gamma}_{ij} := \psi^{-4} \gamma_{ij}, \quad (1.3.1)$$

where ψ is the conformal factor and we impose $\tilde{\gamma} := \det(\tilde{\gamma}_{\mu\nu}) = 1$. The evolution equation for the determinant metric γ then reads

$$\partial_t \psi = -\frac{1}{6} \psi (\alpha K - \partial_i \beta^i) + \beta^i \partial_i \psi. \quad (1.3.2)$$

We split the extrinsic curvature into its trace and traceless parts :

$$K_{ij} = \frac{1}{3} \gamma_{ij} K + A_{ij}. \quad (1.3.3)$$

We define

$$\tilde{A}_{ij} := \psi^{-4} A_{ij}. \quad (1.3.4)$$

The two constraints equations become

$$\mathcal{H} \equiv R^{(3)} - \tilde{A}_{ij} \tilde{A}^{ij} + \frac{2}{3} K^2 - 16\pi E = 0; \quad (1.3.5)$$

$$\mathcal{M} \equiv \partial_j \tilde{A}^{ij} + \tilde{\Gamma}_{jk}^i \tilde{A}^{jk} + 6\tilde{A}^{ij} \frac{\partial_j \psi}{\psi} - \frac{2}{3} \tilde{\gamma}^{ij} \partial_j K - 8\pi \tilde{j}^i = 0, \quad (1.3.6)$$

where $\tilde{\Gamma}_{jk}^i := \psi^{-4} \Gamma_{jk}^i$ and $\tilde{j}^i := \psi^{-4} j^i$. A particularity of the BSSN scheme is the addition of a new dynamical variable

$$\tilde{\Gamma}^i := \tilde{\gamma}^{jk} \tilde{\Gamma}_{jk}^i = -\partial_j \tilde{\gamma}^{ij}, \quad (1.3.7)$$

which has the evolution equation

$$\partial_t \tilde{\Gamma}^i - \mathcal{L}_{\beta} \tilde{\Gamma}^i = \tilde{\gamma}^{jk} \partial_j \partial_k \beta^i + \frac{1}{3} \tilde{\gamma}^{ij} \partial_j \partial_k \beta^k - 2(\alpha \partial_j \tilde{A}^{ij} + \tilde{A}^{ij} \partial_j \alpha). \quad (1.3.8)$$

Following [Alcubierre 2008], the system of equations is made strongly hyperbolic, and thus stable, by adding a multiple of the momentum constraint :

$$\begin{aligned} \partial_t \tilde{\Gamma}^i - \mathcal{L}_\beta \tilde{\Gamma}^i &= \tilde{\gamma}^{jk} \partial_j \partial_k \beta^i + \frac{1}{3} \tilde{\gamma}^{jj} \partial_j \partial_k \beta^k - 2(\alpha \partial_j \tilde{A}^{ij} + \tilde{A}^{ij} \partial_j \alpha) \\ &+ 2\alpha \xi \left[\partial_j \tilde{A}^{ij} + \tilde{\Gamma}^i_{jk} \tilde{A}^{jk} + 6\tilde{A}^{ij} \frac{\partial_j \psi}{\psi} - \frac{2}{3} \tilde{\gamma}^{jj} \partial_j K - 8\pi \tilde{j}^i \right], \end{aligned}$$

with $\xi > \frac{1}{2}$.

The other equations are derived from the ADM equations :

$$\begin{aligned} \partial_t \tilde{\gamma}_{ij} - \mathcal{L}_\beta \tilde{\gamma}_{ij} &= -2\alpha \tilde{A}_{ij}; \\ \partial_t \tilde{A}_{ij} - \mathcal{L}_\beta \tilde{A}_{ij} &= \psi^{-4} \{ -D_i D_j \alpha + \alpha R_{ij} + 4\pi \alpha [\gamma_{ij}(S - E) - 2S_{ij}] \}^{TF} \alpha \left(K \tilde{A}_{ij} - 2\tilde{A}_{ik} \tilde{A}_j^k \right); \\ \partial_t K - \mathcal{L}_\beta K &= -D_i D^i \alpha + \alpha \left(\tilde{A}_{ij} \tilde{A}^{ij} + \frac{1}{3} K^2 \right) + 4\pi \alpha (E + S), \end{aligned}$$

where TF denotes the trace-free part. Those equations form the BSSN equations, when no gauge has been specified. In what follows, we will work in spherical symmetry since this thesis studies the spherical collapse. The next section is then devoted to the writing of the BSSN equations in spherical symmetry.

1.4 The BSSN formalism in spherical symmetry

To develop the BSSN equations in spherical symmetry, we first write the metric in spherical coordinates :

$$ds^2 = -(\alpha^2 - \beta^2) dt^2 + 2\beta dt dr + \psi^4 a^2(t) (\hat{a} dr^2 + \hat{b} r^2 d\Omega^2), \quad (1.4.1)$$

where $\alpha(t, r)$ is the lapse, $\beta(t, r)$ is the radial component of the shift, \hat{a} and \hat{b} are the non-zero components of the conformal 3-metric and ψ^2 is the conformal factor. We also factored out the cosmological scale factor $a(t)$ from the conformal factor. This prescription is convenient in the view of a cosmological Friedmann universe taken as background. Note that the BSSN formalism requires that $\det(\tilde{\gamma}_{\mu\nu}) = 1$, which reads $\hat{a}\hat{b}^2 = 1$. We choose to work, for simplicity, in the zero shift gauge : $\beta = 0$. However, other choices of shift conditions could have been chosen and the interested reader can find other detailed examples in [Gourgoulhon 2012].

The extrinsic curvature is still split into its trace and a trace-free part :

$$K_{\mu\nu} = \frac{1}{3} \gamma_{\mu\nu} K + \psi^4 a^2 \hat{A}_{\mu\nu}. \quad (1.4.2)$$

Spherical symmetry implies that $\hat{A}_{\mu\nu}$ has only two non-vanishing components :

$$A_a := \hat{A}_r^r; \quad (1.4.3)$$

$$A_b := \hat{A}_\theta^\theta. \quad (1.4.4)$$

We then have, because $\hat{A}_{\mu\nu}$ is trace-free, that $A_a + 2A_b = 0$. In the same way, the conformal variable $\hat{\Gamma}^i$ has only the radial component that is non-zero :

$$\hat{\Delta}^r = \frac{1}{\hat{a}} \left[\frac{\partial_r \hat{a}}{2\hat{a}} - \frac{\partial_r \hat{b}}{\hat{b}} - \frac{2}{r} \left(1 - \frac{\hat{a}}{\hat{b}} \right) \right]. \quad (1.4.5)$$

The evolution of spacetime is ruled by the following equations (see [Rekier 2015]) :

$$\partial_t \hat{a} = -2\alpha \hat{a} A_a; \quad (1.4.6)$$

$$\partial_t \hat{b} = -2\alpha \hat{b} A_b; \quad (1.4.7)$$

$$\partial_t \psi = -\frac{1}{6} \alpha \psi K - \frac{1}{2a} \dot{a} \psi; \quad (1.4.8)$$

$$\partial_t K = -D^2 \alpha + \alpha \left(A_a^2 + 2A_b^2 + \frac{1}{3} K^2 \right) + 4\pi \alpha (E + S_a + 2S_b);$$

$$\partial_t A_a = -\left(D^r D_r \alpha - \frac{1}{3} D^2 \alpha \right) + \alpha \left(R_r^r - \frac{1}{3} R \right) + \alpha K A_a - \frac{16\pi}{3} \alpha (S_a - S_b);$$

$$\begin{aligned} \partial_t \hat{\Delta}^r &= -\frac{2}{\hat{a}} (A_a \partial_r \alpha + \alpha \partial_r A_a) + 2\alpha \left(A_a \hat{\Delta}^r - \frac{2}{r\hat{b}} (A_a - A_b) \right) \\ &+ \frac{\xi}{\hat{a}} \alpha \left[\partial_r A_a - \frac{2}{3} \partial_r K + 6A_a \frac{\partial_r \psi}{\psi} + (A_a - A_b) \left(\frac{2}{r} + \frac{\partial_r \hat{b}}{\hat{b}} \right) - 8\pi j_r \right] \end{aligned} \quad (1.4.9)$$

The choice which is chosen for ξ is $\xi = 2$. The quantities R_r^r , R , $D^r D_r \alpha$ and $D^2 \alpha$ are given in the metric variables :

$$\begin{aligned} R_r^r &= -\frac{1}{\psi^4 a^2 \hat{a}} \left[\frac{\partial_r^2 \hat{a}}{2\hat{a}} - \hat{a} \partial_r \hat{\Delta}^r - \frac{3}{4} \left(\frac{\partial_r \hat{a}}{\hat{a}} \right)^2 + \frac{1}{2} \left(\frac{\partial_r \hat{b}}{\hat{b}} \right)^2 \right. \\ &\quad \left. - \frac{1}{2} \hat{\Delta}^r \partial_r \hat{a} + \frac{\partial_r \hat{a}}{r\hat{b}} + \frac{2}{r^2} \left(1 - \frac{\hat{a}}{\hat{b}} \right) \left(1 + \frac{r\partial_r \hat{b}}{\hat{b}} \right) \right. \\ &\quad \left. + 4 \frac{\partial_r^2 \psi}{\psi} - 4 \left(\frac{\partial_r \psi}{\psi} \right)^2 - 2 \left(\frac{\partial_r \psi}{\psi} \right) \left(\frac{\partial_r \hat{a}}{\hat{a}} - \frac{\partial_r \hat{b}}{\hat{b}} - \frac{2}{r} \right) \right]; \end{aligned}$$

$$\begin{aligned} R &= -\frac{1}{\psi^4 a^2 \hat{a}} \left[\frac{\partial_r^2 \hat{a}}{2\hat{a}} + \frac{\partial_r^2 \hat{b}}{\hat{b}} - \hat{a} \partial_r \hat{\Delta}^r - \left(\frac{\partial_r \hat{a}}{\hat{a}} \right)^2 \right. \\ &\quad \left. + \frac{1}{2} \left(\frac{\partial_r \hat{b}}{\hat{b}} \right)^2 + \frac{2\partial_r \hat{b}}{r\hat{b}} \left(3 - \frac{\hat{a}}{\hat{b}} \right) + \frac{4}{r^2} \left(1 - \frac{\hat{a}}{\hat{b}} \right) \right. \\ &\quad \left. + 8 \frac{\partial_r^2 \psi}{\psi} - 8 \left(\frac{\partial_r \psi}{\psi} \right) \left(\frac{\partial_r \hat{a}}{2\hat{a}} - \frac{\partial_r \hat{b}}{\hat{b}} - \frac{2}{r} \right) \right]; \end{aligned}$$

$$D^r D_r \alpha = \frac{1}{\psi^4 a^2 \hat{a}} \left[\partial_r^2 \alpha - \partial_r \alpha \left(\frac{\partial_r \hat{a}}{2\hat{a}} + 2 \frac{\partial_r \psi}{\psi} \right) \right];$$

$$D^2\alpha = \frac{1}{\Psi^4 a^2 \hat{a}} \left[\partial_r^2 \alpha - \partial_r \alpha \left(\frac{\partial_r \hat{a}}{2\hat{a}} - \frac{\partial_r \hat{b}}{\hat{b}} - 2 \frac{\partial_r \Psi}{\Psi} - \frac{2}{r} \right) \right].$$

The Hamiltonian and Momentum constraints written in those coordinates are given by

$$\mathcal{H} \equiv R - (A_a^2 + 2A_b^2) + \frac{2}{3}K^2 - 16\pi E = 0; \quad (1.4.10)$$

$$\mathcal{M}^r \equiv \partial_r A_a - \frac{2}{3} \partial_r K + 6A_a \frac{\partial_r \Psi}{\Psi} + (A_a - A_b) \left(\frac{2}{r} + \frac{\partial_r \hat{b}}{\hat{b}} \right) - 8\pi j_r = 0. \quad (1.4.11)$$

The behaviours of the variables near the origin satisfy the following parity conditions to ensure regularity of the terms in $\frac{1}{r}$ (see [Alcubierre and Mendez 2011]) :

$$\alpha \sim \alpha_0 + O(r^2), \quad (1.4.12)$$

$$\hat{a} \sim \hat{a}_0 + O(r^2), \quad (1.4.13)$$

$$\hat{b} \sim \hat{b}_0 + O(r^2), \quad (1.4.14)$$

$$A_a \sim A_a^0 + O(r^2), \quad (1.4.15)$$

$$A_b \sim A_b^0 + O(r^2), \quad (1.4.16)$$

$$\hat{\Delta}^r \sim O(r^2), \quad (1.4.17)$$

where α_0 , \hat{a}_0 , \hat{b}_0 , A_a^0 and A_b^0 are functions of time exclusively. Moreover, terms in $(A_a - A_b)/r$ and $(1 + \hat{a}/\hat{b})/r$ must also disappear near the origin, which means that the two following conditions, the flatness regularity condition, must occur :

$$A_a - A_b \sim O(r^2) \Leftrightarrow A_a^0 = A_b^0, \quad (1.4.18)$$

$$\hat{a} - \hat{b} \sim O(r^2) \Leftrightarrow \hat{a}_0 = \hat{b}_0. \quad (1.4.19)$$

Numerically, it is challenging to build a code that verifies simultaneously the parity and flatness regularity conditions. Several articles discuss this issue (see [Arbona and Bona 1999], [Alcubierre and González 2005] and [Ruiz et al. 2008]). On our side, we do not need to implement such regularization conditions thanks to the kind of numerical code we use. We detail this algorithm in section 2.2.1.

1.5 The Hydrodynamics for a perfect fluid and the Valencia formulation

Up to now, we have partial differential equations sourced by projections of the energy-momentum tensor $T^{\mu\nu}$, and the evolution equations (1.2.9) for these source terms are derived from the conservation equation $\nabla_\mu T^{\mu\nu} = 0$. But we have not specified the components of this tensor yet. What the stress tensor is made of depends on what

fulfills the universe. For an empty universe, we should, for example, take $T^{\mu\nu} = 0$. In our case, we study the spherical collapse of matter fields. We thus consider the case of perfect fluids.

The tensor $T^{\mu\nu}$ of a perfect fluid can be written as a function of the rest-mass density ρ , the specific enthalpy h , the pressure p and the fluid 4-velocity u^μ :

$$T^{\mu\nu} = \rho h u^\mu u^\nu + p g^{\mu\nu}. \quad (1.5.1)$$

Recall that we are interested in its different projections :

$$E = n_\mu n_\nu T^{\mu\nu}, \quad (1.5.2)$$

$$j_i = -\gamma_{i\mu} n_\nu T^{\mu\nu}, \quad (1.5.3)$$

$$S_{ij} = \gamma_{i\mu} \gamma_{j\nu} T^{\mu\nu}, \quad (1.5.4)$$

where $n_\mu = (-\alpha, 0, 0, 0)$ is the four-vector field orthogonal to the spatial hypersurfaces in the zero shift case. Spherical symmetry imposes that the only independent quantities among the projections of this tensor are E , j^r , $S_a := S_r^r$ and $S_b := S_\theta^\theta$, and are given by :

$$E = \rho h W^2 - p, \quad (1.5.5)$$

$$j_r = \rho h W^2 v_r, \quad (1.5.6)$$

$$S_a = \rho h W^2 v^r v_r, \quad (1.5.7)$$

$$S_b = p, \quad (1.5.8)$$

where we have introduced v_r , the radial physical 3-velocity of the fluid for an Eulerian observer, and W , the associated Lorentz factor :

$$v^r = \frac{u^r}{\alpha u^t}, \quad (1.5.9)$$

$$W = \alpha u^t = \frac{1}{\sqrt{1 - v_r v^r}}, \quad (1.5.10)$$

with v^r in units of c .

The evolution of the source terms can be written in a conservative form by using the Valencia formulation (see [Banyuls et al. 1997]) which ensures stability. To do this, we follow [Rezzolla and Zanotti 2013] (and its notations) and we define the vector $\mathbf{U} = \sqrt{\gamma}(D, S_r, \tau)$ containing the conserved variables :

$$D = \rho W, \quad (1.5.11)$$

$$S_r = \rho h W^2 v_r, \quad (1.5.12)$$

$$\tau = \rho h W^2 - p - D. \quad (1.5.13)$$

Note that we exactly have $S_r = j_r$ but we prefer to keep the notation S_r when dealing with the conserved variables to avoid any possible confusion.

We point out that it is generally not possible to recover the primitive variables (v_r , h , p , ρ , ...) from the conserved ones (D , S_r , τ) in an analytical way, except in few particular cases. A root-finding procedure must be used (see [Rezzolla and Zanotti 2013]).

The hydrodynamical equations $\nabla_\mu T^{\mu\nu} = 0$, jointly with the baryon number conservation, thus read

$$\partial_t \mathbf{U} + \partial_r \mathbf{F}^r = \mathbf{S}, \quad (1.5.14)$$

where the fluxes \mathbf{F}^r are

$$\mathbf{F}^r = \sqrt{-g} \begin{pmatrix} Dv^r \\ S_r v^r + p \\ \tau v^r + p v^r \end{pmatrix}, \quad (1.5.15)$$

and the sources are⁽²⁾

$$\begin{aligned} \mathbf{S} &= \sqrt{-g} \begin{pmatrix} 0 \\ \frac{1}{2} T^{\mu\nu} \partial_r g_{\mu\nu} \\ -T^{\mu\nu} \nabla_\mu n_\nu \end{pmatrix} \\ &= \sqrt{-g} \begin{pmatrix} 0 \\ -\alpha T^{00} \partial_r \alpha + \frac{1}{2} T^{rr} \partial_r \gamma_{rr} + T^{\theta\theta} \partial_r \gamma_{\theta\theta} \\ -T^{0r} \partial_r \alpha + T^{rr} K_{rr} + 2T^{\theta\theta} K_{\theta\theta} \end{pmatrix}. \end{aligned} \quad (1.5.16)$$

We recall that those expressions are exact only in the case of spherical symmetry and vanishing shift ($\beta = 0$). General equations can be found in [Banyuls et al. 1997] and [Montero and Cordero-Carrion 2012].

Using these equations in this form will be problematic in the case of a non-constant background metric. Indeed, the asymptotic value of the vector \mathbf{U} is not well defined in spherical coordinates because the term $\sqrt{\gamma}$ diverges when $r \rightarrow +\infty$. To overcome this difficulty, we use the reference metric approach presented in [Montero et al. 2014]. It consists in taking as new variables $\tilde{\mathbf{U}} = \sqrt{\frac{\tilde{\gamma}}{\gamma}} (D, S_r, \tau)$, where $\tilde{\gamma}_{ij}$ is a reference metric whose determinant $\tilde{\gamma}$ is constant in time. In this case, the new fluxes are

$$\tilde{\mathbf{F}}^r = \alpha \sqrt{\frac{\tilde{\gamma}}{\gamma}} \begin{pmatrix} Dv^r \\ S_r v^r + p \\ \tau v^r + p v^r \end{pmatrix}, \quad (1.5.17)$$

and the source terms are

$$\begin{aligned} \tilde{\mathbf{S}} &= \alpha \sqrt{\frac{\tilde{\gamma}}{\gamma}} \begin{pmatrix} 0 \\ -\alpha T^{00} \partial_r \alpha + \frac{1}{2} T^{rr} \partial_r \gamma_{rr} + T^{\theta\theta} \partial_r \gamma_{\theta\theta} \\ -T^{0r} \partial_r \alpha + T^{rr} K_{rr} + 2T^{\theta\theta} K_{\theta\theta} \end{pmatrix} \\ &+ \begin{pmatrix} -\tilde{\mathbf{F}}_D^r \tilde{\Gamma}_{rk}^k \\ \tilde{\mathbf{F}}_{S_r}^r (\tilde{\Gamma}_{rr}^r - \tilde{\Gamma}_{rk}^k) + \alpha \sqrt{\frac{\tilde{\gamma}}{\gamma}} p (\tilde{\Gamma}_{\theta r}^\theta + \tilde{\Gamma}_{\phi r}^\phi) \\ -\tilde{\mathbf{F}}_t^r \tilde{\Gamma}_{kr}^k \end{pmatrix}. \end{aligned} \quad (1.5.18)$$

⁽²⁾We point out here an apparent little typo in [Montero and Cordero-Carrion 2012] where the terms with indices θ are missing.

The choice for $\tilde{\gamma}_{ij}$ is the flat metric in spherical polar coordinates : $\tilde{\gamma}_{ij} = \text{diag}(1, r^2, r^2 \sin^2 \theta)$. Our final source terms are thus, after evaluating the connection symbols,

$$\tilde{\mathbf{S}} = \alpha \sqrt{\frac{\bar{\gamma}}{\tilde{\gamma}}} \begin{pmatrix} 0 \\ -\alpha T^{00} \partial_r \alpha + \frac{1}{2} T^{rr} \partial_r \gamma_{rr} + T^{\theta\theta} \partial_r \gamma_{\theta\theta} \\ -T^{0r} \partial_r \alpha + T^{rr} K_{rr} + 2T^{\theta\theta} K_{\theta\theta} \end{pmatrix} - \frac{2}{r} \tilde{\mathbf{F}}^r. \quad (1.5.19)$$

Note that this expression can be derived in a direct way by simply developing the term

$$\partial_r \mathbf{F}^r = \partial_r (r^2 \sin \theta \tilde{\mathbf{F}}^r) = 2r \sin \theta \tilde{\mathbf{F}}^r + r^2 \sin \theta \partial_r \tilde{\mathbf{F}}^r$$

and inserting it in (1.5.14).

With that choice, our variables $\tilde{\mathbf{U}}$ are well defined at spatial infinity because

$$\alpha \sqrt{\frac{\bar{\gamma}}{\tilde{\gamma}}} = \alpha \psi^6 a^3 \rightarrow \bar{\alpha} a^3 \quad \text{as } r \rightarrow \infty,$$

where $\bar{\alpha}$ is the background lapse.

The last question that remains to be treated is to know what happens when we consider several matter fields. The easiest way to proceed is to build a stress tensor $T_{(k)}^{\mu\nu}$ for each matter field k and to sum them all to find the total stress tensor :

$$T^{\mu\nu} = \sum_k T_{(k)}^{\mu\nu}.$$

The corresponding source terms can be summed in the same way :

$$\begin{aligned} E &= \sum_k E_{(k)}, \\ j_r &= \sum_k j_r^{(k)}, \\ S_a &= \sum_k S_a^{(k)}, \\ S_b &= \sum_k S_b^{(k)}. \end{aligned}$$

Concerning the hydrodynamics equations (1.5.14), it depends on the adopted coupling between the fluids. In this thesis, we assume that there is no coupling between the fluids : each of them is conserved, independently from the others. We thus have $\nabla_\mu T_{(k)}^{\mu\nu} = 0$ for all k and one set of hydrodynamical equations for each matter field.

1.6 Equation of state

To close the system, we need an equation of state $f(p, \rho, \varepsilon) = 0$, where $\varepsilon = h - 1 - \frac{p}{\rho}$ is the specific internal energy, which will describe what kind of fluid we are using. If we want to simulate an ideal gas, the equation of state will be of the form

$$p = \rho \varepsilon (\gamma - 1), \quad (1.6.1)$$

where γ is the adiabatic index. For a polytropic fluid, the equation will be

$$p = \mathbf{K}\rho^\Gamma, \quad (1.6.2)$$

where \mathbf{K} is the polytropic constant and Γ is the polytropic exponent. Those two cases are widely used in numerical relativity simulations. However, in cosmology we often work with a linear barotropic equation of state :

$$p = \omega e, \quad (1.6.3)$$

where $e = \rho(1 + \varepsilon) = \rho h - p$ is the energy density. This equation of state has the advantage to give a simple (and analytical) formula to recover the primitive variables from the conserved ones (see 2.2.3). The value $\omega = 0$ represents a pressure-less matter (dust) while the value $\omega = \frac{1}{3}$ states for a radiation fluid (relativistic particles). Finally, $\omega < -\frac{1}{3}$ is the condition for the growth of the universe to be accelerated and the simplest way to achieve it is to consider a cosmological constant in the Einstein equations, corresponding to a constant value $\omega = -1$. However, in this work we consider mostly universes not accelerated, only filled with matter fields with $\omega \in [0, 1]$.

We here point out the fact that, when dealing with homogeneous cosmological spacetimes, the energy density is usually denoted by the letter ρ in the literature. In our case we prefer to use the letter e and use the letter ρ to denote the rest-mass density.

1.7 A homogeneous background : the Friedmann-Lemaître equations in BSSN variables

We wish to perform simulations of spherical collapse in a homogeneous and isotropic cosmological background. That means that, at large radii, our variables must be adjusted to a Friedmann-Lemaître-Robertson-Walker (FLRW) universe. We then give here the corresponding Friedmann-Lemaître equations. In all this thesis, an overline is used on a variable to indicate it is its background (homogeneous) value. The line-element is given by the FLRW metric, with possibly a dynamical lapse :

$$ds^2 = -\bar{\alpha}^2(t)dt^2 + a^2(t) (dr^2 + r^2 d\Omega^2), \quad (1.7.1)$$

where we consider that there is no curvature. The evolution of this metric is ruled by the well known Friedmann equations

$$\frac{1}{\bar{\alpha}^2} \left(\frac{\dot{a}}{a} \right)^2 = \frac{8\pi}{3} \bar{e}, \quad (1.7.2)$$

$$\frac{1}{\bar{\alpha}^2} \frac{\ddot{a}}{a} - \frac{\dot{a}}{a} \frac{\dot{\bar{\alpha}}}{\bar{\alpha}^3} = -\frac{4\pi}{6} (\bar{e} + 3\bar{p}), \quad (1.7.3)$$

where \bar{e} and \bar{p} are the total homogeneous background energy density and pressure. By "total", we mean that it is composed with the contribution of different kinds of

energy (matter (in general several species) and possibly a cosmological constant Λ in our case) :

$$\begin{cases} \bar{e} = \sum_k \bar{e}_k + e_\Lambda, \\ \bar{p} = \sum_k \bar{p}_k + p_\Lambda. \end{cases} \quad (1.7.4)$$

For the background, the hydrodynamical equations are simplified and the only evolution equations that are needed are the following ones for the rest-mass density and the energy density :

$$\begin{aligned} \partial_t \bar{\rho}_k &= -3 \frac{\dot{a}}{a} \bar{\rho}_k = \bar{\alpha} \bar{K} \bar{\rho}_k, \\ \partial_t \bar{e}_k &= -3 \frac{\dot{a}}{a} (\bar{e}_k + \bar{p}_k) = \bar{\alpha} \bar{K} (\bar{e}_k + \bar{p}_k), \end{aligned}$$

where $\bar{K} = -\frac{3}{\alpha} \frac{\dot{a}}{a}$ is the trace of the homogeneous extrinsic curvature. Indeed, the other hydrodynamical variables can be recovered by using only the equation of state because the velocity \bar{v}_k^f is null and the Lorentz factor is thus equal to 1.

1.8 The linearized equations

We end this chapter by giving the equations derived from the linear perturbation theory, in the comoving gauge, when only one fluid is considered. This solution is computed to have a point of comparison with the BSSN one. We do not recall all the development but simply give the final equations. We base ourselves on [Padmanabhan 1993].

The principle is to perturb the background solution by writing

$$e = \bar{e} + \delta e, \quad (1.8.1)$$

$$p = \bar{p} + \delta p, \quad (1.8.2)$$

$$H_l = H + \delta H, \quad (1.8.3)$$

where we introduced a local Hubble factor H_l , obtained by perturbing the background Hubble factor $\frac{\dot{a}}{a}$.

Working in the comoving gauge and keeping only terms linear in the perturbations gives the following equations :

$$\delta \dot{e} = -3H \delta e - 3(\bar{e} + \bar{p}) \delta H, \quad (1.8.4)$$

$$\delta \dot{H} = -2H \delta H - \frac{4\pi G}{3} \delta e - \frac{1}{3} \frac{\nabla^2 \delta p}{(\bar{e} + \bar{p})}. \quad (1.8.5)$$

If we use the linear equation of state $p = \omega e$, we have $\delta p = \omega \delta e$ and we can eliminate δH to obtain a single second order equation for $\delta := \frac{\delta e}{\bar{e}}$:

$$\ddot{\delta} + (2 - 3\omega) H \dot{\delta} - \frac{3}{2} H^2 (1 + 2\omega - 3\omega^2) \delta = \omega \nabla^2 \delta. \quad (1.8.6)$$

Now we have developed the evolution equations in the suitable form, we are ready for their numerical treatment. The next chapter is devoted to the building of a numerical integration code.

Chapter 2

Building of a Numerical Code

Summary

This chapter is devoted to the numerical code used in this thesis. We present here the questions that need to be considered before the building of such a code. It starts with the choice of the formalism, the method to be implemented and the gauge conditions. Indeed, there exists several formalisms to cast the problem and many different numerical methods to perform simulations (see [Baumgarte and Shapiro 2010],[Alcubierre 2008], [Rezzolla and Zanotti 2013], [Shibata 2016], [Gourgoulhon 2012]). The choice of the most appropriate combination formalism-algorithm-gauge is thus the first step. The next step concerns the way of building the initial data. This can be numerically difficult and sometimes requires advanced algorithmic methods. We must find initial data that give a good representation of the situation we want to simulate, e. g. initial data for binary systems are a large field of research (see [Gourgoulhon 2012] for an brief overview). But these inputs must also be a solution of General Relativity at initial time, i. e. the Hamiltonian constraint must be theoretically and numerically as accurately verified as possible. We here give two different approaches to this problem. We first expose a simple but efficient method, used in [Rekier et al. 2015], which consists in taking a conformally flat spacetime at initial time and deriving the curvature and density profiles through the Hamiltonian constraint. Secondly, we develop the analytical long-wavelength solution based on the gradient expansion in a general Bona-Masso slicing. This derivation constitutes an original theoretical result of this thesis and gives more realistic initial data, though less exact strictly mathematically speaking since it is an approximate solution. The last part of this chapter is devoted to the validation of the code, an essential step in the development of such a numerical work.

2.1 Choice of the formalism

The first step is, obviously, the determination of which form of the equations is required for the numerical treatment. No prescription should generally be preferred to the others; it depends on the situation and the symmetries of the problem. Since we are studying the cosmological spherical collapse, it is convenient to work in spherical coordinates with the spherical symmetry. But choosing the BSSN formalism described in Chapter 1 is less obvious. Indeed, there exist other formalisms specially adapted to spherical symmetry and, among them, the Misner-Sharp formulation [Misner 1964] has been frequently used to study primordial black holes formation. These equations have the advantage not to require a special treatment of the hydrodynamic equations since they are considerably simplified. However, this formulation is exclusively written in what is called the *comoving gauge*, for which the worldlines of the fluid coincide with the curves of constant spatial coordinates and are orthogonal to the slicing, i.e. $n^\mu = u^\mu$ and $v^i = 0$. Such a gauge is possible when dealing with one perfect fluid but is meaningless when several fluids with relative velocities are considered. So, if a comoving gauge does exist, the Misner-Sharp formulation is a really good and simpler alternative to BSSN equations. But as discussed in the introduction, within the frame of this thesis, the initial idea was to upgrade the BSSN code built and used in [Rekier et al. 2015],[Rekier et al. 2016] and [Rekier 2015] by allowing the possibility of running the code with two different fluids of pressured matter. This is why we choose to work with the BSSN equations coupled with the Valencia formulation of the hydrodynamics.

2.2 The implementation

To solve the hydrodynamical and BSSN equations, we use the same method as in [Rekier et al. 2015] (and first developed in [Montero and Cordero-Carrion 2012]). The radial dimension is discretised by a uniformly cell-centred grid. It must be noted that it is equally customary to use an adaptive mesh refinement method ([Berger and Olinger 1984] and [Berger and Colella 1989]) to obtain a very high resolution in regions where it is needed without imposing it on the entire grid. Such schemes have been used in many critical collapse researches such as [Choptuik 1993] and [Musco and Miller 2013] for example. We do not use such scheme since the code seems to be robust enough for its required utilisation.

2.2.1 The PIRK algorithm

A fourth-order finite difference scheme is used to compute radial derivatives and we use fourth-order Kreiss-Olinger dissipation. A few virtual points of negative radius are added to the grid to improve stability for the radial derivatives close to the origin by using parity conditions on the fields.

We use the PIRK algorithm (for *Partially Implicit Runge-Kutta*) to solve the evo-

lution equations. To achieve it, we split the set of equations in two parts :

$$\begin{cases} \partial_t u = \mathcal{L}_1(u, v), \\ \partial_t v = \mathcal{L}_2(u) + \mathcal{L}_3(u, v). \end{cases} \quad (2.2.1)$$

The variables u are first explicitly evolved and the result is used to evolve v partially implicitly through the operator \mathcal{L}_2 . Since it is a second order PIRK method, the evolution requires two steps which are described in details in [Montero and Cordero-Carrion 2012]. In particular, if we denote by L_1 , L_2 and L_3 the corresponding discrete operators of \mathcal{L}_1 , \mathcal{L}_2 and \mathcal{L}_3 , the operators L_1 and L_3 are used in an explicit way, while L_2 contains the unstable terms and is treated in a partially implicit way. The splitting has been chosen to ensure the scheme to be as stable as possible (see [Rekier et al. 2015]). In the first step, the hydrodynamical conserved variables, the cosmological scale factor a , the lapse α , the elements of the conformal 3-metric \hat{a} and \hat{b} and ψ are evolved explicitly. These are thus included in the L_1 operator. In the second step, the extrinsic curvature is evolved. This means that K and A_a are split into the following L_2 and L_3 operators ⁽¹⁾ :

$$\begin{aligned} L_2(A_a) &= -\left(\nabla^r \nabla_r \alpha - \frac{1}{3} \nabla^2 \alpha\right) \\ &\quad + \alpha \left(R_r^r - \frac{1}{3} R\right), \end{aligned} \quad (2.2.2)$$

$$L_3(A_a) = \alpha K A_a - \frac{16\pi}{3} (S_a - S_b), \quad (2.2.3)$$

$$L_2(K) = -\nabla^2 \alpha, \quad (2.2.4)$$

$$\begin{aligned} L_3(K) &= \alpha \left(A_a^2 + 2A_b^2 + \frac{1}{3} K^2\right) \\ &\quad + 4\pi \alpha (E + S_a + 2S_b). \end{aligned} \quad (2.2.5)$$

Finally, the auxiliary variable $\hat{\Delta}^r$ is evolved partially implicitly :

$$\begin{aligned} L_2(\hat{\Delta}^r) &= -\frac{2}{\hat{a}} (A_a \partial_r \alpha + \alpha \partial_r A_a) - \frac{4\alpha}{r \hat{b}} (A_a - A_b) \\ &\quad + \frac{\xi \alpha}{\hat{a}} \left[\partial_r A_a - \frac{2}{3} \partial_r K + 6A_a \frac{\partial_r \psi}{\psi} \right. \\ &\quad \left. + (A_a - A_b) \left(\frac{2}{r} + \frac{\partial_r \hat{b}}{\hat{b}} \right) \right], \end{aligned} \quad (2.2.6)$$

$$L_3(\hat{\Delta}^r) = 2\alpha A_a \hat{\Delta}^r - 8\pi j_r \frac{\xi \alpha}{\hat{a}}. \quad (2.2.7)$$

Note that general expressions can be found in [Montero and Cordero-Carrion 2012].

⁽¹⁾The terms of R_r^r and R which are proportional to $\hat{\Delta}^r$ and $\partial_r \hat{\Delta}^r$ are in fact included in the $L_3(A_a)$ operator instead of $L_2(A_a)$.

This method, which does not require any regularization, has already been used in the frame of BSSN formalism under asymptotically flatness assumption (see [Baumgarte et al. 2013]). It has also been applied for a dynamical cosmological background in [Rekier et al. 2015] and [Rekier et al. 2016], but it was restricted to the case of dust matter (pressure-less matter) and scalar field, and so it did not really include the full hydrodynamic equations.

2.2.2 A HRSC method for the hydrodynamics

Concerning the hydrodynamic equations, a careful treatment must be taken since we are working in a non comoving gauge and with pressured fluids. To solve them, we use a Godunov type method. It is part of an important class of conservative numerical methods : the High-Resolution Shock-Capturing (HRSC) methods (see [Rezzolla and Zanotti 2013] and [Alcubierre 2008]). These methods are specially designed to deal efficiently with discontinuous solutions and generally do not require adaptive mesh refinement [Rezzolla and Zanotti 2013].

To explain how it works, let us consider the problem in the case of the standard one-spatial dimensional conservation equation and adopt the same notations as [Rezzolla and Zanotti 2013] :

$$\partial_t \mathbf{U} + \partial_x \mathbf{F}(\mathbf{U}) = 0. \quad (2.2.8)$$

Assume each time-slice is spatially discretized into J cells $I_j = [x_{j-1/2}, x_{j+1/2}]$, with $j = 1, \dots, J$. The resulting numerical scheme is of the form

$$\mathbf{U}_j^{n+1} = \mathbf{U}_j^n + \frac{\Delta t}{\Delta x} (\mathbf{F}_{j-1/2} - \mathbf{F}_{j+1/2}), \quad (2.2.9)$$

where the numerical fluxes are computed in such a way :

$$\mathbf{F}_{j\pm 1/2} := \frac{1}{\Delta t} \int_{t^n}^{t^{n+1}} \mathbf{F}[\mathbf{U}(x_{j\pm 1/2}, t)] dt. \quad (2.2.10)$$

The way these fluxes are computed is determined by the method that is used. The idea of Godunov methods is to discretize the continuous solution as a constant value in each cell, corresponding to its volume-average. The function \mathbf{U} is seen as a series of piecewise-constant states generating a local Riemann problem at each interface between adjacent cells. Recall that a Riemann problem is a initial-value problem such as (2.2.8) with initial conditions of the form

$$\mathbf{U}(x, 0) = \begin{cases} \mathbf{U}_L & \text{if } x < 0, \\ \mathbf{U}_R & \text{if } x > 0, \end{cases} \quad (2.2.11)$$

where \mathbf{U}_L and \mathbf{U}_R are constant values called *left* state and *right* state, respectively.

Thus, the numerical fluxes in any Godunov method must be computed by solving the corresponding local Riemann problem. To achieve it, three steps must be performed, each leading to a large panel of numerical methods [Rezzolla and Zanotti 2013] :

1. The reconstruction of the left and right states of the local Riemann problem. Initially, Godunov used the center value of the state as boundary values for each cells :

$$\mathbf{U}(x, t^n) = \begin{cases} \mathbf{U}_j^n & \text{if } x < x_{j+1/2}, \\ \mathbf{U}_{j+1}^n & \text{if } x > x_{j+1/2}, \end{cases} \quad (2.2.12)$$

Unfortunately, doing this has the consequence that a lot of information concerning the behaviour inside the cells is lost. To limit this effect, the so called *reconstruction techniques* give a better estimation of the left and right states, improving the accuracy of the method.

2. The computation of the numerical fluxes by the use of an approximate Riemann solver.
3. The time evolution of the solution by the use of an at least second order evolution algorithm.

For our purposes, we use a monotonised central-difference (MC) slope limiter (see [Leer 1977]) to approximate the left and right states of the primitive variables at each cell. It consists in a piecewise-linear reconstruction given by

$$\mathbf{U}_j^n(x) = \mathbf{U}_j^n + \sigma_j^n(x - x_j), \quad \text{for } x_{j-1/2} \leq x \leq x_{j+1/2}, \quad (2.2.13)$$

with the slope

$$\sigma_j^n := \text{minmod} \left(\frac{\mathbf{U}_{j+1}^n - \mathbf{U}_{j-1}^n}{2\Delta x}, 2 \frac{\mathbf{U}_j^n - \mathbf{U}_{j-1}^n}{\Delta x}, 2 \frac{\mathbf{U}_{j+1}^n - \mathbf{U}_j^n}{\Delta x} \right), \quad (2.2.14)$$

where the minmod function is given by

$$\text{minmod}(\alpha, \beta, \gamma) := \begin{cases} \min(\alpha, \beta, \gamma) & \text{if } \alpha, \beta, \gamma > 0, \\ \max(\alpha, \beta, \gamma) & \text{if } \alpha, \beta, \gamma < 0, \\ 0 & \text{otherwise.} \end{cases} \quad (2.2.15)$$

Note that we can reconstruct equally either the primitive variables or the conserved ones since we are using a finite-difference conservative scheme. If we were using a finite-volume method, we could only apply the reconstruction on the conserved variables (see [Rezzolla and Zanotti 2013]). In our case, we apply it to the primitive ones.

We then solve the equations with a HLLC incomplete Riemann solver, named after Harten, Lax, van Leer and Einfeldt (see [Harten et al. 1983] and [Einfeldt 1988]). Its idea is to suppose that evolution of the discontinuity of the Riemann problem generates only two waves, propagating in opposite directions with velocities $\lambda_L \leq 0$ and $\lambda_R \geq 0$ and leaving only one constant state between them :

$$\mathbf{U}(x, t) = \begin{cases} \mathbf{U}_L & \text{if } x/t < \lambda_L, \\ \mathbf{U}^{HLLC} & \text{if } \lambda_L < x/t < \lambda_R, \\ \mathbf{U}_R & \text{if } x/t > \lambda_R. \end{cases} \quad (2.2.16)$$

The velocities λ_L and λ_R are taken as the smallest and the largest of the characteristic speeds of the solution :

$$\lambda_L := \min(0, \lambda_-(\mathbf{U}_L), \lambda_-(\mathbf{U}_R)), \quad (2.2.17)$$

$$\lambda_R := \max(0, \lambda_+(\mathbf{U}_L), \lambda_+(\mathbf{U}_R)), \quad (2.2.18)$$

$$(2.2.19)$$

where $\lambda_{\pm}(\mathbf{U})$ are eigenvalues of the Jacobian of the flux vectors $\frac{\partial \mathbf{F}^x}{\partial \mathbf{U}}$:

$$\lambda_{\pm} = \frac{\alpha}{1 - v^2 c_s^2} \left[v^x (1 - c_s^2) \pm c_s \sqrt{(1 - v^2)(\gamma^{xx}(1 - v^2 c_s^2) - v^x v^x (1 - c_s^2))} \right] - \beta^x, \quad (2.2.20)$$

where we have introduced the sound speed $c_s^2 = \frac{\partial p}{\partial e}$, which depends on the equation of state.

Finally, the resulting fluxes are given by

$$\mathbf{F}(x, t) = \begin{cases} \mathbf{F}_L & \text{if } x/t < \lambda_L, \\ \mathbf{F}^{HLL E} & \text{if } \lambda_L < x/t < \lambda_R, \\ \mathbf{F}_R & \text{if } x/t > \lambda_R. \end{cases} \quad (2.2.21)$$

where

$$\mathbf{F}^{HLL E} := \frac{\lambda_R \mathbf{F}_L - \lambda_L \mathbf{F}_R + \lambda_L \lambda_R (\mathbf{U}_R - \mathbf{U}_L)}{\lambda_R - \lambda_L}. \quad (2.2.22)$$

Since we already described the evolution algorithm above, it remains to consider the recovering of the primitive variables.

2.2.3 Recovering the primitive variables

If the equation of state is different from (1.6.3), we use a root-finding procedure (Newton-Raphson) to recover the primitive variables from the conserved ones since it cannot be done analytically. But if we work with the equation of state (1.6.3), the situation is far more easier. Recall that the conserved variables are defined in such a way :

$$\begin{cases} D &= \rho W \\ S_i &= (e + p) W^2 v_i \\ \tau &= (e + p) W^2 - p - D \end{cases} \quad (2.2.23)$$

where the rest-mass density ρ , the energy density e , the pressure p , the velocity v_i and the Lorentz factor $W = \frac{1}{\sqrt{1 - v^2}}$ are the primitive variables. In the case of the barotropic equation of state $p = \omega e$, this relation can be inverted analytically. To obtain it, we start by squaring the second equation of (2.2.23) :

$$S^2 := S^i S_i = (e + p)^2 W^4 v^2. \quad (2.2.24)$$

Recalling that $v^2 = 1 - \frac{1}{W^2}$, (2.2.24) becomes

$$S^2 = (e + p)^2 W^4 - (e + p)^2 W^2. \quad (2.2.25)$$

The third equation of (2.2.23) gives

$$\begin{aligned}(e+p)^2 W^4 &= (\tau + D + p)^2 \\ (e+p)^2 W^2 &= (e+p)(\tau + D + p).\end{aligned}$$

Reinserting in (2.2.25) gives the relation⁽²⁾

$$S^2 = (\tau + D)^2 + (\tau + D)(p - e) - pe. \quad (2.2.26)$$

Using now the equation of state $p = \omega e$, we obtain a quadratic equation in e :

$$-\omega e^2 + (\omega - 1)(\tau + D)e + (\tau + D)^2 - S^2 = 0. \quad (2.2.27)$$

Its solutions are

$$e = (\tau + D) - \frac{S^2}{\tau + D}, \quad \text{if } \omega = 0, \quad (2.2.28)$$

and

$$e = \tau + D, \quad \text{if } \omega = -1, \quad (2.2.29)$$

and

$$e_{\pm} = \frac{(\omega - 1)(\tau + D) \pm \sqrt{(\omega + 1)(\tau + D)^2 - 4\omega S^2}}{2\omega}, \quad \text{if } \omega \neq 0, \quad (2.2.30)$$

The sign we have to consider depends on the value of ω .

If $0 < \omega \leq 1$, we have $(\omega - 1)(\tau + D) \leq 0$ and thus we have to take the plus sign to keep a non negative energy density.

If $\omega > 1$, the positivity of the interior of the root and the fact that

$$(\omega + 1)(\tau + D)^2 - 4\omega S^2 \leq (\omega + 1)[(\tau + D)^2 - S^2] \quad (2.2.31)$$

imply that

$$e_+ e_- = \frac{(\tau + D)^2 - S^2}{-\omega} \leq 0, \quad (2.2.32)$$

where the equality holds if and only if $e = 0$. The latter case is trivial, because it requires $D = 0$, $S_i = 0$ and $\tau = 0$, and in the other cases, this means that the solutions e_+ and e_- have opposite signs and that only one is positive.

If $\omega < 0$, the situation is less obvious because both solutions can be positive. For example, if $\omega \in]-1; 0[$, we have

$$\begin{aligned}e_+ e_- &= \frac{(\tau + D)^2 - S^2}{-\omega} \\ &= \frac{((e+p)W^2 - p)^2 - (e+p)^2 W^4 v^2}{-\omega}\end{aligned}$$

⁽²⁾Note that this relation is correct whatever the equation of state and does not requires spherical symmetry.

$$\begin{aligned}
&= \frac{((\omega + 1)^2 W^4 + \omega^2 - 2\omega(\omega + 1)W^2) e^2}{-\omega} \\
&\quad - \frac{(\omega + 1)^2 W^4 v^2 e^2}{-\omega} \\
&= \frac{[(\omega + 1)^2 W^4 (1 - v^2) + \omega^2 - 2\omega(\omega + 1)W^2] e^2}{-\omega} \\
&> 0,
\end{aligned}$$

because all the terms of the numerator are positive. This means that both solutions have the same sign and thus are positive. The choice must be done thanks to the supposed continuity of the solution with time, which can be difficult numerically.

Once the energy density e is computed, the other variables follow easily :

$$p = \omega e \quad (2.2.33)$$

$$W = \sqrt{\frac{\tau + D + p}{e + p}} \quad (2.2.34)$$

$$v_i = \frac{S_i}{(e + p)W^2} \quad (2.2.35)$$

$$\rho = \frac{D}{W}. \quad (2.2.36)$$

2.3 Boundary and gauge conditions

Once the numerical method has been chosen, we need to choose the correct conditions to impose on the boundary points of our grid. This has a great importance since it will rule the behaviour of signals at those boundaries. The question of the slicing conditions must also be decided.

2.3.1 Boundary conditions

The spatial domain is of the form $r \in [0, r_{\text{grid}}]$, where 0 corresponds to the origin and r_{grid} to the outer boundary. We use a cell-centered discretization to avoid calculations at the exact origin in case of singularities. At the origin, we impose, following spherical symmetry, the inhomogeneous variables to have the correct parity for a regular solution thanks to a few virtual points of negative radius we added to the grid.

At the outer boundary, we use a Sommerfeld (radiative) boundary conditions (see [Alcubierre et al. 2003]) : we impose the variables to behave like outward travelling waves when r is near r_{grid} . This means that, at a few outermost points of the computational grid, any field $f(t, r)$ must verify

$$\partial_t f = \partial_t \bar{f} - v \partial_r f - \frac{v}{r} (f - \bar{f}), \quad (2.3.1)$$

where v is the characteristic velocity of the field. Note that v is computed by examining the dynamical equation of each field and is the speed of light for most of it. Only the

lapse α and the variable $\hat{\Delta}^r$ admit a characteristic velocity different from it. For the lapse, it depends on the slicing that is used (see 2.3.2) while it is $\sqrt{2}$ for $\hat{\Delta}^r$. Such a condition prevents any signal to be reflected by the outer boundary, which would highly impact the validity of the solution. We found this condition not to always work perfectly and that it can be at the origin of damaging numerical errors. But, when there is some doubt in its reliability, taking a grid large enough is an efficient solution to avoid any numerical noise coming from the outer boundary to perturb the local evolution. The asymptotic values of each variable are the homogeneous ones given by the background evolution :

$$\alpha(t, r) \rightarrow \bar{\alpha}(t), \quad (2.3.2)$$

$$\hat{a}(t, r), \hat{b}(t, r), \psi(t, r) \rightarrow 1, \quad (2.3.3)$$

$$K(t, r) \rightarrow \bar{K}(t) = -\frac{3}{\alpha} \frac{\dot{a}}{a}, \quad (2.3.4)$$

$$A_a(t, r), A_b(t, r), \hat{\Delta}^r(t, r) \rightarrow 0, \quad (2.3.5)$$

$$\rho_k(t, r) \rightarrow \bar{\rho}_k(t), \quad (2.3.6)$$

$$e_k(t, r) \rightarrow \bar{e}_k(t), \quad (2.3.7)$$

$$v_k^r(t, r) \rightarrow 0. \quad (2.3.8)$$

2.3.2 Slicing conditions

There are lots of different slicing conditions in the literature (see for example [Gourgoulhon 2012], [Baumgarte and Shapiro 2010] or [Shibata 2016]). We implemented the Bona-Masso slicing ([Bona et al. 1995]) for the local dynamics and the geodesic slicing (constant unity lapse) for the background :

$$\partial_t \alpha = -\alpha^2 f(\alpha) (K - \bar{K}), \quad (2.3.9)$$

$$\bar{\alpha} = 1. \quad (2.3.10)$$

We differ a bit from what was made in [Rekier et al. 2015] and [Rekier et al. 2016]. They considered a slicing condition that did not converge to the geodesic one at spatial infinity. Our slicing conditions are thus not exactly the same, we added the $-\bar{K}$ in our equation to ensure that $\alpha \rightarrow 1$ as $r \rightarrow \infty$. This allows identifying the time coordinate to the cosmological synchronous time for physical interpretations. Such a slicing condition gives a characteristic velocity for the lapse of $\alpha \sqrt{f(\alpha)} \gamma^{rr}$ (see [Alcubierre 2008]), which is equal to $\frac{\sqrt{f(\alpha=1)}}{a}$ at spatial infinity. This quantity must then be taken in the Sommerfeld conditions of (2.3.1).

Choosing $f \leq \frac{1}{3}$ implies that the coordinate speed of light remains finite (see [Torres et al. 2014]). Thus, this condition ensures to keep the stability of the scheme though not mandatory.

The simplest choice $f = 0$ is the geodesic slicing $\alpha = 1$. Combined with a zero shift $\beta = 0$ gives what is called the *synchronous gauge*. Although this is not the best choice in term of stability - it easily generates coordinate singularities (see [Gourgoulhon 2012]) - we chose this one in some of our simulations because of its simplicity. Table 2.1 summarizes the different slicing conditions used in this thesis.

Name	$f(\alpha)$
geodesic	0
harmonic	1
1/3	1/3
1 + log	2/ α

Table 2.1 – Different slicing conditions used in this thesis, following the Bona-Masso slicing (2.3.9).

2.4 The question of the initial data

Another important information needed to perform numerical simulations is the situation at initial time. There are two ways of setting the initial conditions : either we choose well determined values for almost all the variables and derive the last ones with the constraint equations (1.4.11), or we choose initial conditions following a good approximation of the solution modelling the situation at early times. The first method has the advantage to start with, theoretically, an exact solution of general relativity since the constraint equations are verified at initial time. But the initial data generated in this way can be viewed as quite artificial and could suffer from transient effects at early times before reaching a more realistic evolution. The second method has opposite properties. It generates a more realistic initial situation from the physical point of view but this is generally only an approximation of the exact solution and then needs some iterations for the constraints to reach a more acceptable level of accuracy. We start by exhibiting the first method in a simple but useful case.

2.4.1 A conformally flat metric as initial data

This idea here is to assume spatial homogeneity on each metric variables except the conformal factor and thus to equal them to their corresponding background values :

$$\alpha(t=0, r) = 1, \quad (2.4.1)$$

$$\hat{a}(t=0, r) = \hat{b}(t=0) = 1, \quad (2.4.2)$$

$$K(t=0, r) = \bar{K}_i = -3H_i, \quad (2.4.3)$$

$$A_a(t=0, r) = A_b(t=0, r) = 0, \quad (2.4.4)$$

$$\hat{\Delta}^r(t=0, r) = 0, \quad (2.4.5)$$

where \bar{K}_i is the initial background curvature and H_i the initial Hubble factor.

Concerning the matter source terms, the Momentum constraint (1.4.11) reduces to $j^r(t=0, r) = 0$. This imposes a null spatial 3-velocity :

$$v_k^r(t=0, r) = 0.$$

Note that in the case of several fluids, the condition $j^r(t=0, r) = 0$ is weaker than $v_k^r(t=0, r) = 0$ for all k . But other possibilities are much more complicated and, we think, naturally improbable.

Since we will work with the cosmological equation of state $p = \omega e$, we do not need to use the rest-mass density quantity ρ . Only two last quantities thus remain to be specified : the energy density and the initial curvature, i.e. the conformal factor. Both are linked by the Hamiltonian constraint :

$$-a^{-2}\psi^{-5} \left(\partial_r^2 \psi + \frac{2}{r} \partial_r \psi \right) + \frac{3}{4} H_i^2 = 2\pi E(t=0, r). \quad (2.4.6)$$

So, specifying one determines the other. Intuitively, the physicist prefers to introduce a specific energy-density profile to model a situation. This is what was done in [Rekier et al. 2015], [Rekier et al. 2016] and [Shibata and Sasaki 1999]. The initial conformal factor $\psi(t=0, r)$ is then found by solving numerically (2.4.6) as a boundary value problem with

$$\partial_r \psi \rightarrow 0, \quad \text{for } r \rightarrow 0; \quad (2.4.7)$$

$$\psi \rightarrow 1 + \frac{C_\psi}{2r}, \quad \text{for } r \rightarrow \infty, \quad (2.4.8)$$

where C_ψ is adjusted such that

$$\partial_r \psi \rightarrow -\frac{C_\psi}{2r^2}, \quad \text{for } r \rightarrow \infty. \quad (2.4.9)$$

This method is used successfully in section 2.6 and in all the following chapter. We specify the initial energy density in terms of the energy density contrast $\delta_k^i(r) = \frac{e_k(t=0, r)}{\bar{e}_k(t=0)} - 1$. We use a smooth top-hat profile (a logistic function) to simulate the evolution of an over-dense region of the universe :

$$\delta_k^i(r) = \delta_k^i \frac{1 - \tanh\left(\frac{r-r_k^i}{2\sigma_k}\right)}{1 + \tanh\left(\frac{r_k^i}{2\sigma_k}\right)}, \quad (2.4.10)$$

where δ_k^i , r_k^i and σ_k are positive parameters designing the shape of the profile.

We must here make an important remark. Such a boundary value problem can be hard to solve numerically and requires a solid numerical algorithm we will not present here. For example, the routine we used, though known to be robust, was not able to generate initial conditions sufficiently compact to form primordial black holes with a fluid of radiation. The reason is probably because, as we told previously, taking a conformally flat metric at initial time is not realistic and the contrast between such metric and a strong gravitational field induced by a compact matter profiles must sometimes be too large to allow computation. The other solution is to specify the initial conformal factor and deduce the corresponding energy density profiles. If we work in a one fluid context, this is far more easier than the first method since the energy density is straightly given by equation (2.4.6) and thus no boundary value problem must be solved. This can seem less intuitive but actually it makes no real difference. Einstein equations make the equivalence between the geometry of spacetime and the energy it contains. So, specifying one or the other is mathematically equivalent. Such

approach has already been used within the frame of primordial black holes formation in [Polnarev and Musco 2007], [Musco and Miller 2013] and [Musco 2019]⁽³⁾. We use it in Chapter 4 to obtain sufficiently compact initial data to form black holes with a radiation fluid. Note that if several fluids are used, this method only determines the total initial energy density $e_i = \sum_k e_k(t=0, r)$, the initial repartition of density for each fluid remains free and must only verify the background repartition at spatial infinity. Two repartitions could nevertheless be pointed out : either homogeneous fluids except one that would then be entirely responsible for the initial inhomogeneous curvature, or the background proportions $\Omega_k^i = \frac{\bar{e}_k(t=0)}{\bar{e}_i}$ conserved everywhere, which would maybe give a more realistic situation.

We present here a useful particular solution when the conformal factor is written in an exponential form :

$$\psi = e^{\frac{\zeta}{2}}.$$

By replacing it in the Hamiltonian constrain (2.4.6), we obtain

$$\delta_i(r) = -\frac{2}{3} \left(\frac{1}{a_i H_i} \right)^2 e^{-2\zeta} \left(\zeta'' + \zeta' \left(\frac{2}{r} + \frac{\zeta}{2} \right) \right), \quad (2.4.11)$$

where a_i is the initial cosmological scale factor and H_i the initial Hubble factor. We follow [Musco 2019] and take a Gaussian profile for ζ :

$$\zeta(r) = A \exp \left(-\frac{r^2}{2\Delta^2} \right), \quad (2.4.12)$$

where A and Δ are positive parameters. Such a profile is known to produce a nearly Mexican Hat shape for the density contrast and is thus particularly adapted to simulate the evolution of an inhomogeneity. The profile in this case is given by

$$\delta_i(r) = \frac{2\zeta}{\Delta^2} \left(\frac{1}{a_i H_i} \right)^2 e^{-2\zeta} \left(1 - \frac{r^2}{3\Delta^2} \left(1 + \frac{\zeta}{2} \right) \right). \quad (2.4.13)$$

2.4.2 The long-wavelength approximation as initial data

To generate more realistic initial conditions, we can use the long-wavelength approach (also called *gradient expansion*), as described in [Lyth et al. 2005], [Harada et al. 2015] and [Musco 2019]. This approach resembles the cosmological perturbation theory but, instead of developing the equations in powers of the inhomogeneities as in the lattice, the long-wavelength scheme expands the solution in the spatial gradient of these perturbations. Concretely, we focus on some fixed time, multiply each spatial gradient ∂_i by a fictitious parameter $\varepsilon \ll 1$ and we expand the equations in a power

⁽³⁾The papers mentioned here indeed specify first the curvature and then deduce the energy density profile. But it must be said that they all use realistic initial conditions computed from linearized evolution equations. They thus do not enter fully in the field of this section 2.4.1.

series of ε . We keep terms up to first-order in ε and then set $\varepsilon = 1$. To compare, in the perturbative approach the parameter ε would multiply the perturbation instead of ∂_i .

The parameter ε is conveniently identified as the ratio

$$\varepsilon := \frac{R_H(t)}{L}, \quad (2.4.14)$$

where $R_H(t) = \frac{1}{H(t)}$ is the Hubble radius, the only geometrical scale in the homogeneous universe, and L is the (comoving) length scale of the perturbation. This approach reproduces the results of linear perturbation theory but can also consider non linear perturbations of the curvature if the universe is sufficiently smooth for scales greater than L (see [Lyth et al. 2005] and [Musco 2019]).

We assume that, at fixed time, the universe becomes locally flat homogeneous and isotropic in the limit $\varepsilon \rightarrow 0$. We thus assume, still following [Lyth et al. 2005], that $\hat{\gamma}_{ij} = O(\varepsilon^2)$. As described in details in [Harada et al. 2015], we then obtain

$$\psi = O(\varepsilon^0), \quad (2.4.15)$$

$$v^i = O(\varepsilon), \quad (2.4.16)$$

$$v_i = O(\varepsilon^3), \quad (2.4.17)$$

$$D_i v^i = O(\varepsilon^4), \quad (2.4.18)$$

$$W = 1 + O(\varepsilon^6), \quad (2.4.19)$$

$$\delta = O(\varepsilon^2), \quad (2.4.20)$$

$$\hat{A}_{ij} = O(\varepsilon^2), \quad (2.4.21)$$

$$h_{ij} = O(\varepsilon^2), \quad (2.4.22)$$

$$\chi = O(\varepsilon^2), \quad (2.4.23)$$

$$\kappa = O(\varepsilon^2), \quad (2.4.24)$$

where we used the following notations

$$\delta := \frac{e - \bar{e}}{\bar{e}},$$

$$h_{ij} := \hat{\gamma}_{ij} - \bar{\gamma}_{ij},$$

$$\chi := \alpha - 1,$$

$$\kappa := \frac{K - \bar{K}}{\bar{K}}.$$

Moreover, the conformal factor can be decomposed in such a way :

$$\psi(t, x^i) = \Psi(x^i) (1 + \xi(t, x^i)), \quad (2.4.25)$$

where $\Psi = O(\varepsilon^0)$ and $\xi = O(\varepsilon^2)$. In fact, as also shown in [Lyth et al. 2005] and [Harada et al. 2015], all slicings coincide up to $O(\varepsilon)$, which allows to apply the long-wavelength scheme in any slicing. After having done it in the special case where $p = \omega e$, the evolution equations become

$$\dot{\delta} + 6\dot{\xi} + 3H\omega(\chi + \kappa) = O(\varepsilon^4), \quad (2.4.26)$$

$$\frac{1}{1+\omega}\dot{\delta} + 6\dot{\xi} = O(\varepsilon^4), \quad (2.4.27)$$

$$\partial_t(a^3(1+\omega)\bar{e}u_i) = -a^3\bar{e}[\omega\partial_t\delta + (1+\omega)\partial_t\chi] + O(\varepsilon^5), \quad (2.4.28)$$

$$\bar{\Delta}\Psi = -2\pi\Psi^5 a^2\bar{e}(\delta - 2\kappa) + O(\varepsilon^4), \quad (2.4.29)$$

$$H^{-1}\dot{\kappa} = \frac{3\omega-1}{2}\kappa - \frac{3(1+\omega)}{2}\chi - \frac{1+3\omega}{2}\delta + O(\varepsilon^4), \quad (2.4.30)$$

$$\partial_t h_{ij} = -2\hat{A}_{ij} + O(\varepsilon^4), \quad (2.4.31)$$

$$\begin{aligned} \partial_t \hat{A}_{ij} + 3H\hat{A}_{ij} = & \frac{1}{a^2\Psi^4} \left[-\frac{2}{\Psi} \left(\bar{D}_i \bar{D}_j \Psi - \frac{1}{3} \bar{\gamma}_{ij} \bar{\Delta} \Psi \right) \right. \\ & \left. + \frac{6}{\Psi^2} \left(\bar{D}_i \Psi \bar{D}_j \Psi - \frac{1}{3} \bar{\gamma}_{ij} \bar{D}^k \Psi \bar{D}_k \Psi \right) \right] + O(\varepsilon^4), \end{aligned} \quad (2.4.32)$$

$$\bar{D}_i \left(\Psi^6 \hat{A}_j^i \right) + 2H\Psi^6 \bar{D}_j \kappa = 8\pi\Psi^6 (1+\omega)\bar{e}u_j + O(\varepsilon^5), \quad (2.4.33)$$

where \bar{D} and $\bar{\Delta}$ are the covariant derivative and the Laplacian operators related to the flat metric written in the coordinates $\{x^i\}$. In spherical coordinates, we have that this metric is given by $\bar{\gamma}_{ij} = \text{diag}(1, r^2, r^2 \sin^2 \theta)$. The resulting equations have been solved in [Harada et al. 2015] for the constant mean curvature (CMC) slicing (for which $K = \bar{K}$), the comoving slicing, the uniform-density slicing (for which $\delta = 0$) and the geodesic slicing. The paper also gives comparison of the solutions between these four slicings. In our case, we will solve them for a general Bona-Masso slicing (2.3.9). This solution has, to our knowledge, never been derived in the literature and thus constitutes an original result in this thesis.

We start with the computation of the variables \hat{A}_{ij} and h_{ij} which, as explained in [Harada et al. 2015], do not depend on the slicing to $O(\varepsilon^2)$. If we use the intermediate variable

$$p_{ij} := \frac{1}{\Psi^4} \left[-\frac{2}{\Psi} \left(\bar{D}_i \bar{D}_j \Psi - \frac{1}{3} \bar{\gamma}_{ij} \bar{\Delta} \Psi \right) + \frac{6}{\Psi^2} \left(\bar{D}_i \Psi \bar{D}_j \Psi - \frac{1}{3} \bar{\gamma}_{ij} \bar{D}^k \Psi \bar{D}_k \Psi \right) \right], \quad (2.4.34)$$

the explicit expressions of \hat{A}_{ij} and h_{ij} are given, solving (2.4.31) and (2.4.32), by

$$\hat{A}_{ij} = \frac{2}{3\omega+5} p_{ij} H \left(\frac{1}{aH} \right)^2 + O(\varepsilon^4), \quad (2.4.35)$$

$$h_{ij} = -\frac{4}{(3\omega+5)(3\omega+1)} p_{ij} \left(\frac{1}{aH} \right)^2 + O(\varepsilon^4). \quad (2.4.36)$$

If we want to use spherical symmetry and the BSSN variables presented in Chapter 1, we must use the quantities

$$p_a := p_r^r = \frac{1}{\Psi^4} \left[-\frac{4}{3\Psi} \left(\partial_r^2 \Psi - \frac{1}{r} \partial_r \Psi \right) + \frac{4}{\Psi^2} (\partial_r \Psi)^2 \right], \quad (2.4.37)$$

$$p_b := p_\theta^\theta = \frac{1}{\Psi^4} \left[\frac{2}{3\Psi} \left(\partial_r^2 \Psi - \frac{1}{r} \partial_r \Psi \right) - \frac{2}{\Psi^2} (\partial_r \Psi)^2 \right]. \quad (2.4.38)$$

With these definitions, we can write

$$\begin{aligned} A_a &= \frac{2}{3\omega+5} p_a H \left(\frac{1}{aH} \right)^2 + O(\varepsilon^4), \\ A_b &= \frac{2}{3\omega+5} p_b H \left(\frac{1}{aH} \right)^2 + O(\varepsilon^4), \\ \hat{a} &= 1 - \frac{4}{(3\omega+5)(3\omega+1)} p_a \left(\frac{1}{aH} \right)^2 + O(\varepsilon^4), \\ \hat{b} &= 1 - \frac{4}{(3\omega+5)(3\omega+1)} p_b \left(\frac{1}{aH} \right)^2 + O(\varepsilon^4), \end{aligned}$$

where we have $p_a + 2p_b = 0$, implying the desired conditions $A_a + 2A_b = 0$ and $\hat{a}\hat{b}^2 = 1 + O(\varepsilon^4)$. The variable $\hat{\Delta}^r$ can be determined thanks to equation (1.4.5).

We will now determine the expressions for δ , ξ , κ and χ by solving equations (2.4.26), (2.4.27), (2.4.29), (2.4.30) and (2.3.9). The combination of the first two ones gives

$$H^{-1} \dot{\delta} + 3(1+\omega)(\chi + \kappa) = O(\varepsilon^4). \quad (2.4.39)$$

The Bona-Masso equation (2.3.9) reads, after being expanded around $\alpha = 1$,

$$H^{-1} \dot{\chi} = 3f(1)\kappa + O(\varepsilon^4). \quad (2.4.40)$$

With equation (2.4.30) and the change of variable $s = \ln a$, we obtain the differential linear system

$$\partial_s \begin{pmatrix} \kappa \\ \delta \\ \chi \end{pmatrix} = M(\omega) \begin{pmatrix} \kappa \\ \delta \\ \chi \end{pmatrix} + O(\varepsilon^4), \quad (2.4.41)$$

where the matrix $M(\omega)$ is given by

$$M(\omega) = \begin{pmatrix} \frac{3\omega-1}{2} & -\frac{1+3\omega}{2} & -\frac{3(1+\omega)}{2} \\ -3(1+\omega) & 0 & -3(1+\omega) \\ 3f(1) & 0 & 0 \end{pmatrix}. \quad (2.4.42)$$

This matrix admits the following eigenvalues :

$$\lambda_* = 1 + 3\omega, \quad (2.4.43)$$

$$\lambda_{\pm} = -\frac{3}{4} \left[1 + \omega \pm \sqrt{(1+\omega)(1+\omega-8f(1))} \right]. \quad (2.4.44)$$

The general solution of the system (2.4.41) is thus given by

$$\begin{pmatrix} \kappa \\ \delta \\ \chi \end{pmatrix} = C_* \mathbf{v}_* a^{\lambda_*} + C_+ \mathbf{v}_+ a^{\lambda_+} + C_- \mathbf{v}_- a^{\lambda_-} + O(\varepsilon^4), \quad (2.4.45)$$

where \mathbf{v}_* , \mathbf{v}_+ and \mathbf{v}_- are the eigenvectors associated respectively to λ_* , λ_+ and λ_- and C_* , C_+ and C_- are integration constants.

For the geodesic slicing, $\lambda_+ = -\frac{3(1+\omega)}{4} < 0$ and $\lambda_- = 0$. In the other Bona-Masso slicings of Table 2.1, λ_+ and λ_- are complex conjugates with a negative real part. Since we only take pure growing modes, we set $C_+ = C_- = 0$. We have that the eigenvector of λ_* is given by

$$\begin{pmatrix} v_*^1 \\ v_*^2 \\ v_*^3 \end{pmatrix} = \begin{pmatrix} (1+3\omega)^2 \\ -3(1+\omega)(1+3\omega+3f(1)) \\ 3(1+3\omega)f(1) \end{pmatrix}. \quad (2.4.46)$$

We can then deduce the two useful relations

$$\kappa = \frac{v_*^1}{v_*^2} \delta + O(\varepsilon^4), \quad (2.4.47)$$

$$\chi = \frac{v_*^3}{v_*^2} \delta + O(\varepsilon^4). \quad (2.4.48)$$

By inserting (2.4.47) in (2.4.29), we finally obtain

$$\delta = \frac{v_*^2}{v_*^2 - 2v_*^1} F \left(\frac{1}{aH} \right)^2 + O(\varepsilon^4), \quad (2.4.49)$$

where we have defined

$$F := -\frac{4 \overline{\Delta\Psi}}{3 \Psi^5}. \quad (2.4.50)$$

We immediately deduce the values of κ , χ and ξ thanks to (2.4.47), (2.4.48) and (2.4.27) :

$$\kappa = \frac{v_*^1}{v_*^2 - 2v_*^1} F \left(\frac{1}{aH} \right)^2 + O(\varepsilon^4), \quad (2.4.51)$$

$$\chi = \frac{v_*^3}{v_*^2 - 2v_*^1} F \left(\frac{1}{aH} \right)^2 + O(\varepsilon^4), \quad (2.4.52)$$

$$\xi = -\frac{1}{6(1+\omega)} \frac{v_*^2}{v_*^2 - 2v_*^1} F \left(\frac{1}{aH} \right)^2 + C + O(\varepsilon^4), \quad (2.4.53)$$

where the integration constant C can be absorbed into Ψ (see [Harada et al. 2015] in a similar case).

The last equation that remains to solve is (2.4.28) to find the velocity v_i . By using the expressions of δ and χ , we find

$$u_i = -\frac{2}{3\omega+5} \cdot \frac{\omega v_*^2 + (1+\omega)v_*^3}{(1+\omega)(v_*^2 - 2v_*^1)} \partial_i F \frac{1}{a} \left[\int_0^a \frac{d\tilde{a}}{H(\tilde{a})} + C \right] \left(\frac{1}{aH} \right)^2 + O(\varepsilon^5), \quad (2.4.54)$$

where the integration constant C must be set to zero to keep only growing modes (see [Harada et al. 2015]). We deduce the value for v_i :

$$v_i = -\frac{2}{3\omega+5} \cdot \frac{\omega v_*^2 + (1+\omega)v_*^3}{(1+\omega)(v_*^2 - 2v_*^1)} \partial_i Fa \left(\frac{1}{aH} \right)^3 + O(\varepsilon^5). \quad (2.4.55)$$

To summarize the results in terms of BSSN variables in spherical symmetry, the long-wavelength solution is given by

$$\psi = \Psi \left(1 - \frac{1}{6(1+\omega)} \frac{v_*^2}{v_*^2 - 2v_*^1} F \left(\frac{1}{aH} \right)^2 \right) + O(\varepsilon^4), \quad (2.4.56)$$

$$A_a = \frac{2}{3\omega+5} p_a H \left(\frac{1}{aH} \right)^2 + O(\varepsilon^4), \quad (2.4.57)$$

$$A_b = \frac{2}{3\omega+5} p_b H \left(\frac{1}{aH} \right)^2 + O(\varepsilon^4), \quad (2.4.58)$$

$$\hat{a} = 1 - \frac{4}{(3\omega+5)(3\omega+1)} p_a \left(\frac{1}{aH} \right)^2 + O(\varepsilon^4), \quad (2.4.59)$$

$$\hat{b} = 1 - \frac{4}{(3\omega+5)(3\omega+1)} p_b \left(\frac{1}{aH} \right)^2 + O(\varepsilon^4), \quad (2.4.60)$$

$$\delta = \frac{v_*^2}{v_*^2 - 2v_*^1} F \left(\frac{1}{aH} \right)^2 + O(\varepsilon^4), \quad (2.4.61)$$

$$K = \bar{K} \left(1 + \frac{v_*^1}{v_*^2 - 2v_*^1} F \left(\frac{1}{aH} \right)^2 \right) + O(\varepsilon^4), \quad (2.4.62)$$

$$\alpha = 1 + \frac{v_*^3}{v_*^2 - 2v_*^1} F \left(\frac{1}{aH} \right)^2 + O(\varepsilon^4), \quad (2.4.63)$$

$$v_r = -\frac{2}{3\omega+5} \cdot \frac{\omega v_*^2 + (1+\omega)v_*^3}{(1+\omega)(v_*^2 - 2v_*^1)} \partial_i Fa \left(\frac{1}{aH} \right)^3 + O(\varepsilon^5). \quad (2.4.64)$$

If we write, similarly to what is done in the second part of Section 2.4.1,

$$\Psi := e^{\frac{\zeta}{2}}, \quad (2.4.65)$$

we have the following expressions for p_a , p_b and F :

$$p_a = -\frac{2}{3} e^{-2\zeta} \left(\zeta'' + \zeta' \left(\frac{1}{r} - \zeta' \right) \right), \quad (2.4.66)$$

$$p_b = \frac{1}{3} e^{-2\zeta} \left(\zeta'' + \zeta' \left(\frac{1}{r} - \zeta' \right) \right), \quad (2.4.67)$$

$$F = -\frac{2}{3} e^{-2\zeta} \left(\zeta'' + \zeta' \left(\frac{2}{r} + \frac{\zeta'}{2} \right) \right). \quad (2.4.68)$$

Moreover, if we choose the Gaussian profile for ζ , i.e.

$$\zeta(r) = A \exp\left(-\frac{r^2}{2\Delta^2}\right), \quad (2.4.69)$$

these expressions become

$$p_a = \frac{4\zeta}{3\Delta^2} e^{-2\zeta} \left(1 - \frac{r^2}{2\Delta^2} (1 - \zeta)\right), \quad (2.4.70)$$

$$p_b = -\frac{2\zeta}{3\Delta^2} e^{-2\zeta} \left(1 - \frac{r^2}{2\Delta^2} (1 - \zeta)\right), \quad (2.4.71)$$

$$F = \frac{2\zeta}{\Delta^2} e^{-2\zeta} \left(1 - \frac{r^2}{3\Delta^2} \left(1 + \frac{\zeta}{2}\right)\right). \quad (2.4.72)$$

As a confirmation of the development, the particular case of the geodesic slicing with $f(\alpha) = 0$ gives a solution that is identical to the one developed in [Harada et al. 2015]. We thus have derived the long-wavelength solution in the Bona-Masso slicing. This solution will give realistic initial conditions for the spherical collapse if the length-scale of the inhomogeneity is greater than the Hubble radius.

2.4.3 The initial background

Concerning the homogeneous and isotropic background, only few parameters need to be specified. First, we need the initial scale factor a_i , that can always be rescaled to 1, and the initial Hubble factor $H_i := \frac{\dot{a}_i}{a_i}$ which tells "how fast" the universe is expanding at initial time. Then, we need to know what the repartition is between the several fluids that filled the background. These proportions are given by the cosmological parameters Ω_k^i which give the repartition of energy-density

$$\bar{e}_k^i = \Omega_k^i \bar{e}_c^i, \quad (2.4.73)$$

where $\bar{e}_c^i = \frac{3}{8\pi} H_i^2$ is the critical energy-density at initial time. The initial contributions to the pressure \bar{p}_k^i are given by the chosen equations of state.

2.5 Scales

We recall that all the quantities and equations we presented above and we use in the code are written in natural units in which $G = c = 1$. The time scale t_{scale} , in seconds, is fixed through the comparison of the experimental value of the Hubble factor measured today $H_0^{\text{exp}} \sim 70 \text{ km/s/Mpc}$ with an adjustable parameter H_0 in arbitrary units, chosen for numerical reasons :

$$t_{\text{scale}} = \frac{H_0}{H_0^{\text{exp}}}.$$

The length scale l_{scale} , in meters, and mass scale m_{scale} , in kilograms, are thus computed through

$$l_{\text{scale}} = ct_{\text{scale}}$$

$$m_{\text{scale}} = \frac{c^3}{G} t_{\text{scale}},$$

where the constants G and c are expressed in the international system of units SI.

2.6 Validation of the code

Before exploiting the code, we need to be sure it is stable enough to perform correct simulations. Sometimes, it can be done by comparing its results with a well known solution. For example, the dust case was compared to the Lemaitre-Tolman-Bondi (LTB) solution [Lemaitre 1933], [Tolman 1934], [Bondi 1947], in the works [Rekier et al. 2015] and [Rekier 2015] and successfully showed the validity of the initial code (without pressure). In our case, we have the difficulty that no analytic solution exists when we consider pressured fluids. A generalisation of the LTB solution for a fluid with pressure was presented in [Lasky and Lun 2006] but it necessitates equally a numerical treatment. And, as we work with the possibility to have two different fluids, actually few existing reference simulations of such non linear cosmological evolution exist in the literature for our code to be compared with. We thus only dispose of the second method to validate the code : the rescaling of the Hamiltonian constraint. It consists in the observation of the Hamiltonian constraint for several resolutions : if the code is stable, a refinement of the grid must induce a rescaling of the constraint and the factor of the rescaling depends on the order of the method. This was also used, for example, in [Rekier et al. 2015] and [Alcubierre and Mendez 2011].

To achieve this validation, we performed a simulation with two species of matter which have linear equations of state $p_1 = 0.1e_1$ and $p_2 = 0$. We chose the geodesic slicing and the initial data are fixed by the conformally flat method discussed in section 2.4.1. Note that we do not validate our code with the long-wavelength approximation as initial conditions since we need initial conditions perfectly correct (not an approximation) from the general relativity point of view. The initial profiles for the energy density contrasts $\delta_k = \frac{e_k}{\bar{e}_k} - 1$ are of the form of the smooth top-hat functions given by eq. (2.4.10). We fix the positive parameters of these profiles to $\delta_1^i = \delta_2^i = 1$, $r_1^i = r_2^i = 10$ and $\sigma_1 = \sigma_2 = 1$, while our spatial domain is the interval $[0, 500]$ (all in code units). We put as much quantity of matter 1 as of matter 2, which reads $\Omega_1^i = \Omega_2^i = 0.5$.

The last quantities that remain to be fixed are the initial scale factor a_i , the initial Hubble factor H_i and the Hubble factor measured today H_0 which will determine the time scale, the mass scale and the length scale. For our tests, we chose $a_i = 1$, $H_i = 0.03$ and $H_0 = 0.001$. The Courant-Friedrichs-Lewy factor (CFL) is set to 0.25, indicating that the discretization step in time Δt is linked to the spatial discretization Δr through the relation $\Delta t = 0.25\Delta r$. We tested the three resolutions $\Delta r = 0.1$, $\Delta r = 0.05$, and $\Delta r = 0.025$.

We now present the results of these simulations. The Hamiltonian constraint at $t = 25$ is shown on Fig. 2.1. The similarity in the shapes of the curves and the fact that it is rescaling with the resolution in the right order (curve for $\Delta r = 0.05$ has been multiplied by 4 and curve for $\Delta r = 0.025$ has been multiplied by 16) show the stability

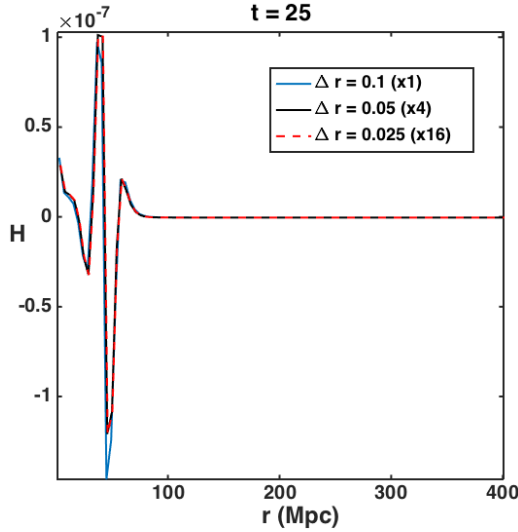


Figure 2.1 – Hamiltonian constraint at $t = 25$ for simulation of the evolution of a smooth inhomogeneity in the density profile, with three resolutions : $\Delta r = 0.1$, $\Delta r = 0.05$, and $\Delta r = 0.025$. Curve for $\Delta r = 0.05$ has been multiplied by 4 and curve for $\Delta r = 0.025$ has been multiplied by 16 to exhibit the second order of convergence of the method.

of the method and at least a second-order convergence of the scheme. Of course, the error is maximal at the centre of coordinates and at the boundary between the inner and outer parts of the over-density. Terms in inverse power laws of the radius are responsible for the larger error at the center. For the overdensity boundary, it is the location where the gradients are maximal and it justifies these peaks in the error.

Moreover, by inspecting the L^2 -norm of the Hamiltonian constraint with respect to time, in Fig. 2.2, we see that we also have a second order rescaling (as in the previous plot, curve for $\Delta r = 0.05$ has been multiplied by 4 and curve for $\Delta r = 0.025$ has been multiplied by 16). The convergence of the method is thus at least second order. Note that the late but steep increase at the end of the simulation is due to the collapse and possibly the reaching of a singularity. Indeed, we can see on Fig. 2.3 that the total energy-density contrast (defined by $\delta_{tot} = \frac{e_1 + e_2}{e_1 + e_2} - 1$, which is different from $\delta_1 + \delta_2$) seems to diverge. However, note that this is not a significant evidence that a black hole is formed. We will discuss this in the next chapter.

We thus have validated our integration code since the Hamiltonian constraint has the correct behaviour. We are allowed to trust our simulations and are ready to investigate in the following chapters the non linear cosmological spherical collapse with this tool.

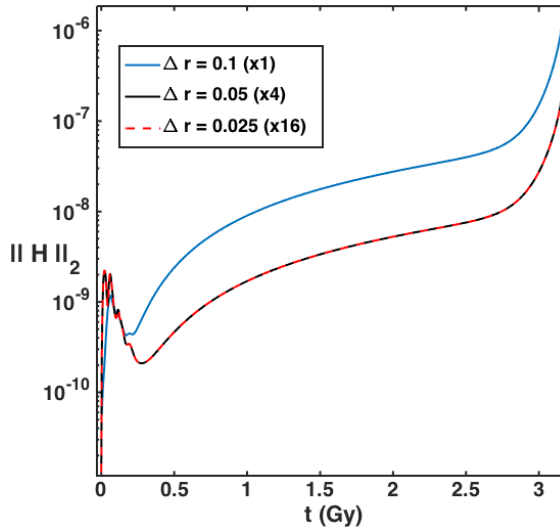


Figure 2.2 – Approximation of the L^2 -norm of the Hamiltonian constraint for simulation of the evolution of a smooth inhomogeneity in the density profile, with three resolutions : $\Delta r = 0.1$, $\Delta r = 0.05$, and $\Delta r = 0.025$. Curve for $\Delta r = 0.05$ has been multiplied by 4 and curve for $\Delta r = 0.025$ has been multiplied by 16 to exhibit the second order of convergence of the method.

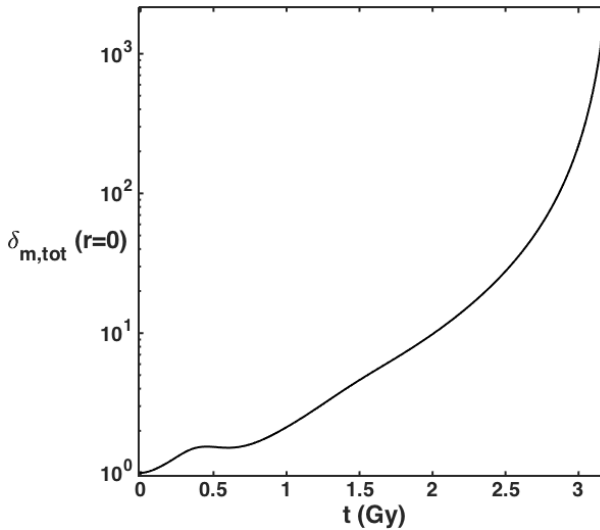


Figure 2.3 – Central total energy-density contrast versus time. The divergence indicates a collapse.

Chapter 3

The Search for Universality of the Spherical Collapse with Respect to the Matter Type

Summary

In this chapter, we study the spherical collapse of an over-density of a barotropic fluid with constant equation of state in a cosmological background. We first define the amplitude, size, mass and compactness notions we will use. Then, the code permits us to exhibit, for a fixed radial profile of the energy-density contrast, the existence of a critical value ω^* for the equation of state under which the fluctuation collapses to a black hole and above which it is diluting. A short phenomenological study, in the synchronous gauge, shows that considering only the central value for the energy-density contrast can lead to misinterpretations when dealing with pressured matter, showing the irrelevance of the top-hat approximation in this case.

The last section is devoted to the search for universality of the critical collapse with respect to the matter type by considering the constant equation of state ω as a control parameter. This means that we try to show that the mass of the formed black hole, for subcritical solutions, obeys a scaling law $M \propto |\omega - \omega^*|^\gamma$ with a critical exponent γ independent of the matter type. First attempts in a cosmological Friedmann background full of matter, in the synchronous gauge and harmonic slicing, give indications in favour of the universality. These simulations should however be treated with care since the collapse can not be followed until the black hole formation. Hopefully, additional tests in the super-horizon regime, using the long-wavelength approximation, showed the universal scaling law, attesting the universality in this case. Finally, in a universe asymptotically Minkowski and in a de Sitter background, the universality appears to be perfectly verified. These are the main results of this chapter.

3.1 Introduction

In 1992, Choptuik studied (see [Choptuik 1993]) the spherical gravitational collapse of a massless scalar field thanks to numerical relativity. He found that, in a Minkowski background, the mass of a formed black hole M follows a scaling power-law

$$M \propto (k - k_*)^\gamma, \quad (3.1.1)$$

where k is a one dimensional quantity parametrising the initial data (in particular, the energy-density profile), k_* is the threshold for black holes formation (which means that a black hole is formed when $k > k_*$ and not if $k < k_*$) and γ is the critical exponent which does not depend on k . Critical phenomena following such a scaling law are said "universal", in the sense that every near-critical solution obeys this scaling law. Moreover, the critical solution admits a continuous self-similarity (CSS). This is a symmetry for which dimensionless quantities h are scale invariant in the sense that $h(t, r) = h(at, ar)$ for spherical symmetry, where $a > 0$ is an arbitrary constant, and thus only depends on the ratio $\xi = \frac{t}{r}$. Such symmetry is linked to the renormalization group of the system (see [Harada 2002] for a detailed description of the CSS solution). This critical phenomenon is similar to critical phase transitions found in statistical mechanic by identifying M to an order parameter controlled by the function $|k - k_*|$ on the total phase space.

On this basis, numerous examples of universality in critical phenomena in gravitational collapse were discovered, some with a critical solution admitting a CSS and others with a discrete self-similarity (DSS) (the same symmetry for a only on the form $a = e^{n\Delta}$ for $n = 0, \pm 1, \pm 2, \dots$ and Δ a fixed constant). The interested reader can find more information in the review by Gundlach and Martín-García [Gundlach and Martín-García 2007]. Among others, it has been shown, still in a Minkowski background ([Evans and Coleman 1994], [Maison 1996]), that the universality was true in the case of the spherical collapse of a perfect fluid with barotropic equation of state $p = \omega e$, where p is the pressure, e is the energy density of the fluid and ω is a constant in the interval $[0, 1]$. The associated critical solution is sometimes called the "Evans-Coleman" CSS solution, according to the authors of [Evans and Coleman 1994]. It was unclear if such CSS solutions exist for $\omega > 0.89$ until [Neilsen and Choptuik 2000] showed it was the case for all ω between 0 and 1. These discoveries were of great importance because it means that, by fine tuning the initial conditions, it is possible to obtain a black hole with a mass as small as wished from a radiation fluid. The possible existence of tiny black holes would thus have an impact on the abundance of primordial black holes formed during the radiation era. In 1999, [Niemeyer and Jedamzik 1999] performed simulations that showed that universality holds also in the cosmological case, when considering a non empty background universe. However, [Hawke and Stewart 2002] showed in 2002, in a similar case, that some families of initial conditions admit a lower bound for the mass of a formed black hole : the scaling law (3.1.1) did not work for values of k very close to the critical solution but the mass seemed rather to stabilise towards 10^{-4} units of horizon mass. The authors explained that shocks, which are numerically challenging difficulties, are present when taking very small $|k - k_*|$ and this should be the reason why [Niemeyer and Jedamzik

1999] could not observe this phenomenon. However, [Musco and Miller 2013] and [Musco 2019] gave, as an explanation, that Hawke and Stewart used special initial conditions in the sub-horizon regime with remaining non growing modes and that this was the reason of the apparition of shocks. By using super-horizon fluctuations with exclusively growing modes, [Musco and Miller 2013] observed no breaking of the universality. All these works investigated the universality with respect to the initial conditions.

On our side, we try to answer the open question of the universality with respect to the matter type, not to initial conditions, in the case of a barotropic perfect fluid with constant equation of state $p = \omega e$. Indeed, at fixed initial data, varying the parameter ω will intuitively divide the solutions space into collapsing and non collapsing solutions, separated by a critical solution ω^* which should inevitably be the corresponding Evans-Coleman CSS solution mentioned above. The idea is thus to see if $|\omega - \omega^*|$ can be considered as a control parameter, as well as $|k - k_*|$ was in previous cases, and if a similar scaling law is verified. We will look for this relation in several important cases, different by their cosmological background : the homogeneous Friedmann universe full of matter, the empty Minkowski background and the empty de Sitter universe.

3.2 Quantities and observables

Before performing simulations, it is of great importance to specify the quantities we will derive in post-treatment to analyse the results. When evolving an inhomogeneity of spacetime, two basic quantities need to be followed : its amplitude and its size. However, such observables have not a unique definition. The simplest definition for the amplitude is the central density-contrast value $\delta_0(t) := \delta(t, r = 0)$. For the size of the fluctuation, it can be determined as the smallest radius r_0 where the density contrast is a predefined fraction q of the central one : $\delta(r_0) = q\delta_0$. These definitions can be motivated by their simplicity and by the behaviour of any centered overdensity of dust matter for which the shape is conserved all along the evolution because of the absence of pressure gradient. However, this is not necessarily the case when dealing with pressured fields. As we saw in section 2.4.2, the shape of a fluctuation is conserved at super-horizon scale, whatever the value of the equation of state. But in the non linear regime, this affirmation is no more true and the shape could be affected by the effect of the pressure. This is why a more robust characterization of the fluctuation must be used, which would depend less on its radial profile. To do so, we follow what is done in [Shibata and Sasaki 1999], [Harada et al. 2015] and [Musco 2019] and based our observables on a compaction function that will intuitively be interpreted as a compactness notion. Let us start the development with some useful quantities.

In spherical symmetry, it is convenient to work with the areal radius. This positive quantity $R(t, r)$ is defined through the relation

$$A := \int_0^{2\pi} \int_{-\frac{\pi}{2}}^{\frac{\pi}{2}} \sqrt{g_{\theta\theta}g_{\phi\phi}} d\theta d\phi = 4\pi R^2, \quad (3.2.1)$$

where $A(t, r)$ is the area of the surface defined by constant coordinates t and r . In our BSSN metric (1.4.1), the areal radius is simply the square root of its $\theta\theta$ component :

$$R = \sqrt{g_{\theta\theta}} = \psi^2 a \sqrt{\hat{b}r}. \quad (3.2.2)$$

This variable is important because local and background quantities must always be compared at the same areal radius. To give an example, assume we want to compare a quantity $Q(r)$ with its corresponding homogeneous background value $\bar{Q}(r)$ (it could be the mass contained in the sphere delimited by the radial coordinate r or any comparable integrated quantity). For the local BSSN metric, the areal radius is given by $R = \psi^2 a \sqrt{\hat{b}r}$. But for the Friedmann background universe, the areal radius is $R = ar$. This means that to compare Q and \bar{Q} in a pertinent way, at the same areal radius, we have to compare the quantity $Q(r)$ with $\bar{Q}(\psi^2 \sqrt{\hat{b}r})$ instead of $\bar{Q}(r)$.

A second notion that is unavoidable is the notion of mass. In general relativity, deriving a well-posed definition of mass is a difficult challenge since it should be gauge invariant and, if possible, time invariant. Moreover, several notions of mass exist in general relativity. For asymptotically Minkowski spacetimes, there still exists the possibility to compute the total energy on a single slice Σ_t . The ADM mass (see [Shibata 2016]) is based on this principle and gives a time independent quantity. Another mass notion that is often used in static spacetimes is the Komar mass (see [Gourgoulhon 2012]). But since we are working in an asymptotically Friedmann universe, we cannot use those definitions with no change. Indeed, the total mass is not finite and we need to truncate the computation to keep only the mass inside the fluctuation. To achieve that, we follow [Shibata and Sasaki 1999] and [Harada et al. 2015] and use the Kodama mass, which was first define in [Kodama 1980].

We start by considering the 2-metric

$$G_{AB} = \begin{pmatrix} g_{tt} & g_{tr} \\ g_{rt} & g_{rr} \end{pmatrix} \quad (3.2.3)$$

with $A, B \in \{t, r\}$. We can then define the Kodama vector by

$$K^A = \sigma^{AB} \partial_B R, \quad (3.2.4)$$

where R is the areal radius and $\sigma_{AB} = \sqrt{-G} \varepsilon_{AB}$ with ε_{AB} being the Levi-Civita symbol and $\sigma^{AB} = G^{AC} G^{BD} \sigma_{CD}$. As we are working in the zero shift gauge, this vector reads

$$K^t = -\frac{\partial_r R}{\alpha \psi^2 a \sqrt{\hat{a}}} \quad (3.2.5)$$

$$K^r = \frac{\partial_t R}{\alpha \psi^2 a \sqrt{\hat{a}}}. \quad (3.2.6)$$

The 2-vector K^A is now extended to a 4-vector K^μ by posing $K^\theta = K^\phi = 0$ because of the spherical symmetry. In [Kodama 1980] and [Harada et al. 2015], it is shown that the quantity $S^\mu = T^\mu_\nu K^\nu$ is a conserved current, meaning that its integral is a conserved

quantity. This integral is thus a good candidate for a mass notion. Therefore, the Kodama mass within a sphere of radius r at time t is naturally defined by

$$M_K(t, r) := 4\pi \int_0^r S^t \alpha(t, x) R^2(t, x) dx. \quad (3.2.7)$$

By developing S^t , we find

$$M_K(t, r) = 4\pi \int_0^r [T_t^t (-R^2 \partial_r R) + T_r^t (R^2 \partial_t R)] dx. \quad (3.2.8)$$

The expression (1.5.1) gives, in the case of a universe filled with one (or several) fluid(s) of matter,

$$T_t^t = -(e + p)W^2 + p = -E \quad (3.2.9)$$

$$T_r^t = (e + p) \frac{W^2}{\alpha} v_r = \frac{S_r}{\alpha}. \quad (3.2.10)$$

In terms of BSSN variables, we have

$$R^2 \partial_r R = \psi^6 a^3 r^2 \sqrt{\frac{\hat{b}}{\hat{a}}} \left(1 + 2r \frac{\partial_r \psi}{\psi} + \frac{r \partial_r \hat{b}}{2\hat{b}} \right) \quad (3.2.11)$$

$$\begin{aligned} R^2 \partial_t R &= \psi^6 a^3 r^3 \sqrt{\frac{\hat{b}}{\hat{a}}} \left(\frac{\dot{a}}{a} + 2 \frac{\partial_t \psi}{\psi} + \frac{\partial_t \hat{b}}{2\hat{b}} \right) \\ &= -\alpha \psi^6 a^3 r^3 \sqrt{\frac{\hat{b}}{\hat{a}}} \left(\frac{K}{3} + A_b \right), \end{aligned} \quad (3.2.12)$$

where we have use (1.4.7) and (1.4.8) for the last equality. In conclusion, the expression for the Kodama mass in BSSN variables is

$$\begin{aligned} M_K(t, r) &= 4\pi a^3 \int_0^r \psi^6 x^2 \sqrt{\frac{\hat{b}}{\hat{a}}} \left[E \left(1 + 2r \frac{\partial_r \psi}{\psi} + \frac{r \partial_r \hat{b}}{2\hat{b}} \right) \right. \\ &\quad \left. - x S_r \left(\frac{K}{3} + A_b \right) \right] dx. \end{aligned} \quad (3.2.13)$$

The corresponding quantity for the Friedmann universe used as background is thus

$$\overline{M}_K(t, r) = 4\pi a^3 \int_0^r \bar{e} x^2 dx = \frac{4}{3} \pi (ar)^3 \bar{e}. \quad (3.2.14)$$

Recall that to give a correct comparison between local and background quantities, we need to compute them at the same areal radius. The expression for the background Kodama mass is thus

$$\overline{M}_K(t, \psi^2 \sqrt{\hat{b}} r) = \frac{4}{3} \pi a^3 \psi^6 \bar{e} \sqrt{\frac{\hat{b}}{\hat{a}}} r^3$$

$$\begin{aligned}
&= 4\pi a^3 \bar{e} \int_0^{\psi^2 \sqrt{\hat{b}r}} x^2 dx \\
&= 4\pi a^3 \bar{e} \int_0^r \psi^6 y^2 \sqrt{\frac{\hat{b}}{\hat{a}}} \left(1 + 2y \frac{\partial_r \psi}{\psi} + \frac{y \partial_r \hat{b}}{2\hat{b}} \right) dy,
\end{aligned}$$

where we made the change of variable $x = \psi(t, y)^2 \sqrt{\hat{b}(t, y)} y$ for the last equality. The last expression, though less simple, can be useful because of its similarity with the first term of (3.2.13). For example, in a comoving gauge it gives the relation

$$\begin{aligned}
&M_K(t, r) - \overline{M}_K(t, \psi^2 \sqrt{\hat{b}r}) = \\
&4\pi a^3 \bar{e} \int_0^r \delta \psi^6 \sqrt{\frac{\hat{b}}{\hat{a}}} x^2 \left(1 + 2x \frac{\partial_r \psi}{\psi} + \frac{x \partial_r \hat{b}}{2\hat{b}} \right) dx, \tag{3.2.15}
\end{aligned}$$

only in term of the energy-density contrast. Concerning the comoving gauge, it is interesting to note that in the Misner-Sharp formalism, the Kodama mass coincides with the Misner mass (see [Musco 2019]). Note that this is also the case if the fluid is pressureless because the absence of pressure generates automatically a comoving gauge.

Now that we have defined our mass notion, we are ready to use it to define a compactness notion. Usually, the compactness of an object is a dimensionless quantity defined as its ratio mass to radius : $\frac{G}{c^2} \frac{M}{R}$. Similarly, we define the compaction function as the mass excess inside the sphere with areal radius R :

$$C(t, r) = \frac{2 \left(M_K(t, r) - \overline{M}_K(t, \psi^2 \sqrt{\hat{b}r}) \right)}{R}, \tag{3.2.16}$$

where the factor 2 is simply a question of convention to follow the definition of [Musco 2019]. This quantity is useful to define the size of the fluctuation. The radius $r_m(t)$ is defined, in hand, as the coordinate r where the compaction function reaches its maximal value. With this point, we can define the mass of the fluctuation as

$$M_m(t) := M_K(t, r_m(t)) \tag{3.2.17}$$

and its compactness as

$$C_m(t) := C(t, r_m(t)) = \max_{r>0} C(t, r). \tag{3.2.18}$$

The last quantity we need before using the code is the amplitude of the fluctuation. The standard way in cosmology is to take the central value of the energy density contrast. But in fact, there is no reason to consider only this particular value because this quantity is not necessarily representative of the full behaviour of the fluctuation, especially when pressure enters into consideration. Indeed, the energy-density contrast

radial profile changes when pressure increases. This is why we use an average energy density contrast defined by

$$\bar{\delta}(t, r) = \frac{\int_0^R 4\pi \delta R'^2 dR'}{\int_0^R 4\pi R'^2 dR'}. \quad (3.2.19)$$

By using BSSN equations, it gives

$$\delta_{\text{mean}}(t, r) = \frac{\int_0^r \delta \psi^6 a^3 \sqrt{\frac{\hat{b}}{a}} x^2 \left(1 + 2x \frac{\partial_r \psi}{\psi} + \frac{x \partial_r \hat{b}}{2\hat{b}}\right) dx}{\int_0^r \psi^6 a^3 \sqrt{\frac{\hat{b}}{a}} x^2 \left(1 + 2x \frac{\partial_r \psi}{\psi} + \frac{x \partial_r \hat{b}}{2\hat{b}}\right) dx}, \quad (3.2.20)$$

where the denominator can be replaced by $\frac{R^3}{3} = \frac{\psi^6 a^3 \sqrt{\frac{\hat{b}}{a}} r^3}{3}$. We thus see the direct relation between the mean energy-density contrast and the compaction in the comoving gauge by looking at the relation (3.2.15).

The mean energy-density contrast of the fluctuation, i.e. its amplitude, is defined as this quantity evaluated at the radius of the fluctuation :

$$\bar{\delta}_m(t) = \bar{\delta}(t, r_m(t)). \quad (3.2.21)$$

The pertinence of this definition can be pointed out through the following relations obtained in the long-wavelength approximation :

$$\bar{\delta}_m(t) \simeq 3\bar{\delta}(t, r_m(t)) \quad (3.2.22)$$

$$C_m(t) \simeq \bar{\delta}_m(t) (H(t)R(t, r_m(t)))^2, \quad (3.2.23)$$

where the first approximation has been derived in [Musco 2019] and the second in [Harada et al. 2015]. These relations show that the particular radius $r_m(t)$ contains an important part of the information characterizing the fluctuation whatever its shape. Actually, we show here that these relations are exact in the comoving gauge without the hypothesis of the long-wavelength approximation.

Starting from (3.2.15), the compaction function reads

$$C(t, r) = \frac{8\pi \bar{e} \int_0^R \delta R'^2 dR'}{R}. \quad (3.2.24)$$

This equation can easily transformed to

$$\begin{aligned} C(t, r) &= \frac{8\pi}{3} \bar{e} R^2 \frac{4\pi \int_0^R \delta R'^2 dR'}{\frac{4}{3} \pi R^3}, \\ &= (H(t)R(t, r))^2 \bar{\delta}(t, r), \end{aligned}$$

where we used (1.7.2). This last equation is also true in $r = r_m$ and gives the relation (3.2.23).

For the relation (3.2.22), we derive (3.2.24) with respect to R :

$$\frac{dC}{dR} = 8\pi e \frac{\delta R^3 - \int_0^R \delta R'^2 dR'}{R^2}.$$

Still using (1.7.2) and the expression of the average energy density in the comoving gauge, we obtain

$$\frac{dC}{dR} = H^2 R (3\delta - \bar{\delta}). \quad (3.2.25)$$

Thus, the only maximum is obtained at the location where $\bar{\delta} = 3\delta$, giving (3.2.22) exactly.

Now looking at the long-wavelength approximation in a general gauge, we have, following (2.4.17), that the relation (3.2.24) is correct up to second order. Thus, the developments we made are also correct up to that order, confirming the computations of [Harada et al. 2015] and [Musco 2019].

To conclude, the quantities we will focus on are the following ones:

- the central energy density contrast $\delta_0(t)$;
- the mean energy density contrast $\bar{\delta}_m(t)$;
- the compactness $C_m(t)$;
- the radius $r_m(t)$ and the corresponding areal radius $R_m(t)$;
- the mass $M_m(t)$;
- the central value of the lapse $\alpha_0(t)$ when a non geodesic slicing is used.

3.3 Phenomenology by varying the equation of state

We now start using the code and look for the typical behaviours that can occur when evolving a small over-density in a universe filled with a single fluid. We also look at the influence of the constant equation of state parameter ω . In all this chapter, we fix the following parameters (unless otherwise stated) : $H_i = 0.03$, $a_i = 1$ and $H_0 = 0.001$. Additionally, we use the geodesic slicing because the synchronous gauge is easily interpretable. But we must keep in mind that this choice of coordinates will not permit us to follow the collapse of an inhomogeneity until the formation of a black hole. To achieve that, we will use another slicing condition in the next section.

We perform simulations involving a single barotropic fluid of matter $p = \omega e$ with an initial profile described by the equation (2.4.10), which is, as already mentioned, parametrized by three real numbers: the initial amplitude δ_i , the initial size r_i of the fluctuation and the sharpness of the profile σ . This profile and the corresponding initial compaction function are shown in Fig. 3.1. A compaction function has usually this bell shape: starting from zero, growing to a peak and then decreasing to zero as asymptotic behaviour. The peak determines, as defined in section 3.2, the size of

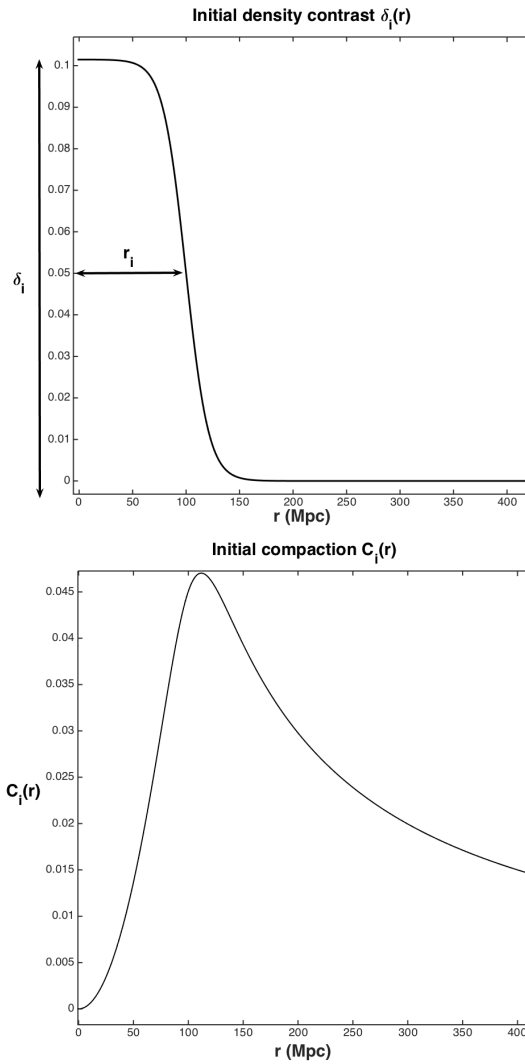


Figure 3.1 – The upper graph shows the shape of an initial profile of the energy-density contrast. The second one gives the corresponding compaction function. The peak in the latter is in agreement with the size of the fluctuation seen in the above panel.

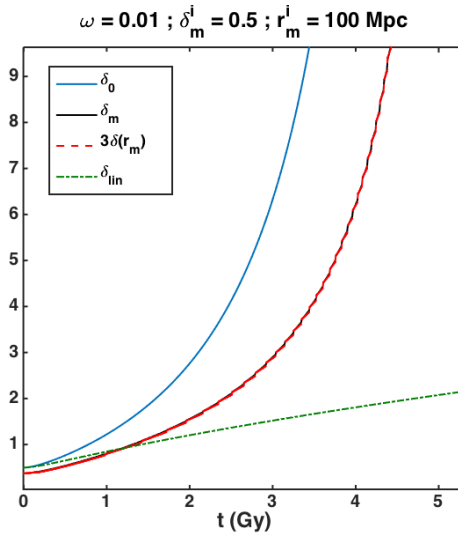


Figure 3.2 – Evolution of the central energy-density contrast δ_0 , the mean energy-density contrast $\bar{\delta}_m$ and the central energy-density contrast δ_{lin} computed with the linear perturbation theory in the collapse scenario. The last curve, $3\delta(r_m)$, shows the validity of the formula (3.2.22), although we are not in a super-horizon regime. The full relativist δ_0 and the approximate δ_{lin} are in adequation at early times, which is an additional validation of the code.

the fluctuation. We can see that it is nearly the same value as r_i , which confirms the pertinence of this definition.

Depending on the three initial parameters, δ_i , r_i and ω (σ is fixed to 10Mpc in all what follows), we observe two different behaviours. The first one is the collapse while the second one is dilution.

We show such an example of collapsing solution in Fig. 3.2, 3.3, 3.4 and 3.5 with the values $\omega = 0.01$, $\delta_i = 0.5$ and $r_i = 100\text{Mpc}$. We see on Fig. 3.2 that the central and mean energy-density contrast are both diverging on the first plot. We also see that the relation (3.2.22) seems to be correct with good accuracy since the curves of $\bar{\delta}_m$ and $3\delta(r_m)$ are nearly the same, although the conditions for the long-wavelength approximation are not verified in this situation. The last curve represents δ_{lin} , the central energy-density contrast computed with the linear perturbation theory described in Section 1.8. The agreement between this curve and $\delta_0 := \delta(r = 0)$ at early times is an additional indication of the validity of the code.

Concerning the compactness (Fig. 3.3), it is first decreasing because of the background expansion. But then it grows until the end of the simulation, indicating a collapse. Our code is not able to follow it at higher compactnesses, but this is sufficient for our purpose. Note that the relation (3.2.23) is verified all along the collapse, even if we are not in a subhorizon regime. The reason why this relation and (3.2.22) are verified must probably due to the low value of the equation of state. Recall that these relations are perfectly verified in the comoving gauge. And the absence of pres-

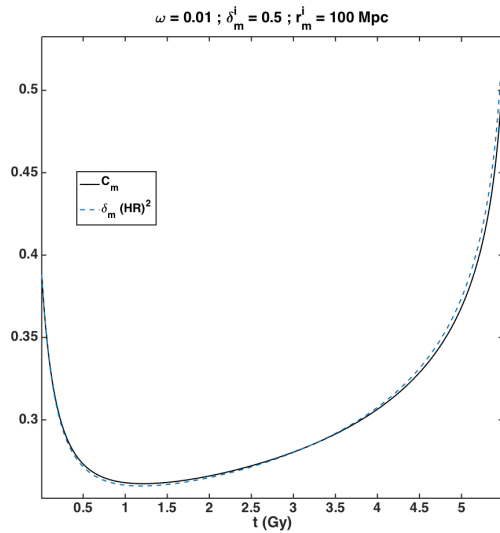


Figure 3.3 – Evolution of the compactness of the fluctuation. The second curve represents the quantity $\bar{\delta}_m(HR)^2$ and its adequation with C_m confirms the approximation (3.2.23), although we are not in a super-horizon regime. The compactness decreases first with the background expansion but then increases more and more rapidly with the collapse. The code is not able to follow it until the black hole formation at $C_m = 1$.

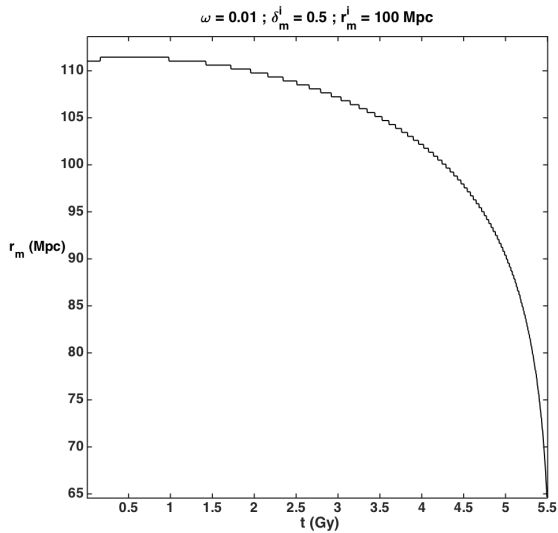


Figure 3.4 – Evolution of the radius of the fluctuation. The steps come from the spatial discretisation. The radius first increases with the background but then starts decreasing, indicating a concentration of the matter towards the center of the grid.

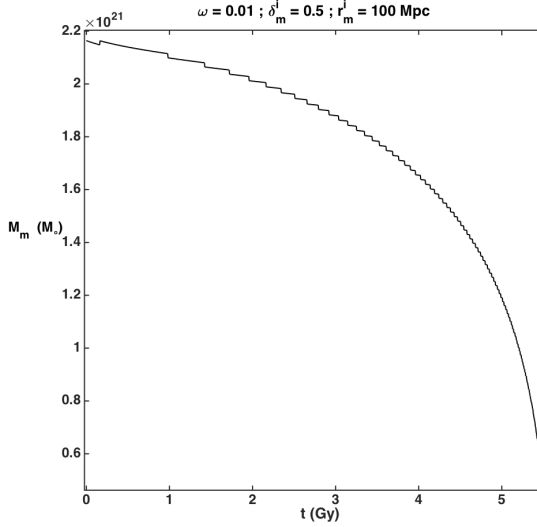


Figure 3.5 – Evolution of the mass of the fluctuation, in solar mass units. The mass decreases because the integration upper bound is related to the radius of the fluctuation, which is collapsing to zero.

sure precisely generates a comoving gauge. Thus the low pressure explains why these relations seem to hold in this case. The Fig. 3.4 shows that the radius of the fluctuation has an increasing phase, coherently with the decreasing phase of the compactness, followed by a fast decreasing. The matter is concentrating towards the center of the grid, which is intuitively logical in the collapse scenario. The Fig. 3.5 shows a decreasing mass. Although this can seem to be illogical, this is normal because the mass we used is an integral whose upper bound is r_m , which is decreasing. The steps visible in these two graphs are simply due to the spatial discretization of the grid. Indeed, the radius r_m , i.e. the location of the maximal compaction, can only be taken among the spatial values given by the discretization, explaining the discontinuous bumps revealing a change in this value.

We give now an example of diluting solution in Fig. 3.6, 3.7 and 3.8 with the values $\omega = 0.1$, $\delta_i = 0.1$ and $r_i = 100\text{Mpc}$. First notice that the two correspondences (3.2.22) and (3.2.23) are no more exactly verified because we involved more pressure and the long-wavelength approximation does not hold. Then, on the first plot, the central energy-density contrast has an oscillations phase before decreasing to zero in a power law of a . This is in agreement with the linear perturbation theory which exhibits the same behaviour. The similarity of the two curves was expected because the evolution stays in the linear regime and this is an additional validation of the code. The mean energy-density is also decreasing but without oscillations. Fig. 3.7 and 3.8 show, through clear power laws in a , that the fluctuation is at late time completely diluted in the background and only follows the dynamics of the latter. The background expansion and the internal pressure are too strong for the fluctuation to collapse and

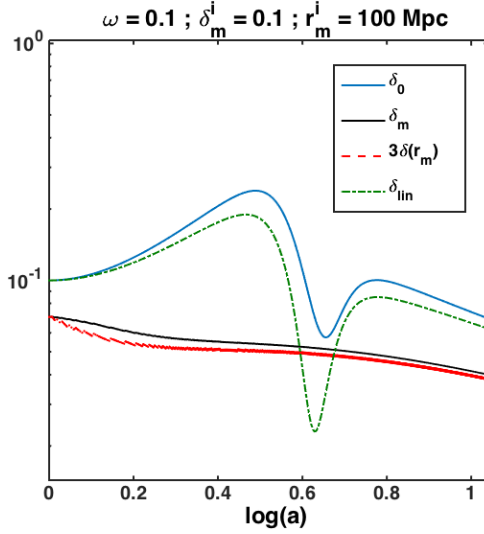


Figure 3.6 – Evolution of the central energy-density contrast δ_0 , the mean energy-density contrast $\bar{\delta}_m$ and the central energy-density contrast $\tilde{\delta}_{lin}$ computed with the linear perturbation theory in the dilution scenario. The last curve, $3\delta(r_m)$, shows the inaccuracy of the formula (3.2.22) in this case. The full relativist δ_0 and the approximate $\tilde{\delta}_{lin}$ are in adequation all along the simulation.

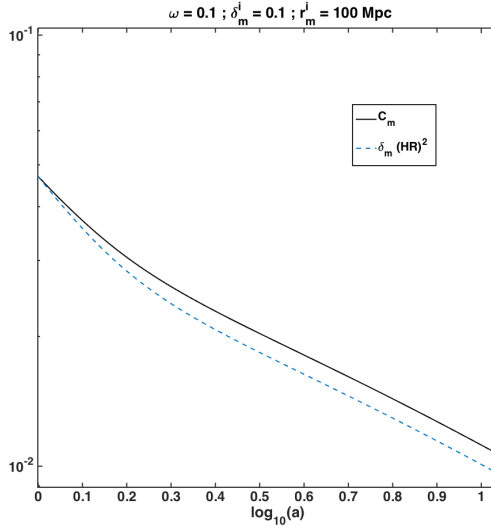


Figure 3.7 – Evolution of the compactness of the fluctuation. The second curve represents the quantity $\bar{\delta}_m(HR)^2$ and is no more in adequation with C_m . The compactness decreases in a powerlaw of the background scale factor, which means that the fluctuation follows its expansion.

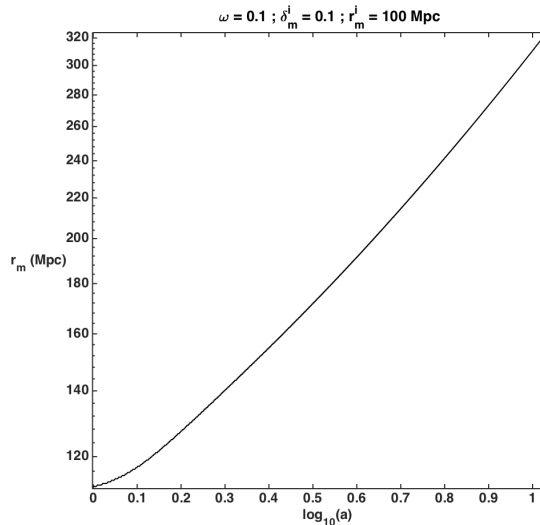


Figure 3.8 – Evolution of the radius of the fluctuation. It is increasing in a powerlaw of the background scale factor, indicating that the fluctuation follows the cosmological expansion.

make it disappear.

We study now the dependence on the equation of state ω by varying it from 0 to 0.9.

Resulting simulations with parameters $\delta_i = 0.5$ and $r_i = 100\text{Mpc}$ give the Fig. 3.9 to 3.13. On these plots, each curve corresponds to one particular value of ω and this value determines the color of the curve, respectively to the right color scale. On the Fig. 3.9, representing the central energy-density contrast, we see that, unsurprisingly, there exists a critical value ω^* of the equation of state that separates collapsing solutions, for which $\omega < \omega^*$, and diluting solutions, for which $\omega > \omega^*$. This value is uneasy to determine in these simulations because it is not clear if curves around $\omega = 0.05$ will asymptotically decrease to zero or continue to grow. To determine it precisely, an AMR scheme should be use with another slicing. However, we will compute and use its approximate value in the next section, jointly with a better slicing. A second interesting fact visible in this plot is the existence of a value for ω , around 0.4, above which the pressure is so strong that δ_c becomes negative after an overshoot and regrows asymptotically towards zero. In this case, the pressure has locally created a void from an over-density. But Fig. 3.10, representing the mean energy-density contrast $\bar{\delta}_m$, shows curves that are strictly positive. This means that the voids indicated in the first graph are surrounded by over-dense shells such that the average density contrast is still positive. The central behaviour is thus not always reflecting the global evolution of the fluctuation. This is one of the reasons of the weakness of the top hat approximation when dealing with pressure.

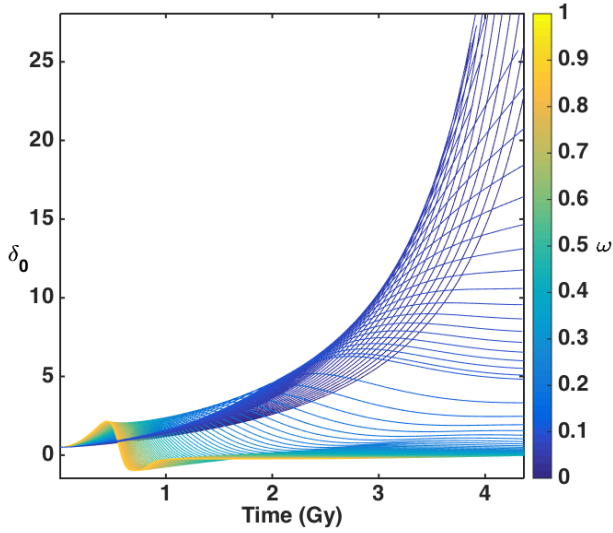


Figure 3.9 – Evolution of the central energy-density contrast for several values of the equation of state ω . A critical value of ω , near 0.05, separates collapsing and diluting solutions. Another specific value, near 0.4, separates solutions that stay positive from solutions that become negative, both converging to zero.

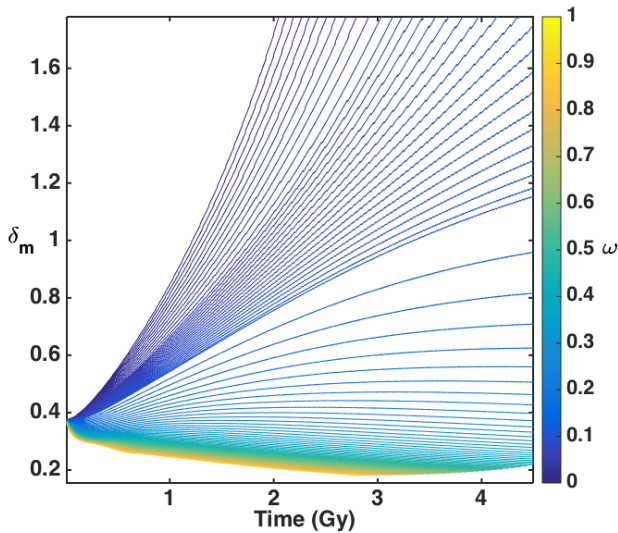


Figure 3.10 – Evolution of the mean energy-density contrast for several values of the equation of state ω . The difference with the central value δ_0 is that, here, curves are all strictly positive, even for large values of ω .

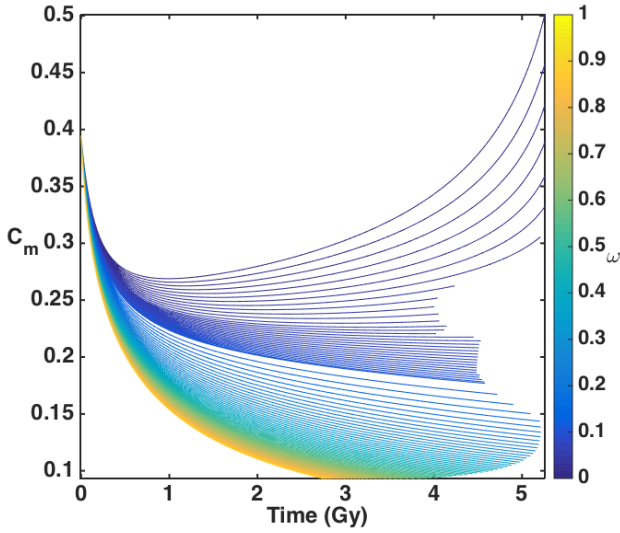


Figure 3.11 – Evolution of the compactness for several values of the equation of state ω . By comparison with the energy-density contrasts (central and mean), no oscillating phase occurs for this variable. The coordinate singularity prevents the code to evolve longer and to reach higher values of the compactness.

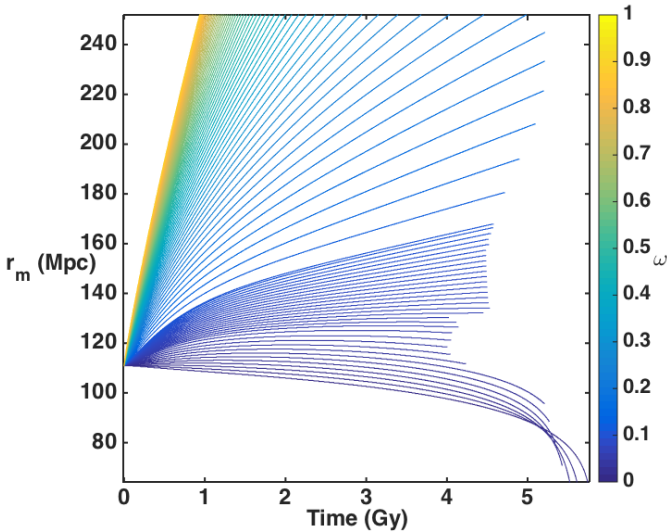


Figure 3.12 – Evolution of the radius for several values of the equation of state ω . Contracting curves correspond to collapsing solutions. A small change of regime is visible at very low ω (at lower right corner of the window) where the speed of the contraction first increases with ω and then decreases.

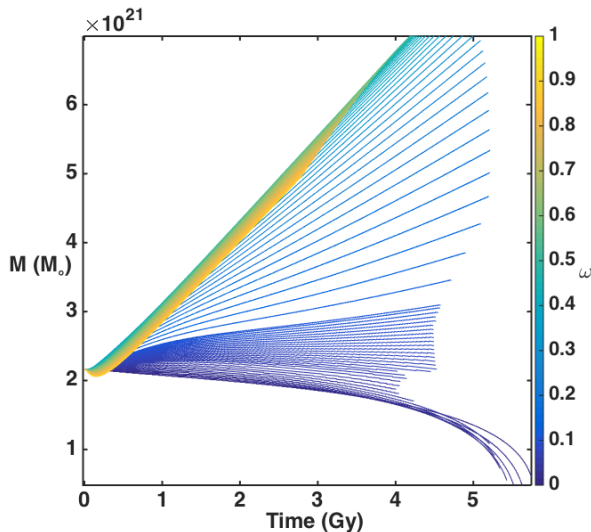


Figure 3.13 – Evolution of the mass for several values of the equation of state ω . Decreasing curves correspond to collapsing solutions because the outer integration bound decreases with time. The same change of regime as in the radius is present. A second one, not visible in the evolution of the radius, occurs at a higher value of ω (near 0.4) where the mass starts to decrease with ω . From this value, the mass initially decreases before growing.

The compactness, plotted in Fig. 3.11, has no inflexion point regardless of the value of ω . This regular behaviour makes us choose the critical value ω^* as the one which separates late growing C_m from those which are numerically always decreasing. This is an empirical value that is necessarily inaccurate, because some decreasing curves near the critical solution (stopped by the coordinate singularity and its unstable behaviour) might eventually regrow again at later time, but it remains close to the real one.

Concerning the size of the fluctuation, the radii are represented in Fig. 3.12. Diluting solutions are those for which the radius is finally expanding and collapsing solutions are the ones for which the radius is contracting. We see a small change in the regime for collapsing solutions. Increasing ω from zero makes the radius contract faster. But, after a particular (very small) value of the equation of state, increasing ω makes it contracting slower again. This value corresponds in fact to the limits between negative and positive initial slopes of $r_m(t)$. This phenomenon is even more visible on the evolution of the mass M_m in Fig. 3.13. On this last figure, we observe a second change of regime at large ω , which is visible only on this quantity. Before a value near 0.4, larger values of ω give larger masses (due to the integral bound in the definition of the mass). But above this limit, larger values of ω give smaller masses. This change is also illustrated in the fact that for ω just smaller than this value, the mass is initially growing, but for ω larger than it, the mass is initially decreasing before regrowing.

3.4 Towards universality

We now want to see if the spherical collapse is universal with respect to matter species. For this reason, we must check if the universality relation (3.1.1) is verified if we take as parameter k the equation of state ω (although this parameter does not represent exactly what is called strictly speaking the initial conditions), that is to say :

$$M \propto |\omega - \omega^*|^\gamma \quad (3.4.1)$$

with γ a constant independent of ω . In this way, we want to check if the parameter ω can be considered as a control parameter while the mass M is seen as an order parameter, similarly to what is done in transition phase theory. Intuitively, the critical solution ω^* must corresponds to the classical critical solution found by [Evans and Coleman 1994] and [Maison 1996] when the equation of state is fixed to that value. It is then known that this solution admits a CSS (continuous self-similarity). We already know that the mass of the black holes formed near this solution decreases (in the famous power-scaling law) to arbitrarily small values. It is thus reasonable to consider that this mass will also be as small as required by approaching ω^* . We are just not sure it will converge in power of $|\omega - \omega^*|^\gamma$ as a universal phenomenon would do.

Concerning the cosmological case, the first in which we are interested, we know that [Hawke and Stewart 2002] exhibited a lower bound in the mass, indicating a breaking of the universality. We recall that [Musco and Miller 2013] observed however no such bound and saw no breaking of universality. The explanation was that the results of Hawke and Stewart must be due to special initial conditions. We do not know, a priori, whether or not we will reach a lower bound in our case, like Hawke and Stewart. The most probable is that our code will not be able to reach values of ω sufficiently close to ω^* to observe this phenomenon, and maybe even not close enough to observe the universality scaling-law. We already mentioned in the previous sections that our gauge choice does not permit us to compute neither the exact value of the mass M of the object that is formed, nor the critical ω^* . The coordinate singularity (collapse of the conformal factor ψ) that is generated by the synchronous gauge makes the simulations break down before the object is formed. However, we can approximate these quantities and consider the results as indications in favour of or against universality. And then we will try to prove it with another gauge.

This is why we decide to consider, when it is not possible to follow the evolution until the black hole formation, the mass of the object at the time where its radius has decreased by a factor q compared to the difference between the maximal radius it has reached in the evolution and the initial radius. That is to say that we choose to consider the mass at the first time t where

$$r_{\max} - r_m(t) \geq q(r_{\max} - r_m^i). \quad (3.4.2)$$

Taking a large value for q will increase the precision of the masses considered, by comparison with the exact ones, but it will also increase the minimum value in ω for which we are able to compute such quantity. Indeed, if q is too large, simulations for values near ω^* are stopped before the condition (3.4.2) is fulfilled and the mass cannot

be computed. On the contrary, taking a small value for q will allow us to explore values nearer ω^* but the resulting masses considered will be further from the real ones. This construction is quite artificial but we must say that, whatever the code, the mass is always computed thanks to an artificial criteria. This criteria is generally an indication that a black hole has formed, such as the collapse of the lapse, a compactness equal to one or a numerically detected horizon. Since none of these conditions can be reached, we fix the computation of the mass before the black hole formation, at a fictive time where all compared simulations have decreased with the same factor q . Our criteria is based on the collapse of the size of the fluctuation and appears to work satisfyingly, though not perfectly.

For the critical ω^* , we choose to fix it at the value where the late growth rate of the compactness goes from positive to negative.

3.4.1 Tests with conformally flat initial conditions

We first consider the case of conformally flat initial conditions given by the density profile (2.4.10).

3.4.1.1 Growth/decrease rates

We recall that the growth rate of a quantity $f(t)$ is defined as the function

$$Df = \frac{\partial \log f}{\partial \log a} \quad (3.4.3)$$

where a is the cosmological scale factor. The growth rates of the central energy-density, the mean energy-density and the compactness, $D|\delta_0|$, $D\delta_m$ and DC_m (resp.), are quantities that are interesting to compute because of the late time power-laws seen in Fig. 3.6 and 3.7 in the diluting scenario. We illustrate these values in Fig. 3.14, 3.15 and 3.16 for the same simulations as in section 3.3 (green points) and also by taking the initial δ_m^i equal to 0.1 (black points).

As it could be expected, the behaviour in terms of central energy-density contrast δ_0 is far less regular than those in terms of mean energy-density contrast and compactness. The asymptote visible near $\omega = 0.4$ in Fig. 3.14 is only due to the fact that, above this value, the central energy-density contrast becomes negative at late time. This forces us to take its absolute value to compute its growth rate and makes the asymptote appear. We already noticed this transition phase in the previous section. Note that this critical value seems to be the same for both initial conditions, as if this limit was universal. On the contrary, the crossing of the curves near $\omega = 0.15$ is not understood because the two other plots on Fig. 3.15 and 3.16 show both two non crossing curves that seems to be just translations of each other. This must be due either to the numerical instabilities present at the center of the grid or to another unknown change of regime not visible on the other graphs. However, the irregular aspects of this figure is an indication that taking only the central value into account will necessarily induce errors in the analysis of the global behaviour.

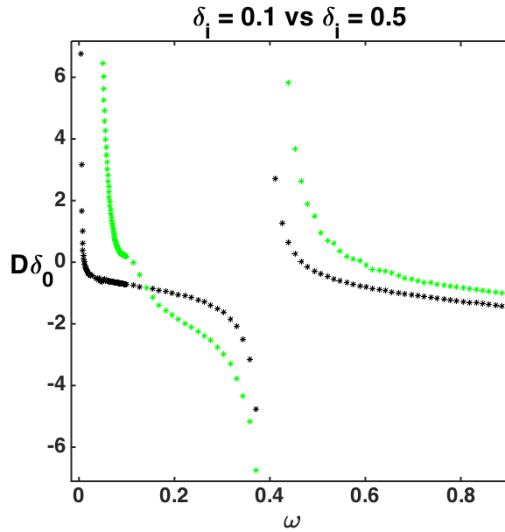


Figure 3.14 – Late growth rate of the central energy-density contrast δ_0 as a function of the equation of state ω . The asymptote is due to the positive to negative transition of δ_0 that imposes to take its absolute value before considering its logarithm. This transition value seems not to depend on the initial amplitude. Green dots have initial amplitude $\delta_i = 0.5$ while black ones have $\delta_i = 0.1$.

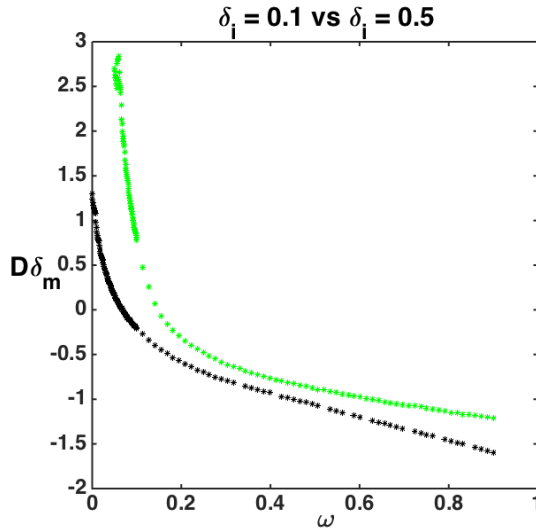


Figure 3.15 – Late growth rate of the mean energy-density contrast $\bar{\delta}_m$ as a function of the equation of state ω . Its behaviour is much more regular than that of δ_c . Green dots have initial amplitude $\delta_i = 0.5$ while black ones have $\delta_i = 0.1$.

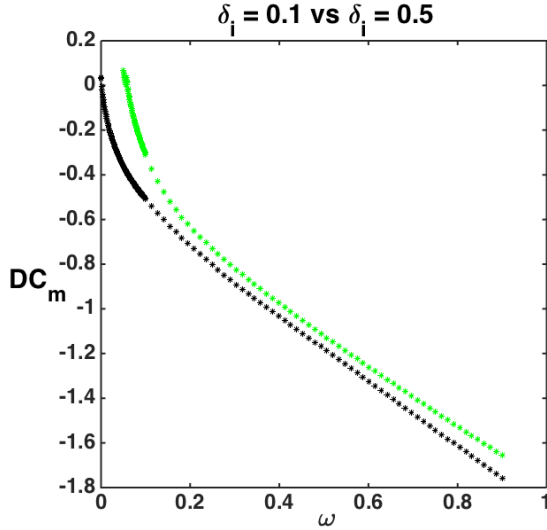


Figure 3.16 – Late growth rate of the compactness C_m as a function of the equation of state ω . The slope of its linear behaviour at large ω seems not to depend on the initial amplitude. Green dots have initial amplitude $\delta_i = 0.5$ while black ones have $\delta_i = 0.1$.

The two other plots in Fig. 3.15 and 3.16 show a quasi linear relation at large ω , especially for the compactness, with similar slopes when making the initial amplitude vary. These similar and regular slopes for large ω must be due to the background evolution that seems to dominate the local one.

Recall that negative values indicate a non collapsing solution, or at least the simulations that have already begin to dilute before the code stopped. Thus, we can see that the two plots give two different values for the critical ω^* , those computed with DC_m being smaller than those computed with $D\bar{\delta}_m$. We choose arbitrarily to take as a critical value ω^* the one computed with DC_m . This is not perfect but the error is at least bounded by the difference of the two values, which remains sufficiently small for our purpose. Empirical values of ω^* obtained are 0.058 for $\delta_i = 0.5$ and 0.0015 for $\delta_i = 0.1$.

3.4.1.2 The search for the scaling law with the geodesic and harmonic slicings

Now go back to the universality of the collapse and the relation (3.4.1). We compute the mass M with two different values of q in the condition (3.4.2) : $q = 0.1$ and $q = 0.9$. We do so for the initial amplitude $\delta_i = 0.5$. Results are shown in Fig. 3.17. As explained in the beginning of the section, a smaller value of q will include in the figure simulations with ω closer to ω^* . This is why in the first graph we have points for values of $|\omega - \omega^*|$ smaller than 0.01 while in the second graph it does not go under 0.02. But a smaller value of q induces a less precise value of M . This explains the difference between first and second values of the masses (upper ones are

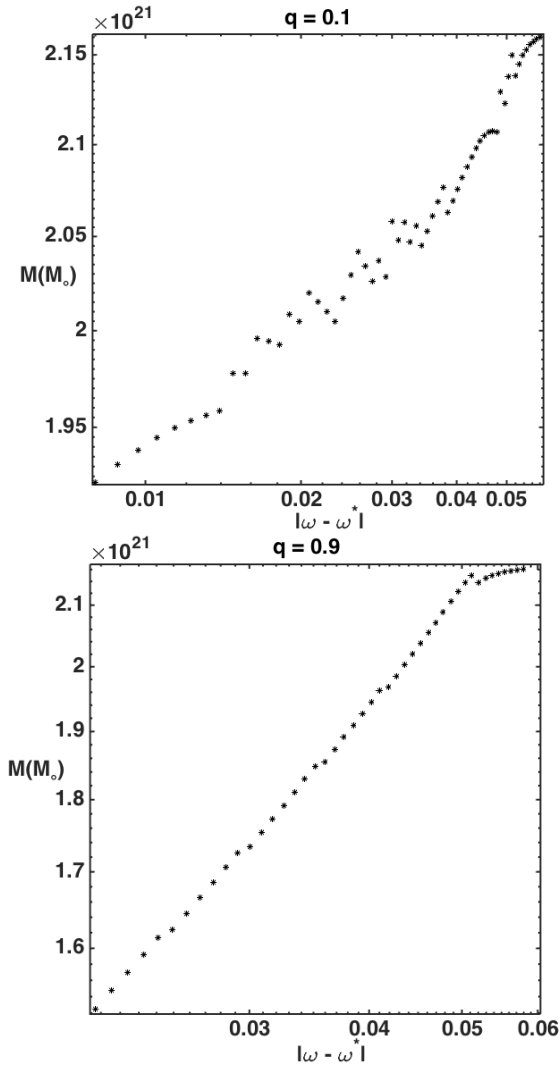


Figure 3.17 – Mass of the fluctuation computed at the time of the condition (3.4.2) with $q = 0.1$ for the upper plot and $q = 0.9$ for the lower one. First graph allows values of $|\omega - \omega^*|$ lower than 0.01 while second one does not go under 0.02. But latter masses are more precise and the shape is much more regular, showing a power law which is an indication that the collapse is universal with respect to ω .

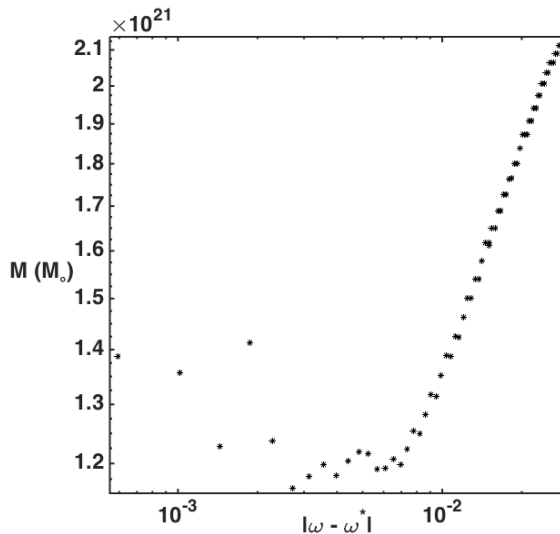


Figure 3.18 – Mass of the fluctuation computed at the time of the condition (3.4.2) with $q = 10$ by using the harmonic slicing. The power law for values at the right of the plot confirms the results of Fig. 3.17. However, closer points to ω^* reveal either numerical instabilities or a lower bound in the mass, suggesting, similarly to [Hawke and Stewart 2002], that universality fails for values very close to the critical solution.

larger because integration has been stopped earlier) but also the fact that the bottom graph has a more regular shape. However, in both we observe globally a power law, especially in the second graph. We are thus allowed to think that the mass obeys the power law (3.4.1) in this case. This gives a numerical indication in favour of the universality of the collapse with respect to the equation of state ω .

However, this result must be confirmed with another gauge choice to be sure it is not just a gauge effect. Additionally, the previous simulations remains quite far from the threshold, maybe not sufficiently close to it to prove the universality relation. A more stable gauge will permit us to compute more precise values of the mass and the threshold ω^* , to explore values closer to the critical solution and maybe to observe the universality breaking mentioned in [Hawke and Stewart 2002]. To do it, we take the harmonic slicing instead of the geodesic one. The harmonic slicing is a Bona-Masso slicing, such as described in section 2.1, with the function f of eq. (2.3.9) defined by $f(\alpha) = 1$. First, note that the critical value computed with the harmonic slicing is equal to the one computed with the geodesic with a difference less than 10^{-4} , which is another validation of the result. Secondly, still by using the criterion (3.4.2) for the determination of the mass, we are able to fix the parameter q to much more higher values than in the synchronous gauge thanks to the stability of this gauge. But, unfortunately, we are still not able to follow the collapse until the black hole formation. By taking $q = 10$, we obtain the Fig. 3.18, which is in a complete agreement with Fig. 3.17. We observe that the power law is no more verified once $|\omega - \omega^*|$ is going under 10^{-2} . This erratic behaviour at the very left of the graph must be due to the extreme

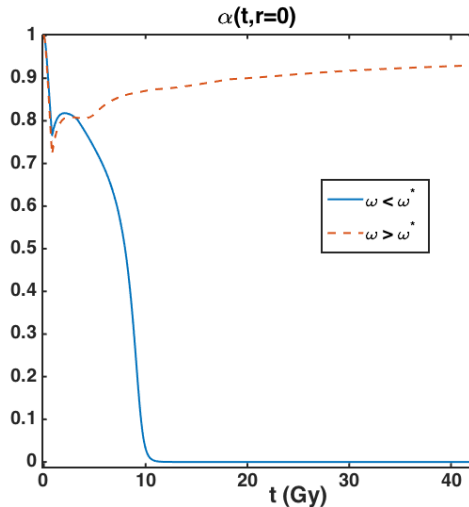


Figure 3.19 – Central value of the lapse in a sub and a super-critical solution. The sub-critical solution leads to the formation of a black hole as the collapse of the lapse indicates it. The super-critical solution shows a lapse regrowing indicating a dilution.

instability and, possibly, the violence of the evolution for parameters in this region. Universality thus could fail very close to the critical solution, unless we are still not sufficiently close to the critical solution to observe universality.

3.4.1.3 The search for the scaling law with the $1 + \log$ slicing

We finally test a last slicing condition, the $1 + \log$ slicing presented in section 2.3.2, to try to follow the collapse until the formation of a black hole. With this slicing, we give here an example of a sub and a super-critical solution obtained in that gauge.

The central value of the lapse is shown in Fig. 3.19. The sub-critical solution is a collapsing solution and we can see the formation of a black hole since the lapse is collapsing to zero. This freezing of time at the centre permits the code to avoid the central singularity and to pursue the calculation outside the horizon after its formation. On the contrary, the other solution exhibits a lapse regrowing away from zero, indicating that the overdensity is diluting. At early times, both solutions follow nearly the same curve before choosing between a collapsing or a diluting solution. This is typically what occurs in critical phenomena : near-critical solution all follow the critical (self-similar) solution until falling into a black hole solution or a diluting one. The time before leaving this curve depends on the closeness to the critical parameter ω^* .

The compactnesses are presented in Fig. 3.20. The collapsing solution shows a compactness growing higher than unity, the black hole limit. But the final compactness of the object seems to stabilise to a value near 1.3. On the other hand, in the diluting solution, the compactness decreases to zero, indicating that the over-density

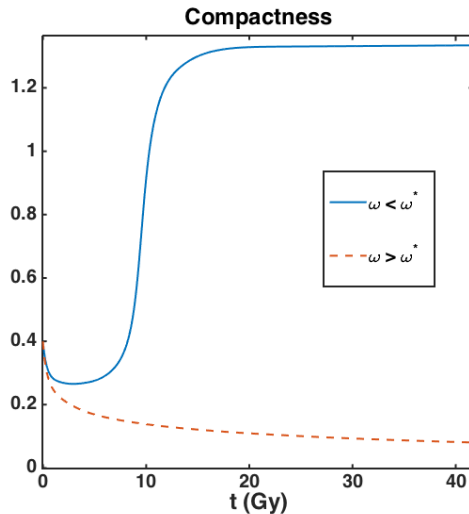


Figure 3.20 – Evolution of the compactness in a sub and a super-critical solution. The compactness reaches values greater than unity for the sub-critical solution, revealing the formation of a black hole. Its final compactness seems to be around 1.3. The diluting super-critical solution shows a decreasing compactness.

is progressively disappearing.

Concerning the mass, we see in Fig. 3.21 that it is decreasing until the formation of the black hole. Then, once it has formed, the black hole grows and accretes matter to finally stabilize due to the collapse of the lapse that freezes the time. The diluting solution shows a late-time evolution following the cosmological expansion and thus a late-time growing mass because of the growing of r_m .

The shape of the areal radius, in Fig. 3.22, equally shows that the size of the black hole regrows once it has formed, due to the matter accretion, and then stabilizes. In the diluting solution, it is always growing, following the background expansion.

With all these information, the question is thus "Which value for the mass of the formed black hole should we take?". We know that, in a FLRW universe, the mass of a black hole is not constant in time (see [Faraoni and Jacques 2007], [McVittie 1933] or [Faraoni 2018] for a review). Indeed, it is growing with the cosmological scale factor $a(t)$, as seen in our simulations. A reasonable choice is to take the value of the mass when the compactness is equal to one, which corresponds almost to the minimum in the curves of the mass and of the areal radius. Another choice would have been the value to which it is stabilizing. But we prefer the first solution for two reasons. First, the late stabilization is due to the freezing of time and may thus be a coordinate effect. The local minimum value seems to be a more pertinent choice. Second, for very near critical solutions, the code has difficulties to follow the collapse until the stabilization.

The mass values computed in this way are reported on Fig. 3.23. Unfortunately, the results do not confirm at all the previous computations : no scaling law is visible

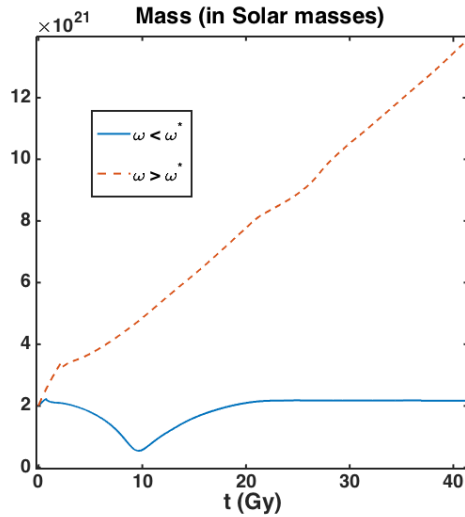


Figure 3.21 – Evolution of the mass in a sub and a super-critical solution. In the collapsing solution, the mass is decreasing until the black hole formation. After that, it regrows, showing that the formed black hole attracts matter. Finally, it stabilizes due to the freezing of the time. The other solution shows equally a growing mass because of the radius of the fluctuation grows with the background expansion.

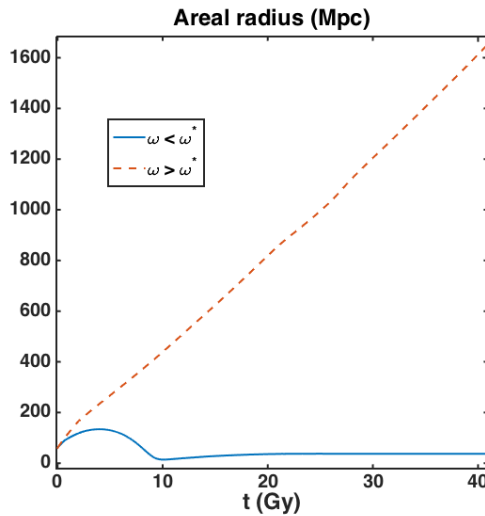


Figure 3.22 – Evolution of the areal radius in a sub and a super-critical solution. The collapsing solution shows a size that is decreasing until the formation of a black hole and after that is regrowing and then stabilizing.

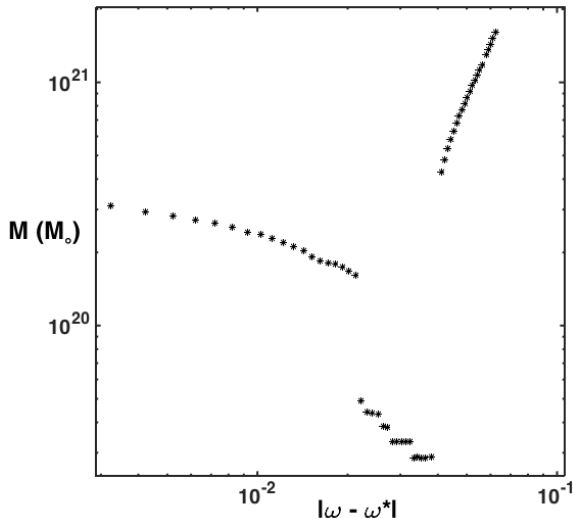


Figure 3.23 – Mass of the formed black hole computed with the $1 + \log$ slicing. No scaling law is observed, indicating that values closer to ω^* should be computed to look for universality.

and, worse, no decreasing of the mass is seen when considering the most left points in the graph. We are thus in a similar case to what is described in [Hawke and Stewart 2002]. In [Musco et al. 2009], it is explained that this behaviour appears because taking non linear initial profiles (with too large initial amplitude δ_i) whose length-scale are smaller than the cosmological horizon generates shocks in near critical solutions because of the presence of decreasing modes. We will thus need to test super-horizon fluctuations to try and avoid this behaviour.

3.4.2 Tests with initial conditions from the long-wavelength approximation

We thus follow the advises of [Musco et al. 2009] and take a fluctuation starting in the super-horizon regime that admits only growing modes when entering the horizon. To achieve that, we use initial conditions computed from the long-wavelength approximation presented in section 2.4.2, still in the $1 + \log$ slicing. The parameter Δ of profile (2.4.69) is chosen such that the initial areal radius of the fluctuation is three-times the Hubble radius $R_H = H^{-1}$. In such a way, all the decreasing modes have disappeared when the size of the inhomogeneity coincides with the cosmological horizon. The second parameter, A , denotes the amplitude of the overdensity and will thus also influence the value of the critical equation of state ω^* . We perform two sets of simulation, one with $\omega_1^* \simeq 0.337$ and the other with $\omega_2^* \simeq 0.434$.

The masses of the formed black holes, rescaled by the horizon mass M_H (the mass inside the horizon computed at the time the fluctuation enters the Hubble radius), are shown in Fig. 3.24. It is clearly visible, in both cases, that the plotted quantity is

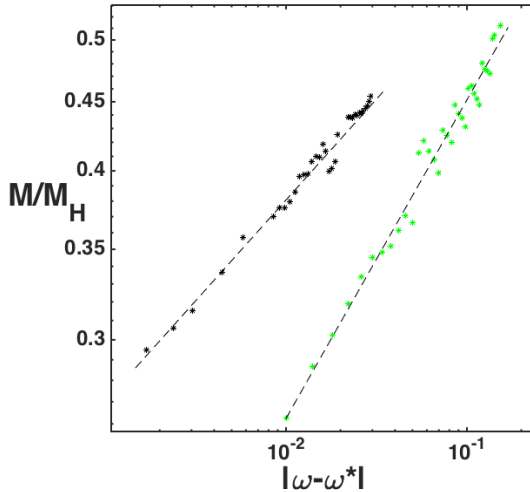


Figure 3.24 – Mass, by units of horizon masses, of the formed black hole computed with the $1 + \log$ slicing for two families of profiles. Black dots represent family 1, with $\omega_1^* \simeq 0.334$, while green ones represent family 2, with $\omega_2^* \simeq 0.434$. In both cases, dots seem to be globally on the same line, indicating a power-law and, thus, that the universality relation is verified. The slope of the line depends on the family of profiles.

rescaling in a power-law of $|\omega - \omega^*|$, although our code does not permit to obtain perfect lines and values nearer the critical solution. This is thus a serious indication in favour of universality. Note that the critical exponent γ is shown to vary as a function of the amplitude of the profiles.

We can draw two major conclusions from this. First, our simulations with sub-horizon and conformally flat initial conditions, though interesting and relevant, revealed a breakdown of universality close to ω^* . Secondly, the universal scaling law seems to be verified when using super-horizon initial conditions with exclusively growing modes. This is perfectly in agreement with [Hawke and Stewart 2002], [Musco et al. 2009] and [Musco and Miller 2013]. They worked by fixing the equation of state and varying the matter profile. On our side, we showed universality with respect to the matter type by varying the equation of state parameter and this is the major original result of this thesis. It should however be checked with a more efficient code, equipped with an adaptive mesh-refinement specially designed for spherical symmetric space-times like the one used by [Musco and Miller 2013], to be proven definitely.

3.4.3 The static Minkowski case

We now investigate the validity of the universality in the case of a static Minkowski background. In this latter case, we hope the code to work more easily since the outer boundary conditions should be less problematic. Our code was not built to deal with an empty background but the only differences consist in the scales and the initial

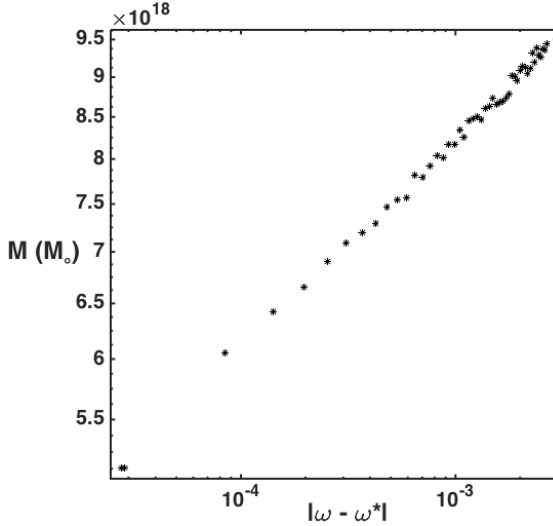


Figure 3.25 – Mass of the formed black hole in a Minkowski background computed with the 1 + log slicing. The power law is clearly visible, proving universality in this case.

conditions. The time, length and mass scales are now given by $t_{\text{scale}} = \frac{GM_{\odot}}{c^3}$ (in s), $l_{\text{scale}} = \frac{GM_{\odot}}{c^2}$ (in m) and $m_{\text{scale}} = M_{\odot}$ (in kg), while the initial profile is based on the energy-density profile instead of the energy-density contrast profile because $\bar{e}_m = 0$:

$$e_m^i(r) = e_m^i \frac{1 - \tanh\left(\frac{r-r_m^i}{2}\right)}{1 + \tanh\left(\frac{r_m^i}{2}\right)}, \quad (3.4.4)$$

where e_m^i is the initial amplitude of the object and r_m^i its initial radius. We work in code units and take as initial conditions $e_m^i = 10^{-5}$ (which corresponds to $6.18 \times 10^{15} \frac{\text{kg}}{\text{m}^3}$) and $r_m^i = 20$ (which corresponds to 2.95×10^4 m), with an initial compactness of 0.048. We use again the 1 + log slicing to observe the complete formation of black holes. All this gives us as critical ω^* the value of 0.0094 and the evolution of the mass of the black hole, that we follow until its formation, with respect to $|\omega - \omega^*|$ is shown in Fig. 3.25. In this plot, we observe that all points lie nearly perfectly along a straight line, indicating a power law and thus universality. This is in agreement with [Choptuik 1993] and generalises universality to one particular 1-parameter family of matter species, in a Minkowski background.

3.4.4 The de Sitter case

Our last test will be the case of an empty space with a positive cosmological constant Λ . We use the same energy profile as in the previous test with $e_m^i = 10^{-5}$ and $r_m^i = 20$. The initial Hubble factor is set to $H_i = 3 \times 10^{-5}$ and $\Omega_{\Lambda} = 1$, in such a way that

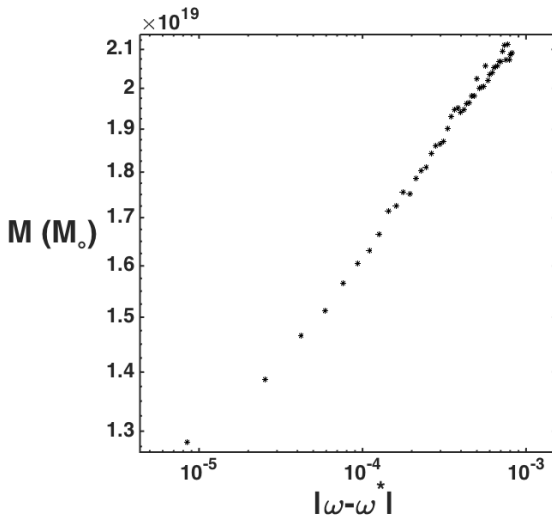


Figure 3.26 – Mass of the formed black hole in a de Sitter background computed with the 1 + log slicing. The power law is clearly visible, proving universality in this case.

the value of Λ is fixed by H_i . The 1 + log slicing is used to follow the black holes formations.

With this, the critical solution appears to be around $\omega^* \simeq 0.0128$. The mass of the formed black holes, with respect to $|\omega - \omega^*|$ is shown in Fig. 3.26. We observe that all the points are along a straight line, revealing the universal scaling law. As well as in the Minkowski case, we thus proved universality in the de Sitter case which is relevant from the cosmological point of view.

3.5 Conclusion

In conclusion of this chapter, we have proven universality for pressured matter in the cases of a Minkowski and a de Sitter background, which is a completely original result. The full matter Friedmann universe case is more tricky, probably because of the outer boundary condition for the hydrodynamical terms and the need of an adaptive mesh refinement. But, when taking a super-horizon fluctuation computed from the long-wavelength approximation as initial conditions, we obtained a serious indication in favour of the universal scaling law. The power-laws we saw should be tested closer to the critical solution but we do not have the most adapted tool to explore that region. We showed the beginning of the scaling law, future studies should work on the consolidation of this new result.

Chapter 4

Influence of the Thermal History on Primordial Black Holes Formation

Summary

This chapter is a concrete application of our numerical code to a cosmological problem: the formation of Primordial Black Holes (PBH). These particular black holes may have gravitationally formed during the radiation era and could possibly be a part or all of the unknown Dark Matter. We worked jointly with Sébastien Clesse on the basis of the paper [Carr et al. 2019b] that used different dips of the equation of state, appearing at different phase transitions and when some particles become non relativistic due to the decrease of the temperature, to compute the corresponding PBH mass function. This article used, as threshold value for PBH formation, for each value of the equation of state ω , the threshold computed in the case of a constant ω from [Musco and Miller 2013]. The results of this is a PBH mass function that satisfies cosmological and astronomical constraints and also gives solutions to some unsolved cosmological problems. We tried to go further in the study by considering, contrary to what is done in [Carr et al. 2019b], the time dependance in the equation of state in our simulations to compute the time-dependent corresponding threshold for PBH formation. The result is a PBH mass function with less accentuated peaks shifted towards lower masses. This seems to be in contradiction with the hypothesis that Dark Matter is made of Primordial Black Holes but this could finally be a gauge effect. We end by analysing the possible improvements for future works to confirm or infirm our results.

4.1 Problem setting

Primordial black holes (PBH) are a subject widely studied in the history of cosmology. These black holes may have formed gravitationally during the radiation era. Precursor works of S. Hawking [Hawking 1971], [Hawking 1975], B. Carr [Carr and Hawking 1974], [Carr 1975] and G. Chapline [Chapline 1975] in the 1970's gave birth to the notion of PBH. The idea that they could constitute a part, and possibly all, of the dark matter is already present in these works. By the end of the 1990's, the MACHO project observed gravitational microlensing caused by small objects in the galactic halo (where one does not expect to have populations of neutron stars or stellar black holes). This enhanced the interest for PBH since it could be at the origin of these observations. But a few years later, in the 2000's, the EROS survey deduced stronger constraints, also from microlensing events, that exclude PBH with mass $10^{-3}M_{\odot} \leq M \leq 1 - 10M_{\odot}$. In 2008, the paper [Ricotti et al. 2008] computed constraints from the Cosmic Microwave Background (CMB) that also exclude more massive PBH. The interest for PBH thus strongly reduced and the hypothesis they could be a part of dark matter was nearly forgotten.

However, the first observation of gravitational waves emitted by merging black holes [Abbott et al 2016] has rekindled interest in PBH because the involved black holes have mass around $30M_{\odot}$ and weak spin, which was quite unexpected. Moreover, the constraints from the CMB were re-analysed and in fact exclude only PBH with mass greater than $100M_{\odot}$. Concerning the constraints obtained from the gravitational microlensing, it can be evaded in case the PBH are grouped in halos, which is not improbable. All this shows that PBH as part of dark matter remains a viable possibility and this is the context of this chapter.

During the post-inflation thermal history of universe, the equation of state parameter ω undergoes several dips, like the important one (around 30%) at the Quantum Chromodynamics (QCD) transition, when protons and neutrons condense out of quarks and gluons (see [Carr et al. 2019b]). The equation of state changes each time the number relativistic degrees of freedom decreases, due to the decrease of temperature that reaches the transition of a particle to become non relativistic. The resulting equation of state is shown in Fig. 4.1. We know, thanks to numerous studies such as [Musco and Miller 2013], that the critical energy density δ_c (threshold of the energy density computed when the fluctuation enters the cosmological horizon) for the formation of PBH reduces with ω . This means that the probability for a PBH to form increases during these different dips in the equation of state.

The papers [Carr et al. 2019a],[García-Bellido et al. 2019], and the early work [Jedamzik 1997], explore that feature by looking at the consequences of the QCD transition on the PBH mass function. In [Carr et al. 2019b] the authors also used other dips in the sound speed in their computation and took a scale-invariant power-spectrum of primordial density fluctuations. They explained that the resulting PBH mass function, assuming that PBHs constitute all the dark matter, satisfies all the known astrophysical and cosmological constraints but would also explain several unresolved interrogations linked to some microlensing events, supermassive black holes, dwarf galaxies,... (see the article for more details).

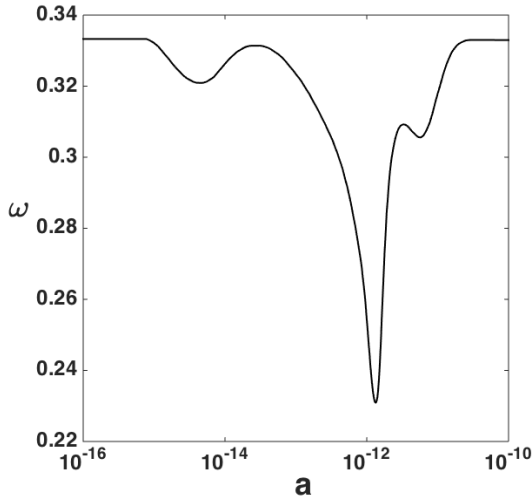


Figure 4.1 – Variation of the equation of state with respect to the cosmological scale factor.

These different works used as values for the critical delta $\delta_c(\omega)$ the ones computed from simulations with a constant equation of state ω , such as in [Musco and Miller 2013]. This can seem reasonable but we think that this may lead to important differences by comparison with simulations using the time-dependent equation of state of Fig. 4.1. Indeed, the dips in ω have a very short duration in time and this could have two consequences on the mass function. First, the amplitude of its peaks could have been overestimated because the average equation of state during a collapse process, leading to the formation of a PBH, should always be larger than its minimum value. Second, these peaks should be shifted towards lower masses since the critical delta is computed at the time the fluctuation enters the Hubble horizon, which is far before the PBH formation. In other words, the mass function from [Carr et al. 2019b] neglects the duration of the PBH formation process, considering it as a punctual event. This gives an interesting result but, at that time scale, we think that an even better approximation can be performed by considering a really time-dependent equation of state. This is what we will do in this chapter : implementing the time dependance of ω and computing the different thresholds $\delta_c(a)$ as a function of the values of the scale factor a at the times the critical delta will be calculated. The results of these computations will allows us to obtain a new approximation of the PBH mass function and to compare it with the previous one.

4.2 A time dependent equation of state

We will compute the critical amplitude $\delta_c(a)$ for several values of a at the "horizon crossing-time", the time when the areal radius of the fluctuation R_m coincides with the

Hubble radius R_H . We know, from [Musco 2019], that this value generally depends on the initial density profile. We will test two kinds of initial conditions : the conformally flat curvature profile (2.4.12) and the long wavelength solution (2.4.69). These Gaussian profiles of curvature produce mexican-hat profiles for the energy-density-contrast and are widely used in the context of cosmological fluctuations ([Niemeyer and Jedamzik 1999], [Musco et al. 2005],[Musco and Miller 2013]). In [Musco 2019], the same profile has been used in the comoving gauge and the value critical delta for a radiation fluid, for which $\omega = \frac{1}{3}$, has been found to be $\delta_c \simeq 0.55$. In [Carr et al. 2019b], they use the value 0.4, from [Musco and Miller 2013], and each value $\delta_c(\omega)$ from this article. But, as explained in [Musco 2019], these values were obtained by defining the coordinate radius of the fluctuation r_0 as the smallest radius where $\delta(r_0)$ is equal to zero. We already mentioned in section 3.2 that the radius of the fluctuation should rather be taken as the location r_m of the maximum of the compaction function. Indeed, considering r_0 give results that depends too much on the density profile by comparison with taking r_m . This is what is done in [Musco 2019] and this is the origin of this difference in the value of the critical delta.

On our side, we work in the $1 + \log$ slicing which appeared to be the most efficient one in our tests of Chapter 3. Our results will thus be different from those in the mentioned article. By examining the coefficient of the expression (2.4.61) of the long-wavelength solution and comparing with the one in the comoving gauge found in [Harada et al. 2015], we obtained that the δ computed in the comoving slicing is equal to a certain constant $C(\omega)$ times the δ computed in the $1 + \log$ slicing, up to fourth order. This constant, which has the value

$$C(\omega) = 3 \left(\frac{\omega + 1}{3\omega + 5} \right) \left[\frac{3(1 + \omega)(7 + 3\omega) + 2(1 + 3\omega)^2}{3(1 + \omega)(7 + 3\omega)} \right], \quad (4.2.1)$$

is valid in the case of a constant equation of state. However, we will assume it is a good approximation in the case of a time-dependant equation of state. The value for radiation is $C(\omega = \frac{1}{3}) = \frac{5}{6}$, which means that our results should give critical values for δ rather around 0.6 than around 0.5 or 0.4.

In both cases, in the conformally flat and the long-wavelength solution, the initial areal radius is chosen to be three times the Hubble radius to make the decreasing modes disappear, like in the last cosmological tests of section 3.4. Although these are the most realistic kinds of initial conditions we can take, the long-wavelength approximation in this form is not perfect either. The derivation of this solution in section 2.4.2 considers only the case of a constant equation of state. Our simulations will thus suffer from little inaccuracies but should however give a good estimation of the PBH mass function. On the other hand, the conformally flat initial conditions are perfectly correct from the general relativity point of view.

4.3 Results and consequences

The results of these simulations are shown in Fig. 4.2, where the critical energy-density contrast $\delta_c(a)$ computed with conformally flat initial conditions and with the

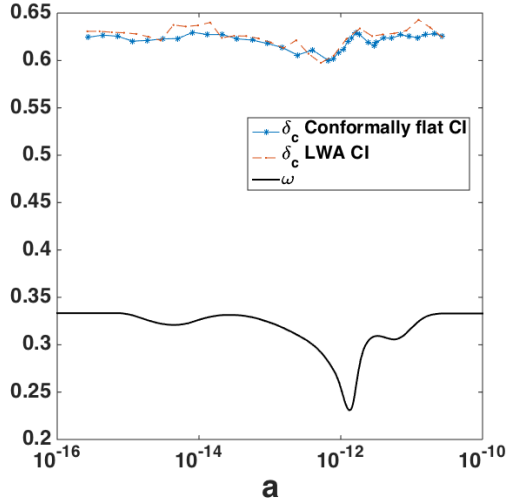


Figure 4.2 – Critical delta computed with the conformally flat initial conditions (blue stars) and with the initial condition from the long-wavelength approximation (dotted red line). The variable equation of state is represented in black.

long-wavelength approximation are both represented. The first observation is that there are few differences between the two simulations, so few we can assume that both initial conditions give the same results.

As we mentioned above, we must rescale these results by a factor that depends on the equation of state to compare with the comoving gauge. For the radiation, this factor is equal to $\frac{5}{6}$ and for a general equation of state it is equal to $C(\omega)$, the constant of (4.2.1). These two rescalings are visible on Fig. 4.3. A constant rescaling will have no impact on the mass function but the rescaling by $C(\omega)$ has its importance because the peaks are amplified. As expected, the peaks in $\delta_c(a)$ appear a bit earlier than those in $\omega(a)$ and their amplitudes are smaller than in the case of a constant equation of state. Note that we represented these curves with respect with the PBH mass they are playing for.

Finally we compute the PBH mass function associated to these results by using the following formula from [Carr et al. 2019b] :

$$f_{\text{PBH}}(M) = \frac{1}{\rho_{\text{CDM}}} \frac{d\rho_{\text{PBH}}}{d\ln M} \approx 2.4\beta(M) \sqrt{\frac{M_{\text{eq}}}{M}}, \quad (4.3.1)$$

where $M_{\text{eq}} = 2.8 \times 10^{17} M_{\odot}$ is the horizon mass at matter-radiation equality, 2.4 corresponds to $2 \left(1 + \frac{\Omega_b}{\Omega_{\text{CDM}}}\right)$ with $\Omega_b = 0.0456$ being the baryon density parameter and $\Omega_{\text{CDM}} = 0.245$ the cold dark matter (CDM) density parameter. The quantity $\beta(M)$ is

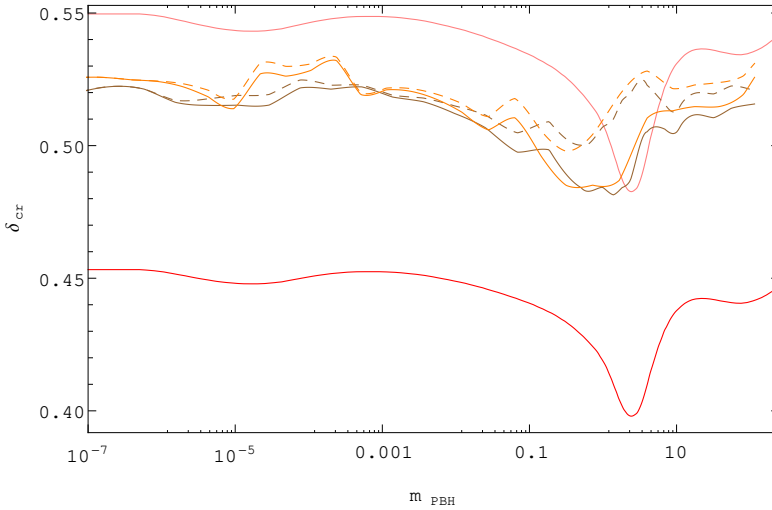


Figure 4.3 – Critical delta computed in the $1 + \log$ slicing rescaled by a factor $C(\omega)$ (brown and orange solid lines for conformally flat and long-wavelength initial conditions, respectively). Those curves are also shown with a constant rescaling (respective dotted lines). The solution for a constant equation of state ω computed by [Musco and Miller 2013] is represented in red. This last curve has been rescaled in pink to be congruent with [Musco 2019] which obtained values near 0.55 instead of 0.45.

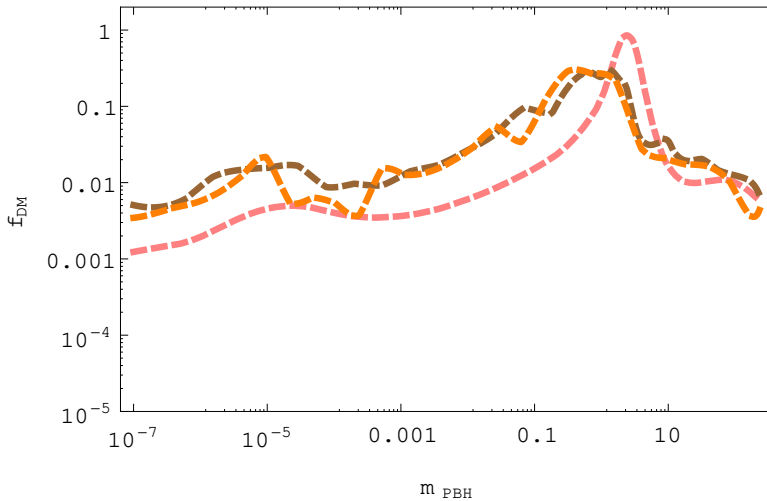


Figure 4.4 – PBH Mass function as a function of the mass (per unit of Solar mass M_{\odot}) for the case where PBH constitute all the Dark Matter. The brown and orange curves are obtained with our simulations taking conformally flat and long-wavelength initial conditions, respectively. The pink curve is the one computed in [Carr et al. 2019b].

the fraction of horizon patches undergoing collapse to PBHs given by

$$\beta(M) \approx \text{erfc} \left[\frac{\delta_c(\omega)}{\sqrt{2}\delta_{\text{rms}}(M)} \right], \quad (4.3.2)$$

where "erfc" is the complementary error function and we supposed that PBHs are formed from Gaussian inhomogeneities with root-mean-square amplitude δ_{rms} given by the quasi-scale-invariant spectrum

$$\delta_{\text{rms}}(M) = A \left(\frac{M}{M_{\odot}} \right)^{\frac{1-n_s}{4}}, \quad (4.3.3)$$

with $A = 0.1487$ and $n_s = 0.97$ free parameters chosen to have a total integrated mass function $f_{\text{PBH}}^{\text{tot}} = 1$, assuming that the totality of Dark Matter is made of PBHs. The PBH mass function consists in a distribution mass function of the PBH.

The obtained resulting function is shown in Fig. 4.4. The results are sufficiently clear, despite the visible imperfect accuracy of the simulations : the peaks were shifted towards lower masses, and were quite attenuated. This is what we expected before the calculations because the average equation of state during the PBH formation process is greater than the particular value of the dips and takes a quite long time. Moreover, there seems to be a spread of the QCD peak since our PBH mass function appears to have a higher level than in [Carr et al. 2019b]. The question now is to know if it is in favour or against the hypothesis that Dark Matter is made of PBH. Considering only our new simulations, the peaks are in fact too small to support the hypothesis and rather reject it. The problem is that it indicates that the PBH mass function stays around 0.1 until large masses, which is in contradiction with some astrophysical constraints such as the CMB. But our results are not yet totally robust and should form the basis for further studies. Of course, the accuracy of the computation could be better to obtain a smooth curve following efficiently all the dips in $\omega(a)$. But we would rather like to point one important aspect concerning the methodology. The PBH mass function is computed from the value of the critical delta $\delta_c(a)$ and we know that it is exponentially sensitive to it (see [Carr 1975],[Carr et al. 2019b]). Now, we know (thanks to [Harada et al. 2015], [Musco 2019] but also our simulations) that this threshold value depends on (1) the way it is computed (by considering r_0 , r_m or any other way), (2) the shape of the fluctuation (Gaussian, mexican-hat,...), and (3) the gauge that is used. The two first criteria can easily be fixed since they depend only on the model. But the dependence on the gauge is theoretically a problem because the PBH mass function should ideally be gauge invariant. It is thus possible that the rejection of the hypothesis that Dark Matter is made of PBH is not correct as this is due to a gauge effect.

We must say that another free parameter was fixed in the last simulations: the ratio of the PBH mass and the horizon mass at re-entry, denoted by γ was fixed to 0.7. But this value could be numerically computed to obtain a better value.

Another remark is that the formula (4.3.1) does not take into account the time for a PBH to form. The resulting curve could then have been too much shifted towards

lower masses. Moreover, it also considers that every fluctuation with the same radius will produce a PBH with the same mass whatever its initial amplitude. This is generally not true and could be modified in the model.

To go further, we think that a gauge invariant criteria should be found to determine if a fluctuation will collapse to a black hole or not. We do not have an answer to this problem. We thus let for future works the opportunity to confirm (or infirm) our results with more simulations involving an AMR and, why not, another gauge and other density profiles. To summarize, the main points to pursue our work of this chapter are :

- The efficiency of the code (AMR and possibly upgrade the outer boundary conditions). But this is also valable for the work of chapter 3.
- To incorporate the duration of the PBH process in formula (4.3.1) and the fact that fluctuations with the same radius but with different amplitudes generate PBHs with different masses.
- To make start all the simulations far before the first dip of the equation of state to ensure the long-wavelength approximation is completely acceptable. But this is only possible with a code that is sufficiently stable to allow very long evolutions.
- To perform the simulations also in the comoving gauge to see if the factor $C(\omega)$ is an acceptable rescaling to convert the $1 + \log$ slicing into the comoving gauge.
- To find a quantity that is less gauge dependent than the critical delta δ_c .

Conclusion

It is time now to conclude after having worked no less than four years on this thesis. Initially, we wished to study the impact of Dark Energy on the cosmological structure formation. But after the implementation of the code, we realized that working only on the spherical collapse of a barotropic fluid of matter with constant equation of state would constitute a consequent work. We then decided to go in that direction and let the problematic of Dark Energy for future studies.

As intended, we upgraded the numerical code built by J. Requier during his Ph. D and used in his works ([Requier et al. 2015], [Requier 2015] and [Requier et al. 2016]). Our goal was to add the possibility to evolve one (or several) matter field with pressure to explore for example the radiation era or the epoch of matter-radiation equivalence. We achieved this by using the Valencia formulation of relativistic hydrodynamics in spherical symmetry and solved these additional equations with a HRSC Godunov-type method. A tricky point, discussed in Chapter 3, was the way to impose the cosmological outer boundary conditions because it seems to be still quite experimental in the literature. The radiative boundary condition we used is supposed to avoid outgoing waves to be reflected but some nasty numerical noise remains and causes instabilities. This is why we had to try to put the outer boundary as far as possible from the central fluctuation. But we could not avoid the cosmological horizon to reach this boundary at a certain time, generally breaking the simulation down. However, we could exploit this numerical tool and obtain the interesting results that are presented in this manuscript. Moreover, we hope to have exposed in Chapter 2 an easy to understand recipe that exhibits, in a not too technical way, the key-points to have in mind when building a numerical relativity code.

By testing the code and varying the equation of state parameter ω , we made two interesting observations. First, we saw that the central energy-density contrast δ_0 evolution does not necessarily reflect the global behaviour of a fluctuation. Indeed, some simulations with large equation of state show a spherical bounce that leads to a negative δ_0 while the average density contrast δ_m remains positive. Considering only the central value can thus lead to misinterpretations when pressure is involved. In General Relativity, the question of the observables is however always tricky because of the gauge dependence of the tensor components. Even such an important quantity as the energy-density contrast is gauge dependent because it consists in a local-background

comparison of variables that do not share the same proper time. Our simulations in the synchronous gauge convinced us that the really relevant observable in the spherical collapse is not the energy-density contrast but the compactness, which is also a dimensionless quantity.

Our simulations also revealed that, for a fixed profile of matter (or, equivalently, of curvature), there exists a critical value ω^* of the equation of state under which the fluctuation collapses to a black hole and above which it is diluting into the background. For super-critical solutions, we saw that the late-time negative growth rate of the compactness of the fluctuation is decreasing linearly with ω and that the slope of this relation seems to be independent on the size of the fluctuation. This indicates that, after a certain time, every fluctuation decreases in the same way, governed exclusively by the cosmological background. For sub-critical solutions, that is to say collapsing solutions, we rapidly conjectured that the mass of the formed black holes should obey the universal scaling law appearing in various critical phenomena. We knew from the literature that the spherical collapse was universal with respect to the shape of curvature profile, we saw no reason for it not being also universal with respect to the matter type. We thus tried to prove it in three different cases: a homogeneous Friedmann background, an empty Minkowski background and an empty de Sitter background.

For the Friedmann case, first tests in the synchronous gauge gave indications in favour of universality, but the well known bad behaviour of these coordinates prevented us to trust this result. This is why we also tested the harmonic slicing, which gave similar results. By using the $1 + \log$ slicing, we could follow the gravitational collapse until the black hole formation and then compute precisely its mass. Unfortunately, no scaling law was visible, possibly because we could not go as close as necessary to the critical solution to observe it. The other possibility is that we encountered a similar behaviour as in [Hawke and Stewart 2002] who saw a breaking of universality near the critical solution because of the use of conformally flat and sub-horizon initial conditions that possess decreasing modes. To bypass this problem, we had to implement super-horizon initial fluctuations with exclusively growing modes. This led us to derive, in any Bona-Masso slicing given by eq. (2.3.9), the solution of the equations in the long-wavelength approximation. This original development, which is interesting in itself because of its similitude to the same solution in [Harada et al. 2015] in other gauges, allowed us to evolve more realistic initial conditions. With it, we could finally observe the universality scaling law we were looking for. The result is not perfect since we could not approach the critical solution as close as we wished, an adaptive mesh refinement should be used to perform this, but it gives more than an indication that universality is true in this case. Concerning the case of a Minkowski background, which concerns the astronomical scale rather than the cosmological scale, the $1 + \log$ slicing appeared to be very efficient. This is probably due to the simplified (empty) outer boundary conditions that render the code more stable. However, we showed complete universality in this case. The de Sitter case, which has important cosmological implications such as the primordial black holes formation during the inflationary era, showed results similar to the Minkowski one: universality holds also in this configuration! These results are important because it is a generalisation of numerous previous works: the gravitational spherical collapse appears to

happen in a very general way that depends little on the initial curvature profile and, we know it now thanks to our own work, the types of matter (through the equation of state parameter ω).

The second research project concerned the formation of Primordial Black Holes (PBH) and followed the work [Carr et al. 2019b] which claims that PBH could be a part of all of the Dark Matter (DM). The equation of state undergoes several dips during the post-inflation thermal history, corresponding to the time the temperature makes some particles to reach a transition that produces a decrease of the number relativistic degrees of freedom. The greater dip corresponds to the Quantum Chromodynamics transition with the formation of protons and neutrons, but other transitions are also considered. The idea was to see if taking a really time-dependant equation of state, including the dips in question, all along the evolution would impact a lot the PBH mass function derived in [Carr et al. 2019b], where each punctual solution at time t_0 is computed with a model with constant $\omega(t_0)$. To achieve it, we computed at several times t the corresponding threshold value $\delta_c(t)$ for PBH formation. As expected, this critical delta $\delta_c(t)$ appeared to have less pronounced dips which occur earlier than those used in [Carr et al. 2019b]. The resulting PBH mass function, that depends exponentially on δ_c , showed flattened peaks shifted to lower masses but a higher level over large range of low masses. This was predictable but the peaks are so attenuated that this goes against the hypothesis that DM is made of PBH.

This result, that has the merit to raise the question, nevertheless suffers from some inaccuracies. These are due to the imperfections of our numerical code but it comes mostly from gauge dependency that avoids to confidently compare the two curves. Our results were computed in the $1 + \log$ slicing because it appeared to be the most efficient gauge working on our code while the original work was designed in the co-moving gauge. We derived the conversion formula from one gauge to the other in the long-wavelength approximation to give the best comparison we could. But we know it cannot be exact since the critical energy-density contrast is computed, by its definition, at the very limit of the area of validity of the long-wavelength approximation. Moreover, this quantity has been shown to depend also on the curvature (or density) profile in [Musco 2019]. This asks again the important question of the observables : which observables do we have to use to have as few gauge effects and profile dependences as possible? The question remains open but, as noticed in Chapter 3, the compactness seems to be an interesting candidate. Another clue comes from the very recent article [Escrivà et al. 2020] which showed numerically that the threshold for black hole formation in terms of the averaged compaction function does not depends on the curvature profile. This is maybe the right parameter to investigate in future studies.

The critical collapse and, more generally, the spherical collapse are studies that can be declined in numerous ways by using numerical relativity, depending on the fluid(s) of matter, the Dark Energy model, the cosmological epoch, the scale of interest, the coupling between the source terms, ... This thesis provides lots of perspectives for future works. We give now some of these in what follows.

We implemented two types of initial conditions in our code : the conformally flat profiles by parametrising either the density profile or the curvature profile and the pure

growing solution coming from the long-wavelength approximation. The advantages of the first ones is that they are very simple, perfectly correct from the theoretical point of view and can easily be compared with the top-hat model which is still used in the literature of structures formation. But they possess non growing modes, which is problematic for the study of PBH, and their artificiality generates unnatural transients effects as it had already been noticed in [Rekier 2015]. The long-wavelength approximation has the opposite properties: such initial conditions are more natural and possess exclusively growing modes but are only an approximation. Moreover, they cannot be implemented in sub-horizon regime. However, while computing the threshold values $\delta_c(t)$ for a time-dependent equation of state, we observed very few differences between the two solutions. It would then be interesting to study the real impact of taking one solution or the other within the frame of the critical collapse. Will a super-horizon conformally flat fluctuation finally coincide with the long-wavelength solution when every decreasing mode has faded away? If it appeared that there is no significant difference between the two solutions at the time the fluctuation enters the cosmological horizon, this would probably mean that one of the most important things concerning the numerical evolution of fluctuations is that it must start with a length-scale far greater than the Hubble radius at initial time.

We used the barotropic constant equation of state $p = \omega e$, where e is the energy-density and p is the pressure because this is what is commonly considered in cosmology. However, other equations of state are often used in the astrophysical case, such as the one for an ideal fluid (1.6.1) and the one for a polytropic fluid (1.6.2). Threshold values of the parameters contained in these equations and the associated critical phenomenon could be examined. This would extend again universality with respect to a larger panel of matter species or, on the contrary, lead to the discovery of a breaking of the universality.

As explained in the Introduction and in Chapter 2, the code was designed to evolve possibly two non interacting fluids of matter, with a scalar field and a cosmological constant. In this work, we only explored the case of a single fluid of matter but any other combination of the previous ingredients is possible. For example, the late time evolution of pressured matter minimally (or not) coupled to a scalar field would have interesting cosmology applications. This was even one of the perspectives given in [Rekier 2015] and we still leave it for future projects. A second obvious application would be the study of structure formation at the epoch of matter-radiation equivalence since we can evolve conjointly dust and radiation, during the inflation era or in a de Sitter background. A third application would be the study of voids since a negative energy-density contrast can easily be implemented.

From the numerical relativity point of view, we built an code which appeared to have some imperfections. Some improvements could be performed, such as the implementation of an adaptive mesh refinement or a logarithmic spatial discretization. The implementation of a non zero shift gauge, like the gamma-driver one, could be interesting too. But the question of the implementation of the cosmological boundary conditions is more tricky and would probably require a research work in itself. Numerical relativity is a subject currently on the rise, thanks to the active field of gravitational waves. It is becoming more and more employed within the frame of cos-

mology, especially concerning the PBH formation but not only, and we hope to have enhance a bit the marriage of the two disciplines.

Whether with our code or any other, whether in the comoving gauge or not, whether in numerical relativity or not, we hope this work will interest future young researchers and spark the desire to jump in the sky and try to understand gravitation, determine the nature of Dark Matter and Dark Energy, simulate black holes formation and evolution or explore other models of gravity as [Rekier 2015] and others did for me.

Bibliography

- B. P. Abbott et al. Observation of gravitational waves from a binary black hole merger. *Physical Review Letters*, 116(6), 2016. doi: 10.1103/PhysRevLett.116.061102.
- M. Alcubierre. *Introduction to 3+1 Numerical Relativity*. Oxford University Press (OUP), New York, 2008.
- M. Alcubierre and J. A. González. Regularization of spherically symmetric evolution codes in numerical relativity. *Computer Physics Communications*, 167(2):76 – 84, 2005. ISSN 0010-4655. doi: <https://doi.org/10.1016/j.cpc.2005.01.008>. URL <http://www.sciencedirect.com/science/article/pii/S0010465505000597>.
- M. Alcubierre and M. D. Mendez. Formulations of the 3+1 evolution equations in curvilinear coordinates. *General Relativity and Gravitation*, 43(10):2769–2806, Jun 2011. ISSN 1572-9532. doi: 10.1007/s10714-011-1202-x. URL <http://dx.doi.org/10.1007/s10714-011-1202-x>.
- M. Alcubierre, B. Brügmann, P. Diener, M. Koppitz, D. Pollney, E. Seidel, and R. Takahashi. Gauge conditions for long-term numerical black hole evolutions without excision. *Physical Review D*, 67(8), Apr 2003. ISSN 1089-4918. doi: 10.1103/physrevd.67.084023. URL <http://dx.doi.org/10.1103/PhysRevD.67.084023>.
- A. Arbona and C. Bona. Dealing with the center and boundary problems in 1d numerical relativity. *Computer Physics Communications*, 118(2):229 – 235, 1999. ISSN 0010-4655. doi: [https://doi.org/10.1016/S0010-4655\(99\)00191-5](https://doi.org/10.1016/S0010-4655(99)00191-5). URL <http://www.sciencedirect.com/science/article/pii/S0010465599001915>.
- R. Arnowitt, S. Deser, and C. W. Misner. The dynamics of general relativity. In L. Witten, editor, *Gravitation : an introduction to current research (Chap. 7)*, pages 227–265. John Wiley and Sons Inc, New York, London, 1962.

- F. Banyuls, J. A. Font, J. M. Ibanez, J. M. Martí, and J. A. Miralles. Numerical $3 + 1$ general relativistic hydrodynamics: A local characteristic approach. *The Astrophysical Journal*, 476(1):221–231, Feb 1997. ISSN 1538-4357. doi: 10.1086/303604. URL <http://dx.doi.org/10.1086/303604>.
- T. W. Baumgarte and S. L. Shapiro. Numerical integration of einstein’s field equations. *Physical Review D*, 59(2), Dec 1998. ISSN 1089-4918. doi: 10.1103/physrevd.59.024007. URL <http://dx.doi.org/10.1103/PhysRevD.59.024007>.
- T. W. Baumgarte and S. L. Shapiro. *Numerical Relativity: Solving Einstein’s Equations on the Computer*. Cambridge Univ. Press, Cambridge, 2010.
- T. W. Baumgarte, P. J. Montero, I. Cordero-Carrion, and E. Müller. Numerical relativity in spherical polar coordinates: Evolution calculations with the bssn formulation. *Physical Review D*, 87(4), 2013. doi: 10.1103/PhysRevD.87.044026.
- M. Berger and P. Colella. Local adaptive mesh refinement for shock hydrodynamics. *Journal of Computational Physics*, 82(1):64 – 84, 1989. ISSN 0021-9991. doi: [https://doi.org/10.1016/0021-9991\(89\)90035-1](https://doi.org/10.1016/0021-9991(89)90035-1). URL <http://www.sciencedirect.com/science/article/pii/0021999189900351>.
- M. J. Berger and J. Olinger. Adaptive mesh refinement for hyperbolic partial differential equations. *Journal of Computational Physics*, 53(3):484 – 512, 1984. ISSN 0021-9991. doi: [https://doi.org/10.1016/0021-9991\(84\)90073-1](https://doi.org/10.1016/0021-9991(84)90073-1). URL <http://www.sciencedirect.com/science/article/pii/0021999184900731>.
- C. Bona, J. Massó, E. Seidel, and J. Stela. New formalism for numerical relativity. *Physical Review Letters*, 75(4):600–603, 1995. doi: 10.1103/PhysRevLett.75.600.
- H. Bondi. Spherically symmetrical models in general relativity. *Mon. Not. Roy. Astron. Soc.*, 107:410, 1947.
- W. B. Bonnor. The formation of the nebulae. *Z. Astrophys.*, 39:143, 1956 (Reprinted as *Gen. Rel. Grav* in 1998).
- B. Carr, S. Clesse, and J. García-Bellido. Primordial black holes, dark matter and hot-spot electroweak baryogenesis at the quark-hadron epoch. *1904.02129*, 2019a.
- B. Carr, S. Clesse, J. García-Bellido, and F. Kuhnel. Cosmic conundra explained by thermal history and primordial black holes. *1906.08217*, 2019b.
- B. J. Carr. The primordial black hole mass spectrum. *The Astrophysical Journal*, 201: 1, Oct 1975. ISSN 1538-4357. doi: 10.1086/153853. URL <http://dx.doi.org/10.1086/153853>.
- B. J. Carr and S. W. Hawking. Black holes in the early universe. *Mon. Not. Roy. Astron. Soc.*, 168:399, 1974.

- G. F. Chapline. Cosmological effects of primordial black holes. *Nature*, 253(5489): 251–252, Jan 1975. ISSN 1476-4687. doi: 10.1038/253251a0. URL <http://dx.doi.org/10.1038/253251a0>.
- M. W. Choptuik. Universality and scaling in gravitational collapse of a massless scalar field. *Physical Review Letters*, 70(1):9–12, 1993. doi: 10.1103/PhysRevLett.70.9.
- Y. Choquet-Bruhat. *General relativity and Einstein's equations*. Oxford University Press (OUP), New York, 2009.
- Y. Choquet-Bruhat and R. Geroch. Global aspects of the cauchy problem in general relativity. *Communications in Mathematical Physics*, 14(4):329–335, Dec 1969. ISSN 1432-0916. doi: 10.1007/bf01645389. URL <http://dx.doi.org/10.1007/BF01645389>.
- I. Cordero-Carrion and P. Cerda-Duran. Partially implicit runge-kutta methods for wave-like equations. 2016.
- G. Darmais. *Les équations de la gravitation einsteinienne*. Gauthier-Villars, 1927.
- P. A. M. Dirac. The theory of gravitation in hamiltonian form. *Proceedings of the Royal Society of London. Series A. Mathematical and Physical Sciences*, 246 (1246):333–343, Aug 1958. ISSN 2053-9169. doi: 10.1098/rspa.1958.0142. URL <http://dx.doi.org/10.1098/rspa.1958.0142>.
- P. A. M. Dirac. Fixation of coordinates in the hamiltonian theory of gravitation. *Physical Review*, 114(3):924–930, 1959. doi: 10.1103/PhysRev.114.924.
- B. Einfeldt. On godunov-type methods for gas dynamics. *SIAM Journal on Numerical Analysis*, 25(2):294–318, 1988. doi: 10.1137/0725021. URL <https://doi.org/10.1137/0725021>.
- A. Einstein. Die grundlage der allgemeinen relativitätstheorie. *Annalen der Physik*, 354(Issue 7):769–822, 1916.
- A. Einstein. Cosmological considerations in the general theory of relativity. *Sitzungsber. Preuss. Akad. Wiss. Berlin (Math. Phys.)*, pages 142–152, 1917.
- A. Escrivà, C. Germani, and R. K. Sheth. Universal threshold for primordial black hole formation. *Physical Review D*, 101(4), 2020. doi: 10.1103/PhysRevD.101.044022.
- C. R. Evans and J. S. Coleman. Critical phenomena and self-similarity in the gravitational collapse of radiation fluid. *Physical Review Letters*, 72(12):1782–1785, 1994. doi: 10.1103/PhysRevLett.72.1782.
- V. Faraoni. Embedding black holes and other inhomogeneities in the universe in various theories of gravity: a short review. 2018.
- V. Faraoni and A. Jacques. Cosmological expansion and local physics. *Physical Review D*, 76(6), 2007. doi: 10.1103/PhysRevD.76.063510.

- Y. Fourès-Bruhat. Sur l'intégration des équations de la relativité générale. *Journal of Rational Mechanics and Analysis*, 5(6):951–966, 1956.
- J. García-Bellido, B. Carr, and S. Clesse. A common origin for baryons and dark matter. *1904.11482*, 2019.
- K. Gödel. An example of a new type of cosmological solutions of einstein's field equations of gravitation. *Reviews of Modern Physics*, 21(3):447–450, 1949. doi: 10.1103/RevModPhys.21.447.
- E.ourgoulhon. *3+1 Formalism in General Relativity : Bases of Numerical Relativity*. Springer, Heidelberg, 2012.
- C. Gundlach and J. M. Martín-García. Critical phenomena in gravitational collapse. *Living Reviews in Relativity*, 10(1), Dec 2007. ISSN 1433-8351. doi: 10.12942/lrr-2007-5. URL <http://dx.doi.org/10.12942/lrr-2007-5>.
- T. Harada. Self-similar solutions, critical behavior and convergence to attractor in gravitational collapse. In *Invited review talk given at the 12th Workshop on General Relativity and Gravitation, Nov 25-28*, <https://arxiv.org/abs/gr-qc/0302004>, 2002.
- T. Harada, C.-M. Yoo, T. Nakama, and Y. Koga. Cosmological long-wavelength solutions and primordial black hole formation. *Physical Review D*, 91(8), 2015. doi: 10.1103/PhysRevD.91.084057.
- A. Harten, P. D. Lax, and B. v. Leer. On upstream differencing and godunov-type schemes for hyperbolic conservation laws. *SIAM Review*, 25(1):35–61, 1983. doi: 10.1137/1025002. URL <https://doi.org/10.1137/1025002>.
- I. Hawke and J. M. Stewart. The dynamics of primordial black-hole formation. *Classical and Quantum Gravity*, 19(14):3687–3707, Jun 2002. ISSN 0264-9381. doi: 10.1088/0264-9381/19/14/310. URL <http://dx.doi.org/10.1088/0264-9381/19/14/310>.
- S. Hawking. Gravitationally collapsed objects of very low mass. *Mon. Not. Roy. Astron. Soc.*, 152:75, 1971.
- S. W. Hawking. Particle creation by black holes. *Comm. Math. Phys.*, 43(3):199, 1975.
- S. W. Hawking and G. F. R. Ellis. *The Large Scale Structure of Space-Time*. Cambridge University Press, May 1973. ISBN 9780511524646. doi: 10.1017/cbo9780511524646. URL <http://dx.doi.org/10.1017/CBO9780511524646>.
- K. Jedamzik. Primordial black hole formation during the qcd epoch. *Physical Review D*, 55(10):R5871–R5875, 1997. doi: 10.1103/PhysRevD.55.R5871.
- H. Kodama. Conserved energy flux for the spherically symmetric system and the backreaction problem in the black hole evaporation. *Prog. Theor. Phys.*, 63(4): 1217, 1980.

- P. D. Lasky and A. W. C. Lun. Generalized lemaître-tolman-bondi solutions with pressure. *Physical Review D*, 74(8), Oct 2006. ISSN 1550-2368. doi: 10.1103/physrevd.74.084013. URL <http://dx.doi.org/10.1103/PhysRevD.74.084013>.
- B. V. Leer. Towards the ultimate conservative difference scheme. iv. a new approach to numerical convection. *Journal of Computational Physics*, 23(3):276 – 299, 1977. ISSN 0021-9991. doi: [https://doi.org/10.1016/0021-9991\(77\)90095-X](https://doi.org/10.1016/0021-9991(77)90095-X). URL <http://www.sciencedirect.com/science/article/pii/002199917790095X>.
- G. Lemaitre. Un univers homogène de masse constante et de rayon croissant rendant compte de la vitesse radiale des nébuleuses extra-galactiques. *Annales de la Société Scientifique de Bruxelles*, A47:49–59, 1927.
- G. Lemaitre. The expanding universe. *Ann. Soc. Sci. Bruxelles A*, 53:51–85, 1933.
- A. Lichnerowicz. *Problèmes globaux en mécanique relativiste*. Hermann et Cie, 1939.
- A. Lichnerowicz. L'intégration des équations de la gravitation relativiste et le problème des n corps. *J. Math. pures et appl.*, 23:37–62, 1944.
- A. Lichnerowicz. Sur les équations relativistes de la gravitation. *Bulletin de la Société Mathématique de France*, 80:237–251, 1952.
- D. H. Lyth, K. A. Malik, and M. Sasaki. A general proof of the conservation of the curvature perturbation. *Journal of Cosmology and Astroparticle Physics*, 2005 (05):004–004, May 2005. ISSN 1475-7516. doi: 10.1088/1475-7516/2005/05/004. URL <http://dx.doi.org/10.1088/1475-7516/2005/05/004>.
- D. Maison. Non-universality of critical behaviour in spherically symmetric gravitational collapse. *Physics Letters B*, 366(1):82 – 84, 1996. ISSN 0370-2693. doi: [https://doi.org/10.1016/0370-2693\(95\)01381-4](https://doi.org/10.1016/0370-2693(95)01381-4). URL <http://www.sciencedirect.com/science/article/pii/0370269395013814>.
- G. C. McVittie. The mass-particle in an expanding universe. *Mon. Not. Roy. Astron. Soc.*, 93(5):325–339, March 1933.
- C. W. Misner. Relativistic equations for adiabatic, spherically symmetric gravitational collapse. *Physical Review*, 136(2B):B571–B576, 1964. doi: 10.1103/PhysRev.136.B571.
- P. J. Montero and I. Cordero-Carrion. Bssn equations in spherical coordinates without regularization: Vacuum and nonvacuum spherically symmetric spacetimes. *Physical Review D*, 85(12), 2012. doi: 10.1103/PhysRevD.85.124037.
- P. J. Montero, T. W. Baumgarte, and E. Müller. General relativistic hydrodynamics in curvilinear coordinates. *Physical Review D*, 89(8), 2014. doi: 10.1103/PhysRevD.89.084043.

- I. Musco. Threshold for primordial black holes: Dependence on the shape of the cosmological perturbations. *Physical Review D*, 100(12), 2019. doi: 10.1103/PhysRevD.100.123524.
- I. Musco and J. C. Miller. Primordial black hole formation in the early universe: critical behaviour and self-similarity. *Classical and Quantum Gravity*, 30(14):145009, Jun 2013. ISSN 1361-6382. doi: 10.1088/0264-9381/30/14/145009. URL <http://dx.doi.org/10.1088/0264-9381/30/14/145009>.
- I. Musco, J. C. Miller, and L. Rezzolla. Computations of primordial black-hole formation. *Classical and Quantum Gravity*, 22(7):1405–1424, Mar 2005. ISSN 1361-6382. doi: 10.1088/0264-9381/22/7/013. URL <http://dx.doi.org/10.1088/0264-9381/22/7/013>.
- I. Musco, J. C. Miller, and A. G. Polnarev. Primordial black hole formation in the radiative era: investigation of the critical nature of the collapse. *Classical and Quantum Gravity*, 26(23):235001, Oct 2009. ISSN 1361-6382. doi: 10.1088/0264-9381/26/23/235001. URL <http://dx.doi.org/10.1088/0264-9381/26/23/235001>.
- T. Nakamura. 3-d numerical relativity. In T. M. Sasaki ed., Universal Academy Press, editor, *8th Nishinomiya-Yukawa Memorial Symposium : Relativistic Cosmology*, 1994.
- T. Nakamura, K. Oohara, and Y. Kojima. General relativistic collapse to black holes and gravitational waves from black holes. *Prog. Theor. Phys. Suppl.*, 90(1), 1987.
- D. W. Neilsen and M. W. Choptuik. Critical phenomena in perfect fluids. *Classical and Quantum Gravity*, 17(4):761–782, Jan 2000. ISSN 1361-6382. doi: 10.1088/0264-9381/17/4/303. URL <http://dx.doi.org/10.1088/0264-9381/17/4/303>.
- J. C. Niemeyer and K. Jedamzik. Dynamics of primordial black hole formation. *Physical Review D*, 59(12), 1999. doi: 10.1103/PhysRevD.59.124013.
- S. C. Noble and M. W. Choptuik. Driven neutron star collapse: Type i critical phenomena and the initial black hole mass distribution. *Physical Review D*, 93(2), 2016. doi: 10.1103/PhysRevD.93.024015.
- T. Padmanabhan. *Structure Formation In The Universe*. Cambridge Univ. Press, Cambridge, 1993.
- A. G. Polnarev and I. Musco. Curvature profiles as initial conditions for primordial black hole formation. *Classical and Quantum Gravity*, 24(6):1405–1431, Mar 2007. ISSN 1361-6382. doi: 10.1088/0264-9381/24/6/003. URL <http://dx.doi.org/10.1088/0264-9381/24/6/003>.
- F. Pretorius. Evolution of binary black-hole spacetimes. *Physical Review Letters*, 95(12), 2005. doi: 10.1103/PhysRevLett.95.121101.

- J. Requier. *Applications of the (3+1)-formalism of General Relativity to Cosmology : A study of Hybrid Inflation and Spherical Collapse with Quintessence*. Presses Universitaires de Namur, 2015.
- J. Requier, I. Cordero-Carrion, and A. Fuzfa. Fully relativistic nonlinear cosmological evolution in spherical symmetry using the bssn formalism. *Phys. Rev. D*, 91: 024025, 2015. doi: 10.1103/PhysRevD.91.024025. URL <https://arxiv.org/pdf/1409.3476.pdf>.
- J. Requier, A. Fuzfa, and I. Cordero-Carrion. Non-linear cosmological collapse of quintessence. *Phys. Rev. D*, 93:043533, 2016. doi: 10.1103/PhysRevD.93.043533. URL <https://arxiv.org/pdf/1509.08354.pdf>.
- L. Rezzolla and O. Zanotti. *Relativistic Hydrodynamics*. Oxford University Press (OUP), Oxford, 2013.
- M. Ricotti, J. P. Ostriker, and K. J. Mack. Effect of primordial black holes on the cosmic microwave background and cosmological parameter estimates. *The Astrophysical Journal*, 680(2):829–845, Jun 2008. ISSN 1538-4357. doi: 10.1086/587831. URL <http://dx.doi.org/10.1086/587831>.
- M. Ruiz, M. Alcubierre, and D. Núñez. Regularization of spherical and axisymmetric evolution codes in numerical relativity. *General Relativity and Gravitation*, 40(1): 159–182, Oct 2008. ISSN 1572-9532. doi: 10.1007/s10714-007-0522-3. URL <http://dx.doi.org/10.1007/s10714-007-0522-3>.
- M. Shibata. *Numerical Relativity*. World Scientific, Singapore, 2016.
- M. Shibata and T. Nakamura. Evolution of three-dimensional gravitational waves: Harmonic slicing case. *Physical Review D*, 52(10):5428–5444, 1995. doi: 10.1103/PhysRevD.52.5428.
- M. Shibata and M. Sasaki. Black hole formation in the friedmann universe: Formulation and computation in numerical relativity. *Physical Review D*, 60(8), Sep 1999. ISSN 1089-4918. doi: 10.1103/physrevd.60.084002. URL <http://dx.doi.org/10.1103/PhysRevD.60.084002>.
- M. Shibata and K. Uryu. Gravitational waves from the merger of binary neutron stars in a fully general relativistic simulation. *Progress of Theoretical Physics*, 107(2):265–303, Feb 2002. ISSN 1347-4081. doi: 10.1143/ptp.107.265. URL <http://dx.doi.org/10.1143/PTP.107.265>.
- R. Tolman. Effect of inhomogeneity on cosmological models. *PNAS; Proceedings of the National Academy of Sciences*, 20(3):169–176, 1934.
- J. M. Torres, M. Alcubierre, A. Diez-Tejedor, and D. Nuñez. Cosmological nonlinear structure formation in full general relativity. *Physical Review D*, 90(12), 2014. doi: 10.1103/PhysRevD.90.123002.

- C. M. Will. The confrontation between general relativity and experiment. *Living Reviews in Relativity*, 4(1), May 2001. ISSN 1433-8351. doi: 10.12942/lrr-2001-4. URL <http://dx.doi.org/10.12942/lrr-2001-4>.
- Y. B. Zel'dovich and I. D. Novikov. The hypothesis of cores retarded during expansion and the hot cosmological model. *Soviet Astronomy*, 10:602, 1967.